Steps in the Development of the GTL Process

R. L. Espinoza, D. S. Jack, H. A. Wright, J. D. Allison and S. R. Landis

Ponca City Technology Center, ConocoPhillips, PO Box 1267, Ponca City, OK 74602

1. Introduction
A commercial GTL process requires the synthesis of several different technologies with the core ones being those closely related to the generation of synthesis gas (CO + H2), Fischer-Tropsch synthesis and refining the F-T products. The methodology for the development of these technologies is similar, although some components (eg catalysis, reactor, modeling, etc) may be present in a higher degree in any given one, depending upon the stage of development. In this paper, and based on our experience, we will summarize the main technical development areas and the degree of detail necessary as a function of the project stages.

2. First Phase: Definition of the basic technology components
The full development of a GTL technology is an expensive process that may require an investment of a few hundred million dollars. Even this first definition stage, or exploratory stage, may require a considerable investment. There should therefore already be some basic ideas and/or preliminary experimental results that justify this first phase. Typical activities at this stage are:

- **Catalyst screening**. It is desirable to concentrate on a pre-selected main catalysis system (e.g., Fe or Co for FT, noble metal or standard refinery type FT wax hydrocracking catalyst for products upgrading), although work should include other systems to maximize chances for significant innovation. Normally this stage is characterized by a large amount of short experimental tests in micro reactors, with full characterization on only selected samples. There is an important input from the open literature (to avoid re-inventing the wheel) and a high creativity component. Catalyst deactivation studies are mostly confined to the identification of deactivation mechanism(s). Different catalyst supports and preparation techniques are studied at this stage.
- **Selection of the reactor system**. This should proceed in close coordination with the catalyst development due to the strong interdependence between these two elements. Micro reactors are commonly used, predominantly fixed bed and CSTR type reactors. This stage is characterized by the identification of the main advantages and disadvantages of the various reactor types and technical challenges for reliable commercial application.
- **Preliminary modeling**. Development of global kinetic equations, preliminary selectivity correlations, preliminary reactor(s) models based mainly on literature data for hydrodynamics, heat and mass transfer, solubilities, diffusion effects, etc
- **Process integration**. It is important to begin full time process engineering activities to understand how the emerging technologies fit into a commercial flow scheme. This activity also provides guidance to the technology team regarding the most important areas of research focus to ensure commercial success. Early process optimization proposals are developed.

3. Second Phase: Pilot Plants and definition of choice technology
In this stage, the type of reactors to be further developed has been identified, as well as the catalysts families and final desired products spectra. This phase is characterized by a period of focusing for the various developmental activities. Final products are produced in larger amounts and their properties are expected to be similar to those expected in commercial plant.

- **Catalysis**. This is a period of consolidation for the accuracy of predictive versus observed behavior. Efforts now concentrate on characterization, support design, stability, selectivity, costs and beginning of scale-up efforts. Design must be adapted to the characteristics of the selected reactor(s) and their effect on catalyst performance.
- **Reactors**. Depending upon the type selected, some hydrodynamic data are now available from smaller reactors and proposed solutions to their characteristic shortcomings are preliminarily tested and designs improved. A period of deeper technological understanding begins.
- **Modeling.** New data are used to improve existing models. Accuracy is improving and they can be used for preliminary commercial design. More sophisticated tools (like CFD) can now be developed.
- **Process Integration.** Optimum current technology configuration of the GTL process is now proposed, although it may still be subject to further improvement during the next phase. These results will help to focus the technical development even further.

4. Third Phase: Demonstration Plant

At this point, the main components of the GTL technology have been developed and will be put to the test. No major changes should occur, although an incremental improvement on the technology is expected. Final products are fully representative of commercial ones.

- **Catalysis.** The scale-up of the catalysts preparation to commercial size batches is completed well ahead of the plant start-up. Efforts now concentrate on the demonstration of all the elements of catalyst performance, and some "polishing up" is still expected. These elements have been considered in the design of the system, including requirements for efficient process integration.
- **Reactors.** The design and construction have concentrated not only on economic factors but also on reliability. Catalyst development results have played an important role.
- **Modeling**. Data from the larger reactor size should only result in minor improvements. Models are consolidated for commercial design.
- **Process Integration**. Desired plant configuration is defined. Reactor and catalysts characteristics have been taken into account.

Figures 1 and 2 illustrate the catalyst development process. Figure 1 is a typical example of industrial catalyst development. During the first or exploratory stage, the selected catalyst family do not perform optimally and the increase in performance – in this case catalyst intrinsic activity – is not high. The reason is that the chosen catalyst family must also fulfill other requirements like physical properties, selectivity, deactivation behavior and be adequate to the characteristics of the most probable reactor to be selected. At the onset of the second or consolidation stage, where the contribution of surface characterization increases and as the understanding of the catalyst system increases, there is a better match between predicted and expected catalyst behavior. This facilitates the design of improved versions of the same family of catalysts. The goal in this stage is to improve the performance of the chosen catalyst family in a fast manner, getting as close to the optimum as possible. During the later part of this phase, resources allocated to the identification of improved catalyst systems – probably a different catalyst family - should increase to avoid stagnation.

Figure 2 is an example of one of the constraints that are frequently encountered in industry during the catalyst development process. In this case, the methane selectivity was another parameter that had to be improved, while at the same time increasing the catalyst activity. Notice that as the understanding of the catalyst behavior increased, it was possible to keep lowering the selectivity towards the undesired methane production. This continuous improvement began to stagnate towards the later part of the second stage, probably indicating that we are reaching the optimum limits for the current catalyst family, when the catalyst is operated in the desired reactor and at the optimum range of operating conditions, as identified in the overall plant optimization studies.

This paper will include more examples to illustrate the typical activities during the different development stages of a GTL technology, like characterization activities, catalyst batch sizes, reactor sizes, model evolution, carbon efficiency, product generation, and reactor development tools (e.g. cold flow models).
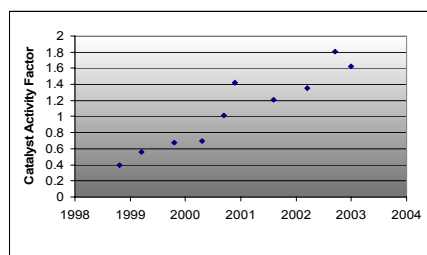

Figure 1. Typical improvement in catalyst activity as system understanding improves.
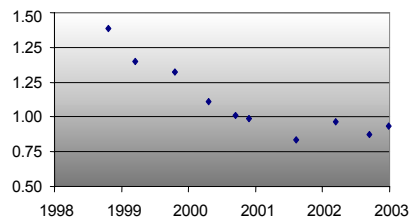

Figure 2. Relative Methane selectivity vs time. Reaching catalyst family limits?

SPRAY DRIED IRON CATALYSTS FOR SLURRY PHASE FISCHER-TROPSCH SYNTHESIS

Dragomir B. Bukur [a], Wen-Ping Ma [a], Victor H. Carreto Vazquez [a], Lech Nowicki [a] and Adeyinka A. Adeyiga [b]

[a] Department of Chemical Engineering, Texas A&M University, College Station, TX 77843
[b] Department of Chemical Engineering, Hampton University, Hampton, VA. 23688

Introduction

Recent developments in Fischer-Tropsch (F-T) technology have been directed towards the use of slurry bubble column reactors and maximization of production of high molecular weight hydrocarbons (wax). A critical issue in this reactor type is the ability to separate catalyst particles from the wax, which accumulates in the reactor. Catalysts with high attrition resistance are needed for this purpose.[1]

Researchers at Hampton University and University of Pittsburgh have studied attrition properties of iron F-T catalysts prepared by spray drying of $Fe/Cu/K/SiO_2$ precursors.[2-5] Attrition properties were evaluated using several types of tests: ultrasonic irradiation, fluidized bed and jet-cup method. Activity and selectivity of some of these catalysts were evaluated in a fixed bed reactor and were found to be comparable to that of the Ruhrchemie catalyst prepared by conventional precipitation.

The above studies of attrition properties provide information on relative attrition strength of different catalysts. However, test conditions employed are not representative of conditions encountered in a slurry bubble column reactor (SBCR) or a stirred tank slurry reactor (STSR).

The present study has been undertaken to investigate attrition properties of two iron F-T catalysts, synthesized at Hampton University, by following changes in particle size distribution (PSD) during F-T synthesis in a STSR, and to provide information on activity and selectivity of these catalysts in a slurry reactor.

Experimental

Catalyst Synthesis. Details of catalyst preparation procedure can be found elsewhere.[2-3] Briefly, the catalyst containing binder silica was prepared by co-precipitation of iron and copper nitrates, followed by washing and addition of aqueous potassium carbonate and silica binder. The resulting slurry was spray dried at 250°C in a bench scale Niro spray dryer. The catalyst containing precipitated silica was prepared by simultaneous precipitation of $Fe/Cu/SiO_2$ precursor. Aqueous tetraethylorthosilicate (TEOS) was used as a source of silica.

Characterization Methods. Slurry samples withdrawn from the STSR were first washed with a commercial solvent to remove residual liquid medium. After drying the catalyst samples were analyzed by SEM (morphological properties) and their particle size distribution (PSD) was determined by a Coulter Counter Multisizer. SEM specimens were observed at different magnifications using a JEOL JSM-6400 Scanning Electron Microscope at 10 mA for 8 minutes.

Slurry Reactor. Catalysts were tested in a one-liter STSR (Autoclave Engineers). Details of reactor set-up, operating procedures and product quantification can be found elsewhere. [6-7]

Results and Discussion

Morphological Properties. SEM micrographs of as received (no sieving or calcination) spray-dried catalysts prepared at Hampton University are shown in Figures 1 and 2. Particle size distribution of 100 Fe/5 Cu/4.2 K/11 (P) SiO_2 (P = precipitated silica) catalyst (HU2061) is broad and most of the particles are irregularly shaped with some of them having plate-like morphologies (Fig.1). Smaller particles (5-10 μm) are nearly spherical, but with rough surfaces. The observed morphology (large number of irregularly shaped) is not expected to result in high attrition strength. Majority of particles of 100 Fe/5 Cu/4.2 K/1.1 (B) SiO_2 (B = binder silica) catalyst (HU3471) are spherical (Fig. 2), but their external surfaces are relatively rough. Particle size distribution for this catalyst is also rather broad.
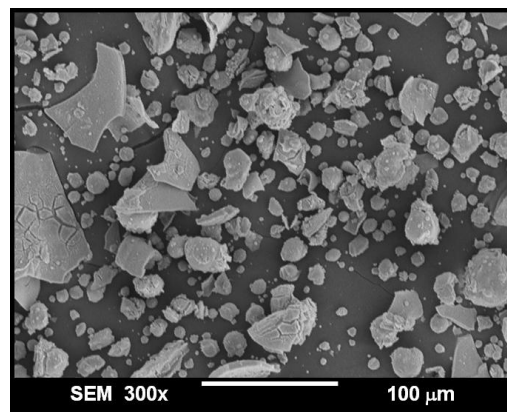

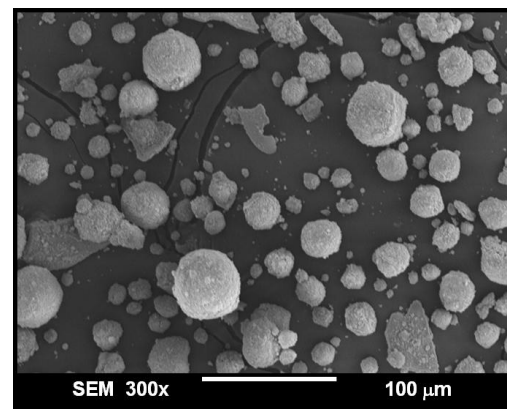**Figure 1.** SEM image of 100 Fe/5 Cu/4.2 K/11 (P) SiO_2 catalyst.

Figure 2. SEM image of 100 Fe/5 Cu/4.2 K/1.1 (B) SiO_2 catalyst.

Catalyst Activity and Selectivity. As received catalysts (14-15 g) and 320-350 g of Durasyn 164 oil (a hydrogenated 1-decene homopolymer, ~ C_{30} obtained from Albemarle Co.) were loaded into the STSR. The catalysts were pretreated in CO at 280°C, 0.8 MPa, 3 Nl/g-cat/h for 12 hours. Slurry samples were withdrawn from the reactor before the pretreatment and at the end of the run for particle size distribution measurements. After the pretreatment, the catalysts were tested at 260°C, 2.1 MPa, $H_2/CO = 0.67$ and gas space

velocities of either 3.1 Nl/g-Fe/h (run SB-20601) or 3.3 Nl/g-Fe/h (run SB-34701).

Changes in synthesis gas conversion with time are shown in **Figure 3**. During the first 50-80 hours of testing the syngas conversion increased with time reaching 85-87%. After reaching the maximum conversion, the catalysts started to deactivate, and at 200 hours on stream the syngas conversion was about 76%. Both catalysts were tested up to 384 h (SB-20601) and 449 h (SB-34701) on stream under different process conditions (results not shown) and then the slurry samples were withdrawn for PSD measurements.
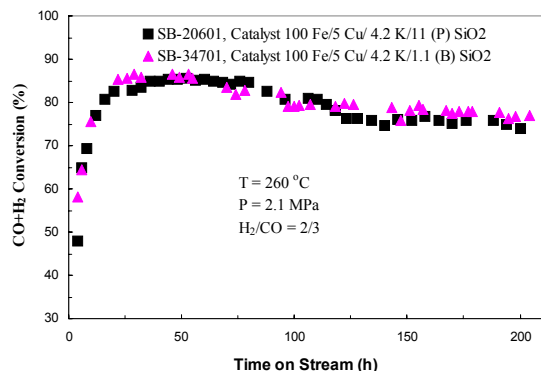

Figure 3. Change in syngas conversion with time-on-stream.

Hydrocarbon selectivities (CH_4 and C_5^+) were similar in both tests. Methane selectivity (**Figure 4**) decreased during the first 150 h of testing, reaching a stable value of 2.0±0.2% (carbon atom basis). Selectivity of C_5^+ hydrocarbons (liquids and wax) was high in both tests. It increased to 84-86% during the first 130 hours of testing, and then remained fairly stable. Methane and C_5^+ selectivities were independent of conversion level and/or process conditions.
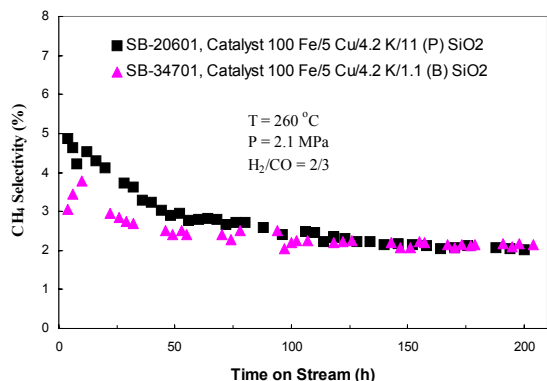

Figure 4. Change in CH_4 selectivity with time-on-stream.

Attrition Properties. Attrition behavior of catalysts tested in this study was evaluated on the basis of observed changes in morphological properties (via SEM), and changes in particle size distribution (PSD) after STSR testing. From PSD results, one can obtain several parameters that can be used to quantify attrition. These are: changes in Sauter mean diameter ($d_{3,2}$), and change in fraction of fine particles (particles < 10 μm in diameter) during testing in the STSR. Generation of fine particles (fines) is important in assessing attrition behavior of iron F-T catalysts, since fine particles cause

separation problems during SBCRs' operation. Results from PSD measurements are summarized in **Table 1**.

Table 1. Summary of PSD Results Obtained Using the Coulter® Counter Multisizer (From Volume Distributions)

Run ID	t*, h	% Change after t* hours in the STSR	Change in fraction of fines
		$\Delta d_{3,2}$	< 10 μm
SB-20601	380	87	62.5
SB-34701	449	39.9	3.7

Attrition results show that HU2061 catalyst used in run SB-20601 had much lower attrition resistance relative to HU3471 catalyst (run SB-34701). This catalyst experienced large reduction in Sauter mean diameters (87%) after 380 h of testing in the STSR. The inferior attrition strength of this catalyst is also reflected in considerable generation of fine particles during the STSR test (62.5 %). HU 34701 catalyst had experienced a modest reduction in Sauter mean diameter (over a longer period of testing) and generation of fine particles was small. The attrition properties of this catalyst are satisfactory for use in a SBCR.

Concluding Remarks

Spray-dried catalysts with compositions 100 Fe/5 Cu/4.2 K/11 (P) SiO_2 and 100 Fe/5 Cu/4.2 K/1.1 (B) SiO_2 have excellent selectivity characteristics (low methane and high C_5^+ yields), but their productivity and stability (deactivation rate) need to be improved. Mechanical integrity (attrition strength) of these two catalysts was markedly dependent upon their morphological features. The attrition strength of the catalyst made out of largely spherical particles (1.1 (B) SiO_2) was considerably higher than that of the catalyst consisting of irregularly shaped particles (11 (P) SiO_2). Improvements in spray drying operating parameters resulting in narrower PSD and higher sphericity could lead to further improvements in the attrition strength.

References
1. Jager, B.; Espinoza, R. *Catal. Today*, **1995**, 23, 17.
2. Jothimurugesan, K.; Goodwin, J. G., Jr.; Santosh, S. K.; Spivey, J. J. *Catal. Today* **2000**, 58, 335.
3. Jothimurugesan, K.; Spivey, J. J.; Gangwal, S. K.; Goodwin, J. G., Jr. in "Natural Gas Conversion V", *Stud. Surf. Sci. Catal.* **1998**, 119, 215.
4. Zhao, R.; Goodwin, J. G., Jr.; Jothimurugesan, K.; Gangwal, S. K.; Spivey, J. J. *Ind. Eng. Chem. Res.* **2001**, 40, 1065.
5. Sudsakorn, K.; Goodwin, J. G., Jr.; Jothimurugesan, K.; Adeyiga, A. A. *Ind. Eng. Chem. Res.* **2001**, 40, 4478.
6. Bukur, D. B.; Patel, S. A.; Lang, X. *Appl. Catal.* **1990**, 186, 329.
7. Bukur, D. B.; Nowicki, L.; Lang, X. *Chem. Eng. Sci.* **1994**, 49, 4615.

MIXED IRON-MANGANESE OXIDE NANOPARTICLES

Jr-iuan Lai,[1,5] Kurikka V. P. M. Shafi,[1,5,] Abraham Ulman,*[1,5] Nan-Loh Yang,[2,5] Min-Hui Cui,[2,5] Thomas Vogt,[3] Claude Estournès,[4]

[1]Department of Chemical Eng., Chemistry & Material Science, Polytechnic University, 6 Metrotech Center Brooklyn, NY 11201.
[2]Department of Chemistry, CUNY at Staten Island, 2800 Victory Boulevard,Staten Island**.**
[3]Physics Department, Brookhaven National Laboratory, P.O. Box 5000, Upton, NY 11973-5000
[4]Institut de Physique et Chimie des Matériaux de Strasbourg Cedex, France
[5]The NSF MRSEC for Polymers at Engineered Interfaces

Introduction

Magnetic nanoparticles have applications in information storage,[1] color imaging,[2] magnetic refrigeration,[3] medical diagnosis,[4] controlled drug delivery,[5] and as ferrofluids.[6] Thus, developing a new synthetic route for magnetic nanoparticles and the investigation of their properties are of great importance.[7]Nanocrystal materials are also known to have superior mechanical properties due to the extremely fine grain size[8]. However, it has not been well established that alloy and alloy-oxide composite coatings with nanocrystal grains have unique properties at high temperatures. Nanocrystal structures promote selective oxidation, forming protective oxidation scales with superior adhesion to the substrate.[9]

Ferrites, the transition metal oxides having a spinel structure, are technologically important because of their interesting magnetic and electrical properties. They are used in magnetic inks and magnetic fluids, and for the fabrication of magnetic cores of read/write heads for high-speed digital tapes or for disc recording.[10] One important example is manganese oxide, which has the desirable properties of low cost and low toxicity. As with other electrically conductive metal oxides, manganese oxide stores electrical charge by a double insertion of electrons and cations into the solid state. Maghemite (γ-Fe$_2$O$_3$, the ferrimagnetic cubic form of iron(III) oxide) is also technologically important, as it is being used widely for the production of magnetic materials and catalysts. Because of the small coercivity of Fe$_2$O$_3$ nanoparticles, which arises from a negligible barrier in the hysteresis of the magnetization loop, they can be used as magneto-optical devices. Magneto-optic media can be made by depositing magnetic and optically transparent materials, and maghemite particles satisfy this condition, since they can be easily incorporated in to ultrathin polymer films. In this paper, we discuss the sonochemical synthesis and characterization of nanosized manganese iron oxide powder

Experimental

Synthesis. Samples of α-Fe$_2$O$_3$, γ-Fe$_2$O$_3$, and manganese iron mixed oxide nanoparticles with varied Mn:Fe ratios, as well as Mn$_2$O$_3$ were synthesized using ultrasonication. Manganese iron mixed oxides were prepared by irradiating mixtures of different ratios of amorphous Fe$_2$O$_3$ nanoparticles (5-10 nm in diameter) and Mn$_2$(CO)$_{10}$ with a high intensity ultrasonic horn, under air, for 2 hours. Due to the high cavitational rate ($>10^9$ K s^{-1}) in the ultrasonication process, the synthesized products are amorphous nanoparticles. Elemental analysis of the amorphous nanoparticles was obtained by atomic absorption. The amorphous nanoparticles were crystallized using an annealing process, at temperatures. determined by DSC measurements. Pure γ-Fe$_2$O$_3$ nanoparticle samples were prepared by heating amorphous Fe$_2$O$_3$ nanoparticles at 300°C for 3 hours, while α-Fe$_2$O$_3$, Mn$_2$O$_3$ and manganese iron mixed oxides are prepared by heating the corresponding amorphous nanoparticle samples at 500°C for 3 hours.

Characterization Powder XRD was performed by using a Philips X-ray diffractometer (Cu K$_\alpha$ radiation, λ = 1.5418 Å). Synchrotron Powder X-ray Diffraction experiments were preformed at the beamline X7A of the National Synchrotron Light Source (NSLS) at Brookhaven National Laboratory with a linear position-sensitive detector gating electronically on the Kr-escape peak. Nanocrystal size and morphology were estimated by using a Phillips CM-12 Transmission Electron Microscope (100 KeV) Element analysis was performed by using Perkin-Elmer flame and graphite furnace atomic absorption spectroscopy. Magnetic data of the solid samples were obtained with a Princeton Applied Research vibrating sample magnetometer Model 155 (VSM) and a Quantum Design SQUID MPMS-XL (AC and DC modes and maximum static field of ± 5 T). X-band EPR spectra were recorded on a Bruker ESP380E spectrometer equipped with a HP 5361 frequency counter. The unpaired spin density was evaluated by comparison with a diphenylpycrilhydrazyl (DPPH) as an internal standard marker calibrated against Mn^{2+}/CaO with known spin number.

Results and Discussion

Figure 1(shown left) presents a TEM image of crystalline manganese iron mixed oxide with 32.08% Mn$_2$O$_3$ content. The bright field image shows aggregation due to sintering. This is a common phenomenon when amorphous nanoparticles are heated. The diffraction pattern reveals that these nanoparticles are highly crystallized. The XRD patterns for γ-Fe$_2$O$_3$, mixed γ-Fe$_2$O$_3$-Mn$_2$O$_3$ oxide nanoparticle samples with Mn$_2$O$_3$ concentration from 8.49% to 32.08%, where *a* is the index of γ--Fe$_2$O$_3$ and *b* is the XRD pattern of synthesized Fe$_2$O$_3$. The XRD pattern of synthesized Fe$_2$O$_3$ matches well the γ--Fe$_2$O$_3$ index. Patterns *c~f* show the XRD for manganese iron mixed oxide with Mn$_2$O$_3$ concentrations from 8.49% to 32.08%. The comparison of patterns *c~f* to *a* reveals that the positions and relative intensities of the strong peaks match those of γ-Fe$_2$O$_3$, which is spinel structure.

In Figure 2, *a* is the index of Mn$_{2-x}$Fe$_x$O$_3$ and *e* is the synthesized Mn$_2$O$_3$. Patterns *b~d* are for manganese iron mixed oxides with Mn concentrations from 60.38% to 68.87%. As is apparent from Figure 3,4, the index of Mn$_{2-x}$Fe$_x$O$_3$ is almost the same as that of Mn$_2$O$_3$, and hence *a* was used as index of both Mn$_{2-x}$Fe$_x$O$_3$ and Mn$_2$O$_3$. The XRD pattern of the synthesized Mn$_2$O$_3$ matches the index of Mn$_2$O$_3$. By comparing b~d to *a*, it was found that the positions and relative intensities of the strong peaks in these patterns match to Mn$_{2-x}$Fe$_x$O$_3$ which is bixbyite structure. Figure 3 shows the synchrotron powder X-ray diffraction of the sample with ≤ 5% Mn(III). The crystal structure of this sample is γ-Fe$_2$O$_3$. This suggests that when the Mn(III) concentration is ≤5% it does not prevent the crystal from adopting the stable α-Fe$_2$O$_3$ structure. We have not investigated the concentration window between 5% and 8.49% Mn(III), and hence the exact concentration where the transition from γ- to α-Fe$_2$0$_3$ occurs is still unknown.

X-ray studies reveal another interesting behavior of samples with low Mn(III) content. The annealing at 500°C should crystallize the pure amorphous iron oxide to the α-Fe$_2$O$_3$ form, which is a hexagonal structure. Indeed, when the Mn(III) concentration was ≤5%, the α-Fe$_2$O$_3$ structure was maintained. Thereafter, in nanoparticle samples with Mn(III) concentration between 8.49% and 32.08% the transition from spinel (γ-Fe$_2$O$_3$ obtained at 300°C) to

hematite(α-Fe$_2$O$_3$ obtained at 500°C) was suppressed. That the mixed oxide samples crystallized as γ-Fe$_2$O$_3$ suggests single-phase
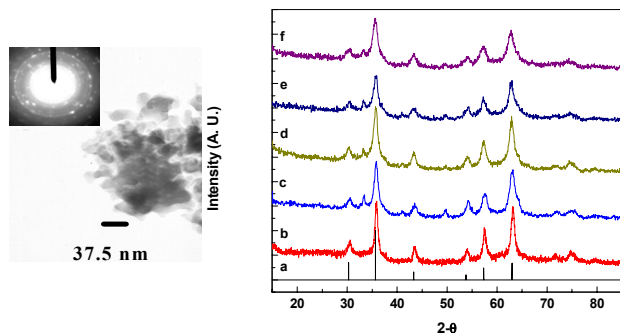
Figure 1 XRD patterns: a. index of γ-Fe$_2$O$_3$; b. Fe$_2$O$_3$; c. 8.49% Mn(III); d. 18.87% Mn(III); e. 27.83% Mn(III); f. 32.08% Mn(III). TEM image of manganese iron mixed oxide with 32.08% Mn(III). is shown on left
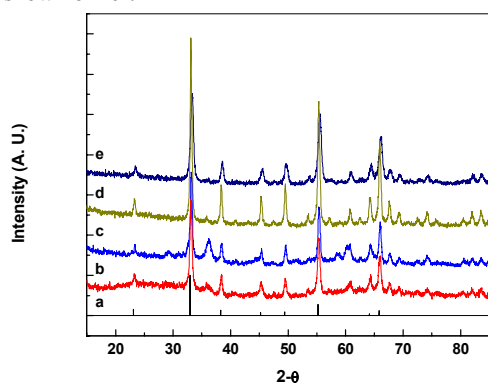

Figure 2. XRD patterns: a. index of Mn$_{2-x}$Fe$_x$O$_3$; b. 65.09% Mn(III); c. 60.38% Mn(III); d. 68.87% Mn(III); e. Mn$_2$O$_3$
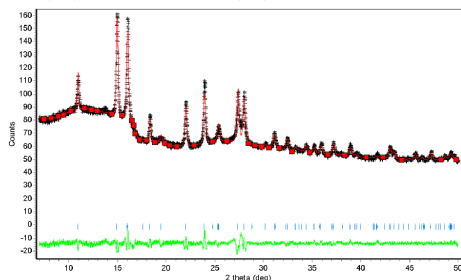
Figure 3. Synchrotron powder x-ray diffraction of $\leq$ 5% Mn sample

compounds and not mixtures. If the latter was the case, the XRD patterns should have peaks of both α-Fe$_2$O$_3$ and Mn$_2$O$_3$, which was not observed in any of our samples. We observed that even pre-annealed samples require temperatures as high as 600°C to completely convert to the α-phase, indicating high activation energy for this process. We believe that the suppression of the γ- (cubic) to α-Fe$_2$O$_3$ (hexagonal) transition is due to the fact that while Mn(III) has a cubic spinel phase (with more free volume) it does not transform into a hexagonal one, and therefore doping Fe$_2$O$_3$ with Mn(III) increases the activation energy for the transition to the more compact α-phase, which requires lattice contraction. Thus, above a critical concentration (between 5 and 8.5%) the transition needs temperatures higher than 600°C to complete. Figures 4 presents the

magnetization curves of γ-Fe$_2$O$_3$, manganese iron mixed oxide and Mn$_2$O$_3$ at 5K. When the magnetization measurements were carried out at room temperature, no coercivity could be observed. Bulk γ-Fe$_2$O$_3$ is ferrimagnetic. However, due to their small dimensions, γ-Fe$_2$O$_3$ nanoparticles are superparamagnetic. Mn$_2$O$_3$ nanoparticles, on the other hand, show antiferromagnetic behavior, similar to the bulk material. The magnetization curves of crystalline Fe-Mn mixed oxide nanoparticles with Mn(III) concentrations from 8.49% to 38.68% show superparamagnetic behavior where as the samples with Mn(III) from 54.72% to 68.87% are linear with small positive susceptibility, which is in agreement with antiferromagnetic behavior. These results show that as the crystal structure transforms from spinel to bixbyite, the magnetic properties transform from superparamagnetic to antiferromagnetic. Taken together the results show that the maximum of the magnetization decreases with the increasing Mn(III) concentration.
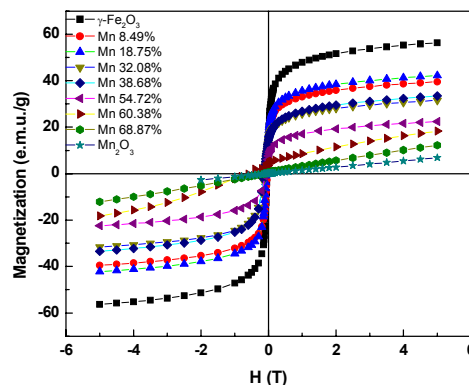

Figure 4. Magnetization curves at 5K.

EPR studies (not shown) also reveal that the spin densities (per gram of Fe$_2$O$_3$ and per gram of sample) of Mn(III) doped Fe$_2$O$_3$ nanoparticles decrease markedly with increasing Mn(III) The normalized spin density of the sample with 68.9% Mn(III) is 6 x 10^{21} spins/g Fe$_2$O$_3$, one order of magnitude lower than that of sample with 8.5% Mn(III) (8.5 x 10^{22} spins/g Fe$_2$O$_3$). Such a reduction in the normalized spin density can be attributed to antiferromagnetic coupling of Fe with Mn.

Conclusions

All physical measurements support compete mixing of the Fe(III) and Mn(III) ions in the mixed oxide amorphous samples. According to XRD, the crystal structures of manganese iron mixed oxides change from spinel to bixbyite crystal structures with increasing of Mn(III) content. The γ-Fe$_2$O$_3$ crystal structure of samples with low Mn(III) content shows that the samples are single-phase compounds. This might due to the replacement of Fe(III) atoms with Mn(III) atoms as supported by EPR data of efficient antiferromagnetic coupling due to the presence Mn(III).

References
1. Audram, A. G.; Huguenard, A. P. In *U.S. Patent*: U.S., 1981.
2. Ziolo, R. F. In *U.S. Patent*, 1984.
3. McMichael etal *J. Magn. Magn. Mater.* **1992**, *111*, 29.
4. Josephson, L. et al *Bioconjugate Chem.* **1999**, *10*, 186.
5. Bhatnagar,S.P.; Rosensweig, R.E. *J.Magn. Magn.Mater.* **1995**, *149*.
6. Rosensweig,R.E.*Ferrohydrodynamics*;MIT Press:Cambridge, 1985.
7. Shafi, K. V. P. M.et al *Chem. Mater.* **2002**, *14*, 1778.
8. Morris, D. *Mechanical Behaviour of Nanostructured Materials*; Trans Tech Publications Ltd., 1998.
9. Gao, W.; Liu, Z.; Li, Z.; Li, S. S.; Gong, H. *International Journal of Modern Physics B* **2002**, *16*, 128.
10. Charles, S. W.; Popplewell, J. *Ferromagnetic Materials*; North-Holland: Amsterdam, 1980; Vol. 2.

ACETYLENES AS PROBES IN THE FISCHER-TROPSCH REACTION

Yulong Zhang, Li Hou, John W. Tierney and Irving Wender

Department of Chemical and Petroleum Engineering
University of Pittsburgh
Pittsburgh, PA 15261

Introduction

Present worldwide interest in the Fischer-Tropsch (FT) synthesis is centered on the conversion of natural gas to synthesis gas which is then converted to diesel and jet fuels over a cobalt catalyst.

Incorporation of probe molecules has been used widely in elucidating the mechanism of FT reactions. Several C1 probes such as methyl chlorides $CHxCl_{4-x}$,[1] and nitromethane CH_3NO_2[2] in FT reactions have been studied. The results suggested that C1 species derived from decomposition of these C1 molecules can be incorporated into FT and serve as monomers for chain growth. Surface C1 species were captured using cyclohexene as a probe on ruthenium catalysts.[3] In this paper, acetylenic compounds have been used as probes.

Experimental

Catalyst Preparation. Cobalt catalysts were prepared by an incipient wetness impregnation technique. Vista B alumina with grain particle sizes of 70-140 mesh was calcined at 500° C for 10 h before impregnation. Cobalt nitrate was dissolved with suitable amounts of deionized water, and then impregnated on calcined alumina. The catalyst was dried at 110° C overnight, and calcined at 300° C for 2 h. An iron catalyst with a composition of 100Fe/1.25K/4.4Si was obtained from the University of Kentucky.

Incorporation of Probes. FT reactions were carried out in a stainless-steel tubular microreactor of 3/8 in (0.95cm) diameter. Probe molecules were added into the FT reaction continuously by a syringe pump. A thermocouple was inserted into the middle of the catalyst bed. 0.5 g of cobalt or 1.0 g of iron catalysts were mixed with 1 g of quartz sands and loaded in the reactor. The catalyst then was activated by H_2 at a rate of 50 ml/min, with a temperature program ramping from room temperature to 350° C at 1° C/min, holding at 350° C for 10 hours. After reduction, the temperature of the reactor was lowered to the reaction temperature in H_2. The gas stream then was switched to Ar. The FT reaction was started by gradually increasing the CO and H_2 flow rates and, at the same time, decreasing the Ar flow rate in 2 h to avoid the temperature surge due to highly active sites present in the fresh catalyst. Wax products were collected by a hot trap at about 200° C. Liquid products were collected by a cold trap in an ice-water bath. A stream of effluent gas was split out between hot and cold traps and went through three sampling valves and analyzed by two GCs (HP6890, HP5890) controlled by HP Chemstation equipped with three GC columns (HP-5 capilary column, Porapak Q packed column, and Carbonsphere packed column) for online analysis of whole products except for heavy waxes. Transfer lines before sampling valves are kept at 230° C to avoid condensation of heavier products. Liquid products collected in the cold trap were analyzed by HP GC-MS with a HP-5 capillary column to identify components of the FT products.

Probe incorporations were carried out at 100 psi (0.7MPa), The probe molecules were added in pentane (10% in volume) with a total flow rate of 2ml/h. Other conditions varied with the catalyst: iron catalyst, WHSV=3.6NL/g/h, CO/H_2=3/2, 170° C and 260° C; cobalt catalyst, WHSV=7.2NL/g/h, CO/H_2=1/2, 150 ° C, 180° C and 220° C.

The pump and the transfer lines of the reaction system were washed with pentane after each experiment to reduce possible interference by remaining probes and condensations of previous runs. Conversions were kept below 5% to ease the condensation of the heavier hydrocarbons at transfer lines.

Results and Discussion

1-Hexyne, 2-hexyne, phenylacetylene, 4-phenyl-1-butyne and 1-phenyl-1-propyne were used as probe molecules. 1-Hexyne, phenylacetylene and 4-phenyl-1-butyne have terminal carbon-carbon triple bonds. 2-Hexyne and 1-phenyl-1-propyne have internal carbon-carbon triple bonds. 1-Hexene was added for comparison purposes.

Incorporation on Cobalt Catalyst. Incorporation of alkynes is much more effective than incorporation of olefins. At 150° C, FT on cobalt catalyst is essentially inactive. Incorporation of 1-hexene is negligible at this temperature. However, 1-hexyne is readily incorporated and C7$^+$ products are formed under such conditions. It could be postulated that all the products obtained at 150° C originate from 1-hexyne. 1-Hexyne initiates chain growth and the hydrocarbon chain grows by stepwise addition of C1 monomers.

Since products of incorporation of 1-hexyne overlap normal FT products, it is difficult to distinguish the alkyne initiated products from normal FT products. Several phenylacetylenes were used as probe molecules. With the phenyl group as a marker, the products from normal FT and from alkyne initiated FT were easily distinguished by GC and GC-MS.

Figure 1 shows the GC-MS results of incorporation of 4-phenyl-1-butyne. It is apparent that normal FT products (labeled underneath) and 4-phenyl-1-butyne initiated FT products (labeled with a benzene ring) are formed.
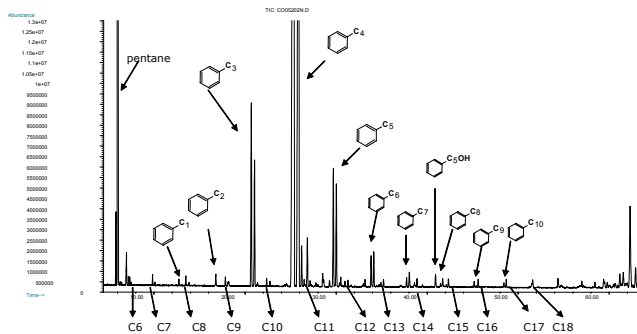

Figure 1. GC-MS analysis of FT liquid products with 4-phenyl-1-butyne addition at 180° C, CO/H_2=3/2, 0.7 MPa, cobalt catalyst.

With incorporation of terminal alkynes, the chain grows from the end of the carbon-carbon triple bond and produces a series of products with α-olefins as the main product. This behavior is very similar to normal FT reactions, suggesting that the intermediates formed from adsorption of terminal alkynes are similar to the intermediates in normal FT.

Incorporation of internal alkynes behaves differently from incorporation of terminal alkynes. Branched hydrocarbon chains are formed with incorporation of 2-hexyne. The activity for incorporation of internal alkynes is lower than incorporation of terminal alkynes. Unlike terminal alkynes, from which dimerization always occurs, internal alkynes do not dimerize.

Except for phenylacetylene, incorporation of above alkynes produces aldehydes and alcohols with one added carbon. 1-Heptanal

and 1-heptanol are formed with addition of 1-hexyne. 5-phenyl-1-pentanal and 5-phenyl-1-pentanol are obtained with incorporation of 4-phenyl-1-butyne. Incorporation of the internal alkynes leads to branched aldehydes and alcohols. In any case, only oxygenates with one carbon more than the probes are formed on cobalt. This is reminiscent of the hydroformylation reaction. To test the mechanism of oxygenate formation, thiophene was injected. It is well-known that sulfur poisons FT activity but hydroformylation is resistant to sulfur. Results show that hydrocarbon products from normal FT and probe initiated FT diminish with injected thiophene, but oxygenate formation is much less affected. This suggests that the oxygenates are formed by hydroformylation. It is recognized that the FT reaction occurs at conditions just below those at which carbonyls are formed.[4] Shultz[5] has shown that hydroformylation occurs on incorporation of olefins into FT on cobalt catalysts.

Incorporations on Iron Catalysts. Incorporation of the probes on an iron catalyst was carried out at 170°C and 260°C. At 170°C, normal FT activity on iron catalyst is negligible and the observed products originate only from incorporation of probe molecules. At 260°C, both normal FT and the initiation by the probe molecule are observed. **Figure 2** shows the GC-MS analysis of liquid products of FT with phenylacetylene addition.
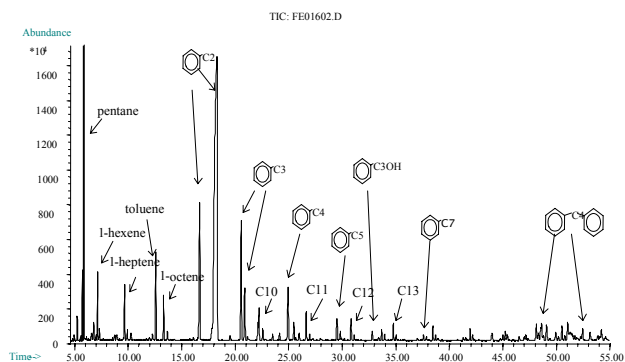

Figure 2. GC-MS analysis of FT liquid products with phenylacetylene addition at 260°C, CO/H$_2$=3/2, 0.7 MPa, iron catalyst.

It is clear that two types of chain growth mechanisms take place with incorporation of phenylalkynes at 260°C. In addition to the normal FT products, phenylacetylene initiated products are superimposed.

Oxygenates originating from phenylalkynes are observed. With addition of phenylacetylene at 170°C, about half of the C^{9+} products are oxygenates, mainly aromatic aldehydes and alcohols. Oxygenates decrease with increase in temperature to 260°C and aldehydes are hydrogenated to alcohols.

In 1970s, a group of Russian researchers[6] explored synthesis of alcohols with fused iron catalysts. It was found that acetylene can initiate chain growth for higher oxygenate formation at high pressure (above 10MPa) and 170-190°C in CO hydrogenation. Their aim was to produce higher alcohols. Our experiments were conducted under 0.7 MPa on a precipitated iron catalyst, which is close to normal FT conditions on iron catalysts. Our results show that incorporation of probes enhances oxygenate selectivity and overall activity at 170°C.

Mechanisms of Incorporation and FT. Chain growth in FT is believed to be stepwise polymerization of monomers with one carbon and product distribution follows Schultz-Flory kinetics. This distribution is generally true except for much lower C2 and higher

CH$_4$ yields than predicted. Lower C2 yields may indicate a deviation from the standard stepwise polymerization mechanism. It has been explained as the result of readsorption and incorporation into the FT product. However, chain growth may start from C2 rather than the C1 monomer. Carbon-carbon coupling of the C1 species into C2 is slower than subsequent chain growth. Adsorption of acetylene forms C2 intermediates which initiate chain growth[6]. Higher yield of alkyne probe initiated FT products than the normal FT products at lower temperature provides an evidence for this mechanism. Much easier incorporation of alkynes than olefins suggests that that the initiating entity of chain growth may be more unsaturated than an alkyl.

Conclusions

Phenylalkynes are incorporated into FT on both cobalt and iron catalysts and function as a chain growth initiator to the position of carbon-carbon triple bond. Incorporation of terminal phenylalkynes, such as phenylacetylene and 4-phenyl-1-butyne produces straight chain phenylalkenes and phenylalkanes. Incorporation of an internal alkyne, such as 1-phenyl-1-propyne, yields branched phenylalkenes and phenylalkanes. At low temperatures, almost all of the products originate from phenylalkyne incorporation; at such conditions normal FT activity is very low. At normal temperatures, alkyne originated and normal FT products are superimposed. Oxygenates are also produced and vary with catalyst and reaction temperature. Iron catalysts produce oxygenates of various chain lengths. Cobalt catalysts produce oxygenates only with one carbon more than the probe molecules, which resembles hydroformylation. At low temperatures, the primary oxygenates are aldehydes; with increase in temperature the aldehydes are hydrogenated to alcohols.

It is tempting to suggest that there is an energy barrier to formation of the initial carbon-carbon bond in the FT reaction. This is overcome by laydown of two carbons from an acetylenic molecule. As to formation of hydroformylation products, initial adsorption of an acetylenic molecule "leaves" a double bond in the adsorbed probe; this may undergo a hydroformylation reaction.

References
(1) Van Barneveld, W. A. A.; Ponec, V. In *J. Catal.*, 1984; Vol. 88, pp 382-387.
(2) Cavalcanti, F. A. P.; Oukaci, R.; Wender, I.; Blackmond, D. G. *J. Catal.* **1990**, *123*, 270-274.
(3) Ekerdt, J. G.; Bell, A. T. *J. Catal.* **1980**, *62*, 19-25.
(4) Pichler, H. *Adv. Catal.* **1952**, *4*, 271-342.
(5) Schulz, H.; Claeys, M. *Appl. Catal. a-Gen.* **1999**, *186*, 71-90.
(6) Loktev, S. M. *J. Catal.* **1982**, *17*, 255-230.

EFFECT OF CALCINATION TEMPERATURE ON THE PERFORMANCE OF Co/ZrO$_2$ CATALYSTS FOR FISCHER-TROPSCH SYNTHESIS

Hongxia Zhao, Jiangang Chen, Yuhan Sun

State Key Laboratory of Coal Conversion,
Institute of Coal Chemistry, Chinese Academy
of Sciences, P.O.Box 165, Taiyuan 030001, P.R. China

Introduction

Cobalt has been one of the most commonly used metals for Fischer-Tropsch catalysts since the 1930s because of its high activity [1]. It has become well established that the performance of a heterogeneous catalyst not only depends on the intrinsic catalytic activity of the components but also on its texture and stability. One of the most important factors in controlling the texture and strength of a catalyst involves the correct choice of a support and the preparation of the support in the appropriate form.

Zirconium oxide has attracted considerable attention recently as a catalyst support because of its high thermal stability and the amphoteric character of its surface hydroxyl groups [2-3]. Extensive studies have been made of the effect of temperature on the development of the porous texture or structure in samples of zirconia [4]. The majority of the textural studies have, however, been confined to low calcination temperature (<500℃). More important, to the best of our knowledge few investigators have studied the development of the acidity of the support surface with the increasing temperature.

In this study, the effect of the calcination temperature of the zirconia support on the physico-chemical properties of supported cobalt catalysts will be investigated. Furthermore, the performance of the impregnated catalysts in the Fischer-Tropsch synthesis will be investigated.

Experimentle

Preparation. Samples of zirconia were made by precipitation at room temperature. A solution of zirconyl chloride was added dropwise, concurrently with a solution of ammonia. Followed by washing and drying, calcination was carried out in a muffle furnace at various temperatures up to 800℃.

Samples of catalysts were prepared by the incipient wetness impregnation method.

Characterization. The surface areas, total volumes and pore size distribution of the samples were measured with ASAP-2000 Micromeritics instrument. XRD was recorded in Rigaku D/max-γA with Cu target at 40 kV and 100 mA. NH$_3$-TPD was carried out in a flow apparatus. The sample (100 mg) was pretreated at 600℃ in Ar for 2 h and saturated with NH$_3$ at 100℃. After removing the physically adsorbed ammonia, the sample was heated to 650℃ at 10 ℃/min in a Ar flow of 50ml/min.

Catalyst activity evaluation The performance of the catalysts in the Fischer-Tropsch synthesis was tested at 2 Mpa, 1000h^{-1} and a H$_2$/CO ratio of 2 in a fixed bed reactor of i.d.10mm. Following reduction in a flow of hydrogen at 400℃ for 6 h, the samples were switched to syngas. Mass balances were commenced after the reaction was on-line for 24 h. The CO, H$_2$, CH$_4$ and CO$_2$ products were analyzed on the TCD and the gas hydrocarbons were detected by the FID. Liquid and solid products were collected in a cold trap and a hot trap respectively and then were offline analyzed by the FID.

Results and Discussion

From the results summarized in **Table 1**, it is evident that the porous texture of the zirconia supports is different. With the increasing of calcination temperature, the surface area decreased and the average pore diameter increased. Once they were loaded by cobalt, an interesting phenomenon was observed. All catalysts had smaller surface area compared to their counterpart supports. It should be noted that the pore diameter of CoZr120 and CoZr400 was larger than their counterpart supports Zr120 and Zr400. Under this condition cobalt crystallite blocked smaller pores, thus the average pore diameter increased. On the other hand, Zr600 and Zr800 had a larger pore, so cobalt could fit in the pore and adsorbed on the inner wall, hence the average pore diameter of CoZr600 and CoZr800 decreased.

Table 1. Textural Properties of Samples

Samples	BET/m$^2 \cdot$ g^{-1}	Pore diameter/nm
Zr120	349	3.1
Zr400	101	6.6
Zr600	32	17.6
Zr800	15	25.5
CoZr120	133	4.8
CoZr400	68	6.7
CoZr600	26	14.7
CoZr800	13	22.5

The X-ray spectra (**Figure 1**, **Figure 2**) of Zr120 showed only two very broad bands in the range of 2θ from 18 to 40° and from 40 to 70°, this being indicative of a very low degree of crystallinity. The profiles of other zirconia supports showed that it consisted of mixtures of the stable monoclinic phase and the metastable tetragonal phase. The content of monoclinic phase increased with increasing calcination temperature. There were no Co$_3$O$_4$ diffraction peaks and tetragonal phase appeared in the profile of CoZr120 indicated that cobalt was highly dispersed and the loading of cobalt promoted the transformation from amorphous-phase zirconia to tetragonal-phase zirconia. Co$_3$O$_4$ diffraction peaks appeared on others suggests larger cobalt particle formed and the particle size of cobalt increased with the calcination temperature of the support increased.
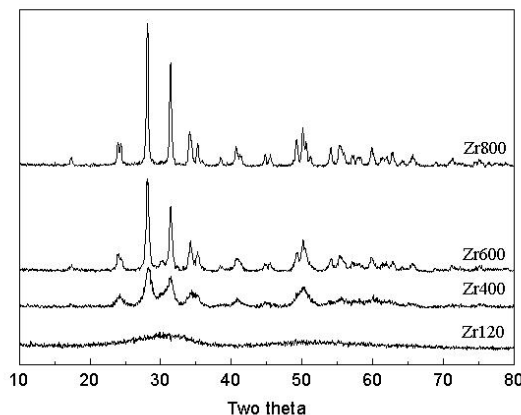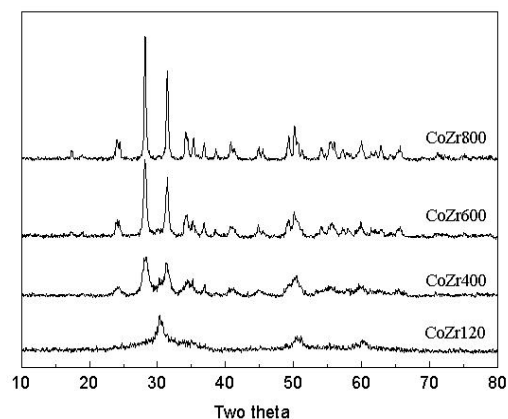

Figure 1 XRD profiles of ZrO$_2$ supports

Figure 2 XRD profiles of Co/ZrO$_2$ catalysts

Table 2 Properties of F-T Synthesis of Co/ZrO$_2$ Catalysts

Catalysts	θ /℃	Conversion/%	CH$_4$./%	C$_{5+}$/%
CoZr120	210	2.7	35.4	34.7
	220	16.3	34.7	36.6
CoZr400	210	21.4	32.1	43.4
	220	53.2	15.5	75.4
CoZr600	210	82.3	4.5	92.2
	220	94.2	3.7	93.0
CoZr800	210	66.9	8.9	86.0
	220	90.4	8.5	83.3

NH$_3$-TPD (**Figure 3**) results indicated that the acidity of the zirconia supports decreased with the increasing calcination temperature. Sample Zr120 had the strongest acidity and Zr800 had the weakest acidity. On the surface of Zr120, several kinds of acid centers existed. However, on the surface of Zr800 only weaker acid centers appeared and the stronger acid centers disappeared. This means that stronger acid centers on the surface of the support disappeared with the increasing calcination temperature.

Conclusions

The texture, crystallite phase and acidity of zirconia are greatly influenced by the calcination temperature of the support. Accompanying phase transformation and crystallite growth, the surface area of the support lost rapidly on calcination. Calcination may have a great influence on the surface acidity of zirconia and consequently affect the catalytic performance of the catalysts.

References
1 E. Iglesia, Appl. Catal. A., 1997, 161: 59-78
2   M. Valigi, D. Gazzoli, I.Pettiti, G.Mattei, S.Colonna, S.De Rossi, G. Ferraris. Appl. Catal. A., 2002, 231: 159-172
3 P.D.L.Mercera,J.G.Vanommen, E.B.M.Doesburg, A.J.Burggraaf, and J.R.H.Ross. Appl. Catal. A., 1990, 57: 127-148
4 V.G.Milt, E.A.Lombardo, M.A.Ulla. Appl. Catal.B:Environmental 2002, 37:63-73

Figure 3 NH$_3$-TPD profiles of ZrO$_2$ supports

The catalytic activity and selectivity of Co/ZrO$_2$ catalysts were shown in **Table 2**. CO conversion and products selectivity were strongly depended on the calcination temperature of the supports. With the calcination temperature of the supports increased, the catalytic activity and selectivity increased and catalyst CoZr600 which support was calcined at 600 ℃ had the optimal catalytic properties. The catalytic performance of CoZr800 depressed to a certain degree compared to CoZr600 due to the reduce of the surface area of Zr800 for sintering at higher calcination temperature.

Effect of Pretreatment on Reduction and Activity of the Boron-Modified Co/TiO$_2$ Fischer-Tropsch Catalyst

Jinlin Li[1] and Neil J. Coville[2]

1. College of Chemistry and Life Science, South Central University for Nationalities, Wuhan 430074, P.R. China
2. Department of Chemistry, University of the Witwatersrand, Johannesburg, Wits 2050, South Africa

Introduction

Supported cobalt catalysts have been widely employed for Fischer-Tropsch (F-T) synthesis of long chain hydrocarbons from Syngas [1]. Cobalt has certain advantages over iron or ruthenium as a catalyst, such as longer catalytic life time, less water-gas-shift activity and production of a modified product. As with many supported transition metal catalysts, the structure and catalytic properties of supported cobalt catalysts can be affected by cobalt loading, support, preparation method and pretreatment conditions. Numerous studies have focused on the pretreatment effects on the supported cobalt catalysts [2-10]. Calleja et al. [7] investigated the pretreatment effects on the Fischer-Tropsch reaction over a Co/HZSM-5 catalyst, and found that the calcination and reduction temperatures did not have an effect on the catalyst activity. The results obtained by Rathousky et al.[9], however, revealed that the pretreatment conditions had a significant effect on the catalytic properties of Co/Al$_2$O$_3$ and Co/SiO$_2$ catalysts. Turnover frequency (TOF) for the F-T reaction decreased with increasing calcination temperature for both Co/Al$_2$O$_3$ and Co/SiO$_2$. However, the total reaction rate increased for Co/Al$_2$O$_3$ while it decreased for Co/SiO$_2$ [8-10]. Belambe et al. [11] studied the pretreatment effects on the activity of a Ru-promoted Co/Al$_2$O$_3$ catalyst for F-T reaction. The calcination temperature was found to have a pronounced effect on the overall activity of the catalyst, but not on TOF. The reduction temperature had only a negligible effect on the overall activty and TOF.

The pretreatment effects on cobalt supported on titania have not prevously been reported in the literature. A previous investigation into the effect of boron on Co/TiO$_2$ catalysts indicated that boron decreases the reducibility of a Co/TiO$_2$ catalyst [12]. In parallel, the total CO hydrogenation rate was decreased by the addition of boron. TOF, however, was not affected by boron. In this study, the pretreatment effects on the catalytic properties of the boron-modified Co/TiO$_2$ catalyst were investigated. TPR, H$_2$ chemisorption and O$_2$ titration have also been used to check the pretreatment effects on the reducibility and dispersion of the catalyst.

Experimental

Catalyst preparation and pre-treatment. From the previous investigation, we found that the 10 wt% cobalt supported on the titania modified by 0.1 wt% boron catalyst had good activity for the F-T reaction [12]. This catalyst also showed good resistance for the sulfur poisoning [13]. This catalyst was thus used in this study. The titania modified by 0.1 wt% boron was prepared by pore volume impregnation of titania (Degussa P25, BET surface area: 50m^2/g; pore volume: 0.51ml/g) with a boric acid solution. The sample was dried at 120°C for 16 h then calcined at 400°C for 6 h. Cobalt (10 wt%) was deposited on the boron-modified titania by pore volume impregnation with cobalt nitrate solution. The sample was redried at 120°C for 16 h before calcination. The catalyst was calcined at different temperatures (200-400°C) using flowing air (GHSV = 2000 h^{-1}) for 16 h. After calcination, the catalyst was cooled down to room temperature and stored in a dry atmosphere. Before carrying out the F-T reaction, the catalysts were reduced for 16 hours at various temperatures (200-450°C) under flowing hydrogen (GHSV = 2000 h^{-1}).

Characterization techniques. Temperature Programmed Reduction (TPR), H$_2$ chemisorption and O$_2$ titration were used to characterize the catalysts. The methods used have previously been described [12, 13].

Reactor study. The catalysts, calcined and reduced at various temperatures, were tested for their activity and selectivity in the Fischer-Tropsch reaction in a fixed-bed flow reactor. The procedure has been described early [12,13]. The catalyst amount (~ 2 g) used for various experiments was kept constant. Fischer-Tropsch reaction was carried out at a pressure of 8 bar; a temperature of 230°C; GHSV of 350 h^{-1}(of CO) and a CO/H$_2$ 1:2 ratio for more than 400 h. Mass balances were carried out after the catalysts were on line for > 80 h. An on line GC , two off line GCs were used to analyse the composition of the product spectrum.

Results

TPR. The TPR spectra of the catalysts calcined at various temperatures are shown in Figure 1. Three reduction peaks can be observed for the catalyst calcined at 200 ^{o}C. The first peak, ranging from 180-200°C, was attributed to the reduction of the NO$_X$ group from Co(NO$_3$)$_2$. This peak became smaller when the catalyst was calcined at 300 ^{o}C and it disappeared after calcination at 400 ^{o}C due to the complete decomposition of nitrate[9]. Two peaks between 250-550°C were assigned to the reduction of Co$_3$O$_4$ supported on titania. The reduction of Co$_3$O$_4$ supported on titania proceeded in two stages [14], namely a primary reduction of Co$_3$O$_4$ to CoO and a subsequent reduction of CoO to Co metal. It is apparent that the Co$_3$O$_4$ reduction peaks shift to higher temperature and the area of reduction peaks decreases with increasing calcination temperature, suggesting that calcination decreases the reducibility of the catalyst.
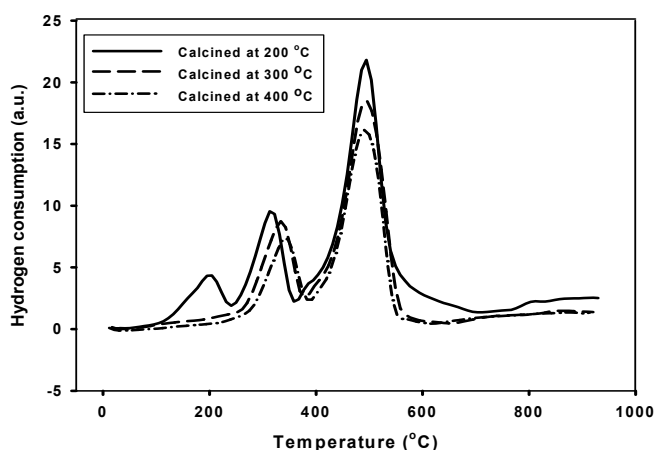

Figure 1. TPR profiles of the catalyst calcined at different temperature.

H$_2$ chemisorption and O$_2$ titration. The effects of pretreatment conditions on the percentage dispersion (% exposure) and percentage reduction of the catalysts were measured by H$_2$ chemisorption and O$_2$ titration. The results are shown in Tables 1, 2. With the exception of the dried catalyst, the percentage dispersion and percentage reduction of catalysts were found to decrease with increasing calcination temperature. As the reduction temperature was increased the % reduction did increase up to 300 ^{o}C after which there was little further effect.

The percentage dispersion increased initially and then decreased on increasing the reduction temperature. The maximum dispersion occurred in the catalyst reduced at 300 ^{o}C.

Fischer-Tropsch synthesis. The effect of calcination on the catalytic properties of the catalyst are shown in Table 1. The initial CO conversions were measured after about 30 min of reaction, while the steady-state CO conversions and the CO hydrogenation rates were measured after 80 h of reaction when the CO conversions are constant. The steady-state CO conversions decreased by about 25% from the initial conversions for all the calcination temperatures. Increasing calcination temperature was found to cause a linear decrease of both the steady-state CO conversion and total reaction rate for the F-T reaction. When the calcination temperature was increased from 200°C to 400°C, the reaction rate decreased by 30%. The product selectivity and α value were not affected by the lower temperature calcination. The higher temperature calcination shifted the product spectrum to the lower weight hydrocarbons. CO_2 was also found to be produced at the higher calcination temperatures. Turnover Frequency (TOF) was constant and independent of the calcination temperature. Table 2 shows the F-T reaction results obtained with the catalyst calcined at 300°C, but reduced at various temperatures. At this calcination temperature, the reduction temperatures have a significant effect on the F-T reaction rate. When the reduction temparature was increased up to 350 ^{o}C, the total reaction rate almost kept constant. Further increasing reduction temperature (400 and 450 ^{o}C) resulted in a clear decrease in CO conversion. The reduction temperature, however, did not have effect on TOF and product selectivity.

Discussion

Effect of pretreatment on the extent of reduction and dispersion of Co/B/TiO$_2$. The TPR and O$_2$ titration results revealed that the reducibility of the catalyst decreased with increasing calcination temperature. This may be due to (i) the smaller Co_3O_4 crystallite size (from XRD result, not shown) or (ii) the formation of surface cobalt compounds through metal-support interactions at higher calcination temperature [2]. Ho et al. [15] found a surface $CoTiO_3$-like phase in Co/TiO$_2$ catalysts, in addition to the Co_3O_4 phase, after calcination at 400°C. The amount of surface compound was dependent on the cobalt loading and calcination temperature. The "surface compounds" formation has been reported by others for non-promoted Co/SiO$_2$, Co/Al$_2$O$_3$ [2,3] and Ru-promoted Co/Al$_2$O$_3$ catalysts [11]. Our results revealed that the extent of reduction of the catalyst was not changed at the lower reduction temperatures (from 250 to 350 ^{o}C) but that the higher reduction temperatures (400, 450 ^{o}C) increased the extent of the reduction of the catalyst. This may be because the higher temperature causes the partial reduction of titania support resulting in a increase in the total reduction content, which was measured by total O$_2$ consumption [15].

The results shown in Table 1 reveals that the dispersion (% exposure) of the catalyst decreases with increasing calcination temperature. Hydrogen chemisorption has been reported to be suppressed for the catalysts which are poorly reduced [4-6]. Ho et al. [16] observed a decrease in chemisorption values with increasing calcination temperature for a Co/SiO$_2$ catalyst. Belambe et al. [11] also found the same effect for a Ru-promoted Co/Al$_2$O$_3$ catalyst. The results indicate that the higher reduction temperature gives a catalyst with a lower dispersion of catalyst, probably due to the strong metal-support interaction (SMSI). TiO$_2$ is a typical SMSI support. The higher temperatures can reduce TiO$_2$ to TiO$_X$ which blocks the surface metal cobalt sites and can cause loss of dispersion [17].

Effect of pretreatment on Fischer-Tropsch reaction of Co/B/TiO$_2$ catalyst. The data in Table 1 shows that the total CO hydrogenation rate decreases, and TOF is almost constant with increasing calcination temperature. This suggests that the decrease in total rate is the result of a decrease in the number of cobalt active sites due to the lower reducibility of the catalyst at the higher calcination temperature. This is consistent with the results obtained by other researchers for the SiO$_2$, and Al$_2$O$_3$ supported cobalt catalysts. Ho et al.[16] studied the effect of calcination temperature on the surface characteristics and CO hydrogenation activity of a Co/SiO$_2$ catalyst. They did not observe any change in TOF with calcination temperature. Belambe et al. [11] studied the effect of pretreatment on the activity of Ru-promoted Co/Al$_2$O$_3$ F-T catalyst. Their results indicated that the F-T reaction activity decreased with increasing calcination temperature. TOF was constant and was independent of the calcination temperature and the extent of reduction of catalyst. In contrast, the results obtained by Rathousky et al. [9] exhibited an increase in total CO hydrogenation activity for a Co/Al$_2$O$_3$ catalyst at higher calcination temperatures. They indicated that cobalt-aluminium oxides formed due to high calcination temperature which favored the increased yield of hydrocarbons.

Selectivity data and α value data revealed that the higher calcination temperature favored the lower weight hydrocarbons. Poorly-reduced catalysts contain a large fraction of stable surface oxide phases which are highly inactive for CO hydrogenation, but active for water-gas-shift reaction [18]. A higher H$_2$/CO ratio at the surface caused by the WGS reaction would promote the formation of lower weight hydrocarbons. The reduction temperature did not have a significant effect on the selectivity of the catalyst. This suggests that there is no change in the chemical properties of the active cobalt sites [11]. Calleja et al. [7] (for Co/HZSM-5 catalyst) and Fu and Bartholomew [6] (for Co/Al$_2$O$_3$ catalyst) also obtained similar results.

Conclusions

Pretreatment conditions were found to have a significant effect on the reducibility and activity of 10 wt% cobalt supported on titania catalyst modified by 0.1 wt% boron. The percentage reduction and percentage dispersion decreased with increasing calcination temperature. The higher calcination temperatures decreased the total CO hydrogenation activity, but did not affect the turnover frequency. The decrease in CO hydrogenation rate with increasing calcination temperature is attributed to a decrease in the number of surface active sites. The higher reduction temperature also decreased the total activity. This is the result of the loss of dispersion due to the TiO$_X$ blocking the surface active sites at the higher reduction temperatures. The higher calcination temperature shifted the product spectrum to the lower weight hydrocarbons, however, the reduction temperature did not affect the product selectivity.

References

(1) Anderson, R. B. Fischer-Tropsch Synthesis, Academic Press: New York, 1984.
(2) Chung, K. S.; Massoth, F. E. *J. Catal*. **1980,** 64, 320.
(3) Chin, R. L.; and Hercules, D. M. *J. Phys. Chem*. **1982,** 86, 360.
(4) Yoon, K. E.; Moon, S. H. *Appl. Catal*. **1985,** 16, 289.
(5) Ihm, S.; Lee, D.; Lee, J. *J. Catal*. **1988,** 133, 544.
(6) Fu, L.; Bartholomew, C. H. *J. Catal*. **1985,** 92, 376.
(7) Calleja, G.; Lucas, A.; Grieken, R. V. *Appl. Catal*. **1991**, 68, 65.

(8) Lapidus, A.; Krylova, A.; Rathousky, J. *Appl. Catal.* **1991**, 73, 65.
(9) Rathousky, J.; Krylova, A. Zukal, A. *Appl. Catal.* **1991**, 79,167.
(10) Lapidus, A.; Krylova, A.; Rathousky, J.; Jancakova, M. *Appl. Catal.* **1992,** 80, 1.
(11) Belambe, A. R.; Onkaci, R.; Goodwin, Jr. J. D. *J. Catal.* **1997**, 166, 8.
(12) Li, J.; Coville, N. J. *Appl. Catal. A:* **1999,** 181, 201.
(13) Li, J.; Coville, N. J. *Appl. Catal. A:* **2001**, 208, 177.
(14) Martens, J. H.; van't Blik, H. F. J. *J. Catal.* **1986**, 97, 200.

(15) Ho, S. W.; Cruz, J. M.; Houalla, M.; Hercules, D. M. *J. Catal.* **1992,** 135, 173.
(16) Ho, S. W.; Houalla, M.; Hercules, D. M. *J. Phys. Chem.* **1990,** 94, 6396.
(17) van de Loosdrecht, J.; van der Kraan, A. M.; van Dillen, A. J. *Catal. Lett.* **1996,** 41, 27.
(18) Reuel, R. C.; Bartholomew, C. H. *J. Catal.* **1984,** 85, 78.

Table 1. Effect of Calcination Temperature on the Catalyst

Tc (^{o}C)	Uncalcined	200	300	350	400
Dispersion (% exposure)	0.9	1.95	1.71	1.69	1.42
Reduction(%)	40.5	51	42.5	40.9	37.6
CO Conversion (mol%)					
Intial[a]	32	65	58	54	47
Steady state[b]	28.5	49	43	39	35
Reaction rate (S-S)					
(μmole/g cat./s)	0.46	0.79	0.69	0.63	0.58
TOF ($10^3 .s^{-1}$)[c]	24.5	25.9	24.2	24.9	26
Selectivity (%, by mass)					
C_1	15.6	11.2	11.5	13.2	19
C_2-C_4	14.2	12.7	9.4	11.5	15
C_5-C_{11}	48.7	47.6	52.3	49	46
C_{12}-C_{18}	16.3	17.5	19	18.5	15.5
C_{18+}	5.4	10.5	8.8	7.3	4.5
CO_2 selectivity (%, by mass)	0	0	0	0.8	1.5
α value	0.69	0.8	0.79	0.75	0.54

[a] Reduction temperature: 300°C; reaction conditions: T=230°C, P=8 bar, H_2/CO=2:1,measured after about 30min of reaction; [b] Measured after 80 h of reaction; [c] Based on total H_2 chemisorption.

Table 2. Effect of Reduction Temperature on the Catalyst

Tr (^{o}C)	250	300	350	400	450
Dispersion (%, exposure)	1.5	1.71	1.65	1.41	1.2
Reduction (%)	35	42.5	40.9	43.3	45.6
CO Conversion (mol%)[a]					
Initial	53	58	57.2	40	35
Steady state	39	43	42.5	33	29
Reaction rate (S-S)					
(μmole/gcat./s)	0.65	0.69	0.68	0.57	0.47
TOF ($10^3 .s^{-1}$)	26	24.2	24.6	25.6	24.5
Selectivity (%, by mass)					
C_1	12	11.5	13	14.9	12
C_2-C_4	8.9	9.4	11	10.6	10.4
C_5-C_{11}	49	52.3	53	50	51
C_{12}-C_{18}	21	18.5	16	17	17.9
C_{18+}	9	8.8	7	6.9	8.6
α value	0.73	0.79	0.75	0.69	0.76

[a] Calcination temperature: 300°C; reaction conditions: T=230^{0}C, P=8 bar, H_2/CO=2:1.

INFLUENCES OF REACTION CONDITIONS ON STREAM REFORMING OF METHANE OVER Ni/ZrO$_2$ CATALYST

Jie HU[1,2], Dehua HE[1], Yingwei LI[1], Hui WANG[1], Xin ZHANG[1]*

[1] State Key Laboratory of C$_1$ Chemistry and Technology, Department of Chemistry, Tsinghua University, Beijing 100084, P.R. China
[2] Henan Textile College, Zhengzhou, 450007, P.R. China

Introduction

The stream reforming of methane is a major process for producing hydrogen rich syngas in industry. Recently, the hydrogen production from the stream reforming of methane has attracted researchers' much attention in the world owing to the development of hydrogen fuel cell.[1-3] It has become a new hotspot to develop an efficient catalytic process for producing highly pure hydrogen gas.

Ni based catalysts have been mostly used in the stream reforming of methane in industry. In order to decrease the carbon deposit on the surface of Ni catalyst, a high H$_2$O/CH$_4$ ratio has been usually adopted. Furthermore, high reaction temperatures are required for the stream reforming of methane because it is a highly endothermic reaction. Therefore, highly thermostable and carbon deposit-resisting catalysts are desired in the stream reforming of methane. The selection of a suitable support may be an effective way for improving the thermo-stability and carbon deposit-resisting ability of the Ni based catalysts.

Recently, ZrO$_2$ has been widely investigated as a support in the carbon dioxide reforming of CH$_4$ to syngas and showed a quite positive effects on the catalytic performance.[4-6] ZrO$_2$ possesses both acidic and basic properties and shows a relatively high thermo-stability in catalytic reactions. Ni/ZrO$_2$ showed relatively high carbon deposit-resisting ability and stability in the carbon dioxide reforming of CH$_4$ to syngas. [7-8] Recently, we have investigated the performance of Ni/ZrO$_2$ catalyst in the stream reforming of methane. Here, we report the influences of reaction conditions and preparation conditions of the catalyst on the catalytic performance of Ni/ZrO$_2$.

Experimental

Preparation of samples. ZrO$_2$ was prepared by a precipitation method. A solution of ZrOCl$_2$•8H$_2$O was slowly added to a well-stirred ammonium solution at room temperature with controlling pH value at 10 during the precipitation. The obtained white precipitate was aged in the mother liquor for 2.5 h, filtered and washed with deionized water until no detectable Cl$^-$. The resultant paste was dried at 110 ^{o}C overnight and calcined at 650 ^{o}C for 5 h. Ni/ZrO$_2$ Catalyst was prepared by a wet impregnation method. An aqueous solution of Ni(NO$_3$)$_2$•6H$_2$O was added to ZrO$_2$ powder for the impregnation. After being evaporated and dried at 110 ^{o}C overnight, the sample was calcined at 650 ^{o}C for 3 h.

Reaction Procedure. The stream reforming of methane was carried out in a fixed-bed flow type quartz tube reactor (i.d. 8 mm). The catalyst (0.2 - 0.5g) was packed in the reactor and pretreated in a stream of 9%H$_2$-N$_2$ (120 ml/min) at 650 ^{o}C for 3 h. After reduction, the feed gas of stream, CH$_4$ and N$_2$ (H$_2$O/CH$_4$/N$_2$=2/1/2.67, 170ml/min) was introduced into the reactor and the reaction went on from 550 to 850 ^{o}C at atmospheric pressure. The reactor effluent was introduced into a condenser to condense the liquid components and then the dry effluent gas was analyzed by on-line gas chromatographs (TDX-01 column, TCD detector).

Characterization of catalysts. The crystal phases of ZrO$_2$ were determined by XRD (BrÜker, D8 Advance powder diffractometer) with CuKα radiation with a nickel filter. The crystal size of ZrO$_2$ was calculated from the half-width of the reflection of monoclinic phase determined by XRD. The specific surface area of ZrO$_2$ was measured by BET method on Micromeritics ASAP-2010C adsorptionmeter using N$_2$ as adsorption gas.

Results and Discussion

Under the reaction conditions of 650°C, H$_2$O/CH$_4$/N$_2$=2/1/2.67 and SV=1.98×10^{4}h^{-1}, 85% CH$_4$ conversion and 70% CO selectivity were obtained over 10%Ni/ZrO$_2$ catalyst in the stream reforming of methane. The influence of the reaction temperatures on the catalytic performance is shown in Fig. 1. In the temperature range of 650 ^{o}C~ 800 ^{o}C, the conversion of methane increased with the increase of temperatures and researched 100% at 800 ^{o}C. CO selectivity also increased monotonously with the increase of temperatures from 650 ^{o}C to 800 ^{o}C.
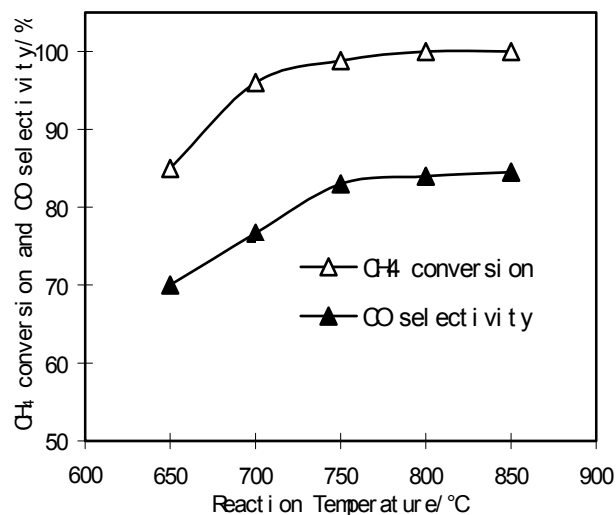

Figure 1. Catalytic performance of 10%Ni/ZrO$_2$ and effect of reaction temperatures. (H$_2$O/CH$_4$/N$_2$=2/1/2.67 and SV=1.98×10^{4}h^{-1})
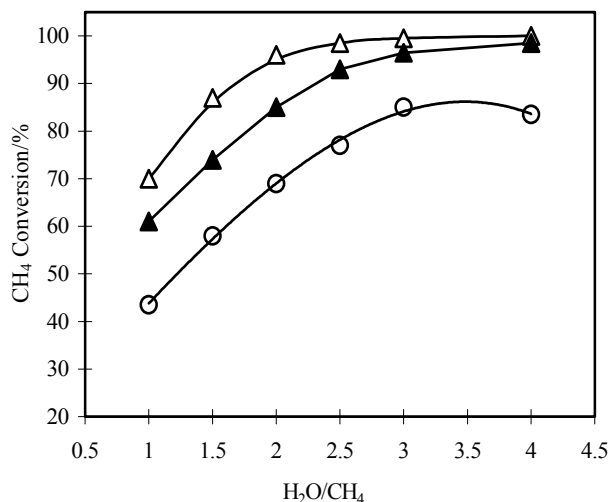
Figure 2. Influence of H$_2$O/CH$_4$ ratios on catalytic activity (10%Ni/ZrO$_2$, T$_{reduction}$ = 650°C, SV=1.98×10^{4}h^{-1}) Reaction temp.: Δ 700°C; ▲ 650 ^{o}C; ○ 600°C.

The effect of the ratios of H_2O/CH_4 on the stream reforming of methane was investigated in the range of H_2O/CH_4 ratio from 1/1 to 4/1 under the conditions of 600~700 °C and $1.98\times10^4h^{-1}$SV. The conversion of methane increased monotonously with the increase of H_2O/CH_4 ratios at all tested temperatures in the ratio of $H_2O/CH_4 = 1/1\sim3/1$ (Fig. 2). When the H_2O/CH_4 ratio was over 3.5, the conversion of methane kept constant at all tested temperatures. The effect of H_2O/CH_4 ratios on CO selectivity is shown in Fig. 3. The selectivity of CO decreased with the increase of H_2O/CH_4 ratios at all tested temperatures and dropped dramatically down to 12% at 600 °C when H_2O/CH_4 ratios researched 4/1.
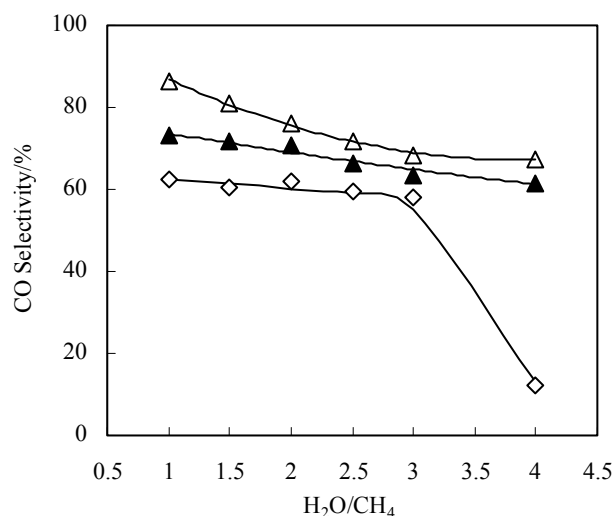
Figure 3. Influence of H_2O/CH_4 ratios on CO selectivity
(10%Ni/ZrO$_2$, $T_{reduction}$ = 650°C, SV=$1.98\times10^4h^{-1}$)
Reaction temp.: Δ 700°C; ▲ 650 °C; ◇ 600°C.

The influence of SV on the catalytic activity is shown in Fig. 4. Both methane conversion and CO selectivity decreased with the increase of SV in the range of $1.98\times10^4h^{-1} \sim 9.74\times10^4h^{-1}$ at 550 ~ 850 °C. The increase of space velocity would result in short contact time of the reactants with the surface of catalyst, which will be unfavorable for the adsorption and activation of the reactants and leads to the decrease of CH$_4$ conversion. It was reported that CO and CO$_2$ would be formed in parallel in the stream reforming of methane[9] and our experiment results of the influent of SV on CO selectivity seem to support this supposition.

The support ZrO$_2$ was calcined at 550~850 °C before impregnation with the solution of Ni(NO$_3$)$_2$•6H$_2$O. The characterization of the support showed the specific surface area of ZrO$_2$ decreased evidently and its crystal size increased in some sort with the increase of calcination temperature. Influence of calcination temperatures of the support ZrO$_2$ on the catalytic performance at the reaction temperatures of 650 °C and 800°C is shown in Table 1. Changing the calcination temperatures of the support ZrO$_2$ showed no evident influence on the conversion of methane and CO selectivity. The effect of the reduction temperatures of Ni/ZrO$_2$ catalyst on the catalytic performance was also examined in the reduction temperature range of 450~750°C. Under the reaction temperature of 650 °C, the catalyst reduced at 550°C showed a higher CH$_4$ conversion than at other reduction temperatures. But no influence was found on CO selectivity when changing the reduction temperature of Ni/ZrO$_2$ catalyst.

The stability of Ni/ZrO$_2$ was also examined under the reaction conditions of 650 °C, H_2O/CH_4 =1.5/1 and 5.1×10^4 mL/g-cat•h for 30 hours. Although the tested times (30 hours) was not enough for check the stability of the catalyst, both CH$_4$ conversion and CO selectivity did not decrease and kept constant during the tested period.
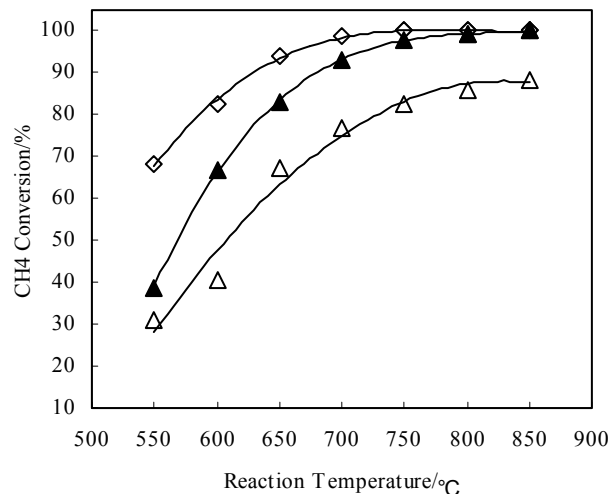
Figure 4. Influence of space velocities on catalytic activity
(10%Ni/ZrO$_2$, $T_{reduction}$ = 650°C, $H_2O/CH_4/N_2$=2/1/2.67)
◇ : SV=$1.98\times10^4h^{-1}$; ▲: SV=$4.87\times10^4h^{-1}$; Δ: SV=$9.74\times10^4h^{-1}$.

Table 1 Influence of calcination temperatures of support

Calcination temperature / °C	Reaction temperature / °C			
	650 °C		800 °C	
	CH$_4$ Conv. /%	CO Sele. /%	CH$_4$ Conv. /%	CO Sele. /%
550	65.8	61.0	94.3	82.3
650	69.8	60.7	96.3	82.1
750	65.4	63.2	95.8	82.3
850	65.6	62.6	96.0	83.3

References
1 Solh T. E., Jarosch, K., de Lasa, H. I, Appl. Catal. A: General. **2001**, *210*, 315-324
2 Dong W.S., Roh H.S., Jun K.W., Park, S.E., Oh, Y.S., Appl. Catal. A: General, **2002**, *226 (1-2)*, 63-72
3 S.Hegarty M.E., O'Connor A.M., Ross J.R.H., Catal. Today, **1998**, *42*, 225-232
4 Bitter J.H., Seshan K., Lercher J. A., J. Catal., **1999**, *183*, 336
5 Wei J.M., Xu B.Q., Li J.L., Cheng Z.X., Zhu Q.M., Appl. Catal. A, **2000**,*196*, L167-172
6 Wei J.M., Xu B.Q., Cheng Z.X., Li J.L., Zhu Q. M., Stud. Surf. Sci. Catal., **2000**, *30*, 3687-3692
7 Wei J.M., Xu B.Q., Sun K.Q., Li J.L., Zhu Q. M., Chem. J. Chin. Univ., **2002**, *23*, 2196
8 Xu B.Q., Wei J.M., Yu Y.T., Li J.L., Zhu Q. M., Top. Catal., **2003**, *22 (1/2)*, 77
9 Ho K., Hughes R., Chemical Engineering Journal, **2001**, *82(1-3)*, 311-328

FISCHER-TROPSCH PRINCIPLES OF CO-HYDROGENATION ON COBALT CATALYSTS

Hans Schulz

University of Karlsruhe
Engler-Bunte-Institute
76131 Karlsruhe, Germany

Introduction

CO-hydrogenation on the metals Ni, Ru, Co, and others, commonly yields methane, as discovered by Sabatier and as thermodynamically to be expected. But at adequate catalyst preparation, at relatively low temperature, methane becomes a minor product and the formation of linear olefins and paraffins dominates. The conclusion has then to be "methane formation is frustrated in the Fischer-Tropsch regime", this allowing for chain growth, the intrinsic characteristic of Fischer-Tropsch synthesis. It is outlined in the lecture in more detail how **frustration of distinct basic reactions** rules the Fischer-Tropsch regime - rather than promotion of others.

A further principle of FT-synthesis with cobalt is its extreme **dynamic character** responding sensitively with its product composition (chain length, branching, olefin/paraffin-ratio, oxygenates) against changes of temperature and of the partial pressures of CO, H_2 and H_2O (most pronouncedly p_{CO}, in contrast to the behavior of iron as catalyst).

With cobalt (also Ni and Ru) it appears that the reactants and intermediates are dynamically featuring as part of the active catalytic sites, such behavior is well-known in homogeneous catalysis with transition metal complexes.

The principle of **self-organization** for attaining the steady-state conversion is a very important feature of FT-synthesis with cobalt as the catalyst. Obviously, a thermodynamically driven segregation of the cobalt surface and thereby **sites disproportionation** occurs (Fig. 1). This follows from time resolved measurements of activity and selectivity and related kinetic modeling together with surface structure imaging.
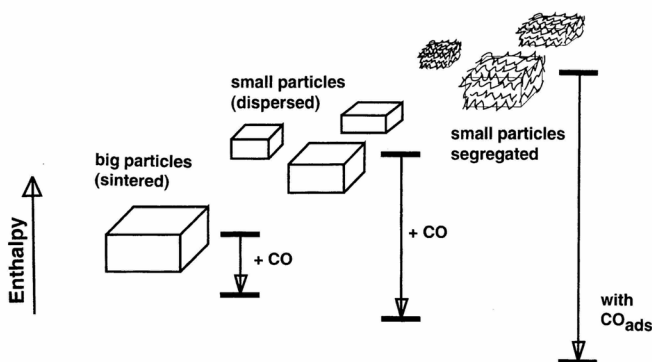

Figure 1. Thermodynamic view of cobalt surface segregation under FT-conditions: Segregation is favored against sintering and surface-annealing by CO-chemisorption. An equilibrium state of surface reconstruction is being approached.

The principle of **spatial constraints** applying to distinct basic reactions appears additionally to operate. To elaborate the influences of these principles from experimental results, the conversion is modeled as a kind of **polymerization** and the relevant influences are specified as moderating ideal polymerization.

Results and Discussion

As a function of time (duration of the experiment) it is investigated how the steady-state Fischer-Tropsch regime is established:

- The reaction rate (of CO-consumption) increases (factor of 3 to 10),
- The chain growth probability increases,
- Methane selectivity decreases,
- Secondary olefin hydrogenation and isomerization decrease,
- Branching probability decreases.

These kinetic changes are explained in conjunction with catalyst restructuring, caused by strong CO chemisorption, proceeding as segregation of the catalyst surface to increase the number of active sites and disproportionate on-plane-sites into on-top-sites and in-hole-sites, the on-top-sites exhibiting catalytic properties, resembling those of transition metal complexes and the in-hole-sites showing high activity for dissociation (of CO), whereas the common on-plane-sites are much deactivated through CO-adsorption (and methyl-coverage). Of course, such steady-state should be highly dynamic.

The preferred **monomer** for chain growth appears to be the methylene species, as concluded from the observed reversible terminal CH_2-splitting from added labeled olefins, relating the chemistry on the on-top-sites to that of transition metal carbene complexes.

Ethene to act as a monomer is also observed as a minor reaction, to relate the chemistry on the growth sites to homogeneous olefin polymerization. CO as a monomer is also possible (as related to olefin hydroformylation), however, only as a minor reaction to produce alcohols and aldehydes.

Spatial constraints at the growth sites are concluded to operate as for preferred olefin readsorption at their alpha-position, for the decline of branching with increasing size of the growing chain and for suppressed desorption after branching.

The most important principle of any FT-regime appears to be **frustration of desorption** and this to concern the reaction of associative desorption of an alkyl together with a H to desorb as a paraffin molecule. This causes the accumulation of **deactivating methyl species** on the catalyst surface (mainly on on-plane-sites) and allows for chain growth to become dominant.

In **conclusion**, the important process of surface segregation and thereby active sites generation and moderation can be influenced by promotors and the conditions of segregation in order to design catalysts for optimal technical application.

SYNTHESIS AND CHARACTERIZATION OF NANO-SIZED IRON PARTILCES ON A POLYSTYRENE SUPPORT AS POTENTIAL FISCHER-TROPSCH CATALYSTS
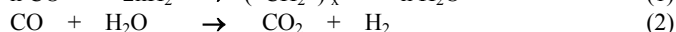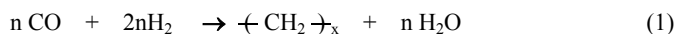
Amruta Desai[1], Devinder Mahajan[1,2], and Miriam Rafailovich[2]

[1]Energy Sciences & Technology Department, Brookhaven National Laboratory, Upton, NY 11973-5000, USA.
[2]Department of Materials Science & Engineering, Stony Brook University, Stony Brook, NY 11794 USA

Introduction

Iron is inexpensive that makes it the most desirable material to catalyze Fischer-Tropsch (F-T) synthesis[1]. Iron is also desirable because the hydrocarbons produced are high in olefinic content. Prior to World-War II, the commercial plants utilized Fe-based catalysts in Germany and South Africa. The Fischer-Tropsch reaction is best described by Equation 1:

$$n\,CO \;+\; 2nH_2 \;\rightarrow\; +\!\left(CH_2\right)\!\!\rightarrow_x \;+\; n\,H_2O \qquad (1)$$
$$CO \;+\; H_2O \;\rightarrow\; CO_2 \;+\; H_2 \qquad (2)$$

The F-T reaction is always accompanied by the well-known water-gas-shift reaction (WGSR) (Equation 2). The WGSR reaction is facile under the temperature (260° - 280^oC) and the pressure (2000 – 3000 kPa) conditions under which Fe-catalyzed F-T reaction takes place. The value of x in Equation 1 determines the product distribution that can range from methane for x = 1 to high molecular weight waxes.

One of the crucial problems associated with the F-T reaction is the following. As the F-T reaction proceeds, the volatile (low molecular weight) hydrocarbons exit the reactor by the flowing gas but the higher molecular weight waxes remain in the reactor. After certain period on-line, the waxes accumulate to a point that it encapsulates the catalyst and reduces its effectiveness. Moreover, after the F-T reaction, the catalyst/waxy product separation is problematic to regenerate the catalyst.

We recently reported[2] the use of nano-sized unsupported Fe particles in an attempt to enhance the space-time-yield (STY) during the F-T reaction. But a facile method to synthesize nano metal catalysts remains a challenge. New methods are sought to facilitate synthesis of supported nano materials for potential applications in catalysis, gas separation and storage. Polymers provide structural flexibility than well-studied inorganic frameworks such as zeolites. To this effect, there are reports of the use of polymers as a support to stabilize colloidal iron dispersions[3], synthesis of highly porous metal-organic frameworks consisting of supertetrahedron clusters when capped with monocarboxylates[4] that are stable up to 300^oC and materials based on dendrimers in which metal nanopartilces are encapsulated in the dendritic framework[5]. This paper summarizes our attempt to synthesize nano-sized materials that could be used to enhance STY yield and provide a pathway to an effective catalyst/wax separation. We report herein a facile synthesis of supported Fe nano particles that are embedded in the polystyrene matrix.

Experimental

Synthesis of Nano Fe particles Supported on Polystyrene (Fe-PST). Polystyrene is a porous polymer that could provide selective porosity to gas absorption and separation. Moreover,

polystyrene (PS) may be able to remain stable under reaction conditions of higher temperature (250^oC - 300^oC) that are required for F-T synthesis. The strategy was to attempt to simultaneously synthesize polystyrene from the styrene monomer to be used as the supporting matrix, while producing the nano-sized Fe particles at the same time. Though the polymerization process requires initiators, we used the produced nano-sized Fe particles as initiators to polymerize the monomer styrene and create its own matrix to envelope the nano Fe particles. The polymer matrix may be suited to protect the Fe particles without changing their properties.

The procedure developed to produce polymer-supported nano Fe metal particles involved thermal decomposition of $Fe(CO)_5$ in the presence of a monomer that was allowed to concurrently polymerize. The method involved mixing 50ml purified styrene monomer with 50 ml hexadecane solvent in a glass flask, adding 1.2 ml $Fe(CO)_5$ after purging with argon, stirred and heated at 100^oC at ambient atmosphere. The solution turned black in a few minutes after heating was initiated indicating the formation of zero-valent Fe. The darkening of the solution was followed by gradual solidification of the solution over time indicating polymerization of styrene. The product in this case was a slightly brownish solid in which black Fe particles could be distinctly seen.

Characterization of Fe-PST. The NSF funded Garcia Center for Engineered Polymer Interfaces in the Materials Science and Engineering Department at SUNY at Stony Brook houses state-of-the-art instruments to characterize polymeric materials. Characterization of the samples included using the Transmissions Electron Microscopy (TEM), Differential Scanning Calorimeter (DSC), Fourier Transform Infrared Spectroscopy (FTIR), Gel Permeation Chromatography (GPC), Electron Paramagnetic Resonance (EPR), and measurement of magnetic properties.

Results and Discussion

The overall observed reaction can be described as follows:

$$(3)$$
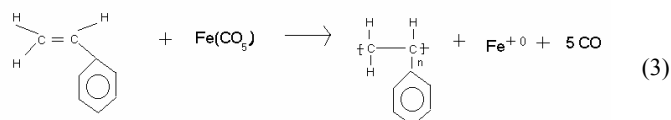
Mechanistically, the reaction sequence is better described as a combination of Reactions 4 and 5:

$$Fe(CO)_5 \;\overset{\Delta}{\Rightarrow}\; \text{"Fe"} + 5\,CO \qquad (4)$$

$$Styrene \;\overset{\text{"Fe"}}{\Rightarrow}\; Fe\text{-}Polystyrene \qquad (5)$$

The $Fe(CO)_5$ decomposition reaction is written first in the sequence because we recently reported[6] the rate constant for this reaction to be $3 \times 10^{-6}\,s^{-1}$. The reaction rate for Reaction 4 is far greater than the styrene polymerization during Reaction 5 as we observed the solution viscosity that increased slowly with time and took four days till the contents of the flask could not be further stirred. Therefore, we infer the role of Fe nano particles, initially produced during the reaction, appears to initiate polymerization of styrene. The synthesized material is best described as polystyrene containing nano particles of Fe (Fe-PST).

The synthesized material contains nano particles of Fe in polystyrene matrix. The physical appearances of the materials are as follows. As shown in Figure 1, pure polystyrene exists as a white material whereas polystyrene containing Fe (Fe-PST) becomes

colored. The freshly prepared Fe-PST material is black that slowly changes to brick red on exposure to air. The homogeneous spread of the brick red color also shows that the Fe particles do not just reside on the polystyrene surface but rather are highly dispersed throughout the matrix. The brick red color is likely due to the oxidation of zero-valent iron to iron oxide.

Figure 1: Physical appearance of: pure polystyrene (left) and thermally prepared Fe-PST material (right). Note that as shown, the brick red color in the right sample is due to oxidation that was originally black (prior to oxidation) as seen at the core of the sample.

The Fe-PST material was characterized by various techniques. The TEM of the sample is shown in Figure 2. It is evident that the Fe particles are part of the polystyrene matrix that are seen as dark spots in the TEM image shown in Figure 2. The mean particle size was calculated to be 44 nm.

Figure 2. TEM micrograph of Fe-PST material prepared by thermal treatment of a mixture containing $Fe(CO)_5$ and styrene monomer.

The average molecular weight of a polymer sample are usually expressed as number average, M_n and weight average, Mw, values. The gel permeation chromatography (GPC) was used in this work to determine the molecular weight distribution of polystyrene in the thermally synthesized Fe-PST material. The GPC chromatogram describes the relative amount of polymer molecule as a function of molecular sizes. The molecular weight is found in order to ensure that the synthesized matrix consists of reasonably large polystyrene molecules, establishing, the success of the polymer synthesis reaction and giving information of the polymerization process. For a purified polystyrene sample with EPR data, the weight average molecular weight, M_w, was found to be 59.6K and number average molecular weight, M_n, 19.3K with the highest population at M_p= 49.9K (Figure 3). The polydispersity, M_w/ M_n of this sample is about 3, which is a value higher than normal low conversion radical polymerization; this polydispersity is expected for high conversion systems. Thus the GPC and the TEM data show that the nano Fe particles of a mean size of 44 nm are formed and get well dispersed in the polystyrene polymer whose average molecular weight is 59,600.
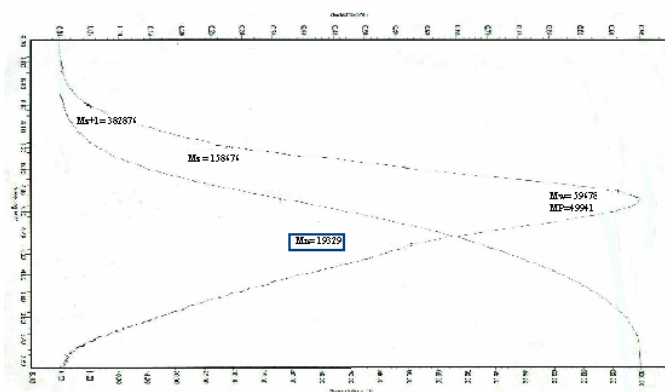

Figure 3. The chromatogram depicts the molecular weight distribution for the thermally synthesized sample. M_w = 59.6K; M_n= 19.3K and M_p= 49.9K. A curve of cumulative amount is also shown.

Conclusions

To conclude, a polymeric material containing nano particles of Fe(0) and polystyrene can be conveniently prepared by the thermal treatment of a solution containing iron pentacarbonyl and styrene monomer in hexadecane. The TEM data show that the mean particle size of synthesized Fe particles is 44 nm and the Fe particles are well dispersed throughout the polystyrene matrix. The Fe-PST material, as prepared under an inert atmosphere, contains Fe particles in zero-valent oxidation state that appear as black particles. On exposure to air, the Fe slowly starts to oxidize to a brick red material that is likely to be iron oxide.

Further characterization of these materials by Differential Scanning Calorimetry (DSC), Fourier Transform Infrared Spectroscopy (FTIR), Electron Paramagnetic Resonance (EPR), and measurement of their magnetic properties is underway to establish their morphology, rheology and other structural properties. The DSC measurement will allow us to establish thermal stability of these materials to allow us to evaluate their potential as Fischer-Tropsch catalysts.

References
1. Dry, M.E. in: J.R. Anderson, M. Boudart (Eds.), Catalysis, Science and Technology, Springer-Verlag, Berlin, 1981, p. 159 and references therein.
2. Mahajan, D., Gütlich, P., Stumm, U. Catal. Commun. **4** (2003) 101-107.
3. Smith T. W., Wychick D. J. Phys. Chem., **84** (1980) 1621-1629.
4. Li, H., Eddaoudi, M., O'Keeffe, M., Yaghi, O. M. Nature, **402** (1999) 276-279.
5. Tully, D.C., Frechet, M. J. Chem. Commun., (2001) 1229-1239.
6. Mahajan, D., Papish, E.T., Pandya K. Ultrasonic Sonochem., submitted (2003).

HIGH PRESSURE CO₂ REFORMING OF CH₄ OVER NI/MGO CATALYST DERIVED FROM NANO-MgO

Yu-He Wang, Bo-Qing Xu and Qi-Ming Zhu

State Key Lab of C₁ Chemistry and Technology
Department of Chemistry, Tsinghua University
Beijing 100084, China

Introduction

There has been a general interest in recent in the more efficient use of natural gas (methane) and in the decrease of carbon dioxide in the atmosphere. The production of synthesis gas by CH_4/CO_2 reforming is one of the attractive routes for the utilization of CH_4 and CO_2. The product mixture of this reaction from a stoichiometric (1:1) feed has a high CO/H_2 ratio that is suitable for methanol and F-T synthesis, because low CO/H_2 ratios favor methanation and suppress chain growth [1]. Great efforts have been focused on the development of catalysts that shows high activity and stability.

Generally, CH_4 is preserved at high pressures in natural gas fields, and most F-T synthesis and methanol synthesis from CO/H_2 are performed at high pressures in the GTL (gas to liquid) process. Hence, from an economical point of view, the CH_4/CO_2 reforming should be carried out at high pressures in such a process [2]. In addition, in terms of the utilization of synthesis gas, the compressed synthesis gas is more convenient. It has been proposed that researchers must appreciate that the key problem is catalyst life at high pressures because customers need H_2 at >1.0 MPa and compression of large volumes of product gas is not very acceptable [3]. As it is well known that higher pressures favor coking and deactivation of catalysts in the CH_4/CO_2 reforming to synthesis gas, researches of the reforming reaction at high pressures are required. However, most of the researches were performed at atmospheric pressure, and only a few studies were conducted at high pressures [2-8]. To date no high stable Ni-based catalysts are reported in the dry reforming of methane at high pressures. Our searches have shown that Ni/MgO-AN catalyst (Ni-loading: 8.8%wt), the support of nano-MgO (named as MgO-AN) prepared by thermal processing of an alcogel of $Mg(OH)_2$, was extremely stable at 973-1123 K for CH_4/CO_2 reforming at atmospheric pressure [9]. In this paper, we have explored the catalytic performance of Ni/MgO-AN at high pressures CH_4/CO_2 reforming.

Experimental

Catalyst preparation and characterization. Magnesia support was prepared by sol-gel method with $MgCl_2 \cdot 6H_2O$ (A.R., Beijing Yili Chemical Reagent Co.) and $NH_3 \cdot H_2O$ (A.R., Beijing Yili Chemical Reagent Co.). Obtained $Mg(OH)_2$ hydrogel was changed to alcogel by washing with ethanol and then calcined at 650 ºC in flowing N_2 for 5 h, named as MgO-AN (S_{BET} = 59.3 m²/g). Catalyst of Ni/MgO-AN (Ni-loading: 8.8%wt, S_{BET} = 48.1 m²/g) was prepared by wet impregnation of an aqueous solution of $Ni(NO)_3 \cdot 6H_2O$ (A.R., Beijing Yili Chemical Reagent Co.) onto MgO-AN support [9]. The obtained paste was dried at 120 ºC overnight and then calcined at 650 ºC for 5 h in air. Temperature programmed oxidation (TPO) experiments of carbon species formed on catalysts were performed on a thermogravimetric analyzer (SETARAM TGA 92) in flowing air. TEM measurements were performed on a H-800 electron microscope.

Catalyst tests and product analysis. A catalytic activity test of CH_4/CO_2 reforming was carried out in a fixed-bed continuous-flow reaction system. The reactor was made of a quartz tube (7 mm i.d.) tightly fixed in a stainless steal tube. A Viton O-ring pressed by a locking nut was used to prevent the gas from leaking into the ringed gap so as to eliminate the influence of the metal wall. The reaction

temperature was measured by a thermal couple, which was protected with a quartz tube (6 mm o.d.) with a dead end. The flow rate of CH_4/CO_2 = 1/1 (Huayua gas chemical & technology Ltd. Co., Beijing) was controlled by a mass flow controller (Brooks 5850E) and the pressure of the reaction system was controlled by a back-pressure regulator (Type 806, Badger Co.). The outlet gas was cooled to remove H_2O and sampled by a six-port valve and analyzed by an on-line gas chromatograph (Varian 3400 GC, Ar carrier and 2 m TDX-01 column) with a TCD detector. The catalyst bed contains 40 mg Ni/MgO-AN that was diluted with 100 mg inactive α-Al_2O_3 (Homemade by calcining the commercial Al_2O_3 to 1350 ºC). Before the reaction, the catalyst was reduced with a flowing 5.0% H_2/N_2 at 1123 K for 1 h. Blank reaction tests showed that CH_4 conversion is less than 2.0% under the current reaction conditions within 50 h.

Results and Discussion

Figure 1 shows the dependence of CH_4 conversion and CO yield on the time on stream for 8.8%Ni/MgO-AN catalyst with GHSV=1.6×10^4 ml/h·g_{cat} under 1.5 MPa at 1023 K. Results indicate that activity of the catalyst decreases with increasing the reaction time-on-steam (TOS) up to 10 h, but no further decline is observed thereafter when the reaction was continued to TOS = 50 h. Both CH_4 conversion and CO yield can reach a constant value, 23.5% and 29.6% respectively. The CH_4 conversion and CO yield can be estimated to be 39.5% and 49.5% on the basis of thermodynamic calculation in CO_2 reforming CH_4 (CH_4/CO_2 = 1/1, total pressure 1.5 MPa, reaction temperature 1023K) at equilibrium.
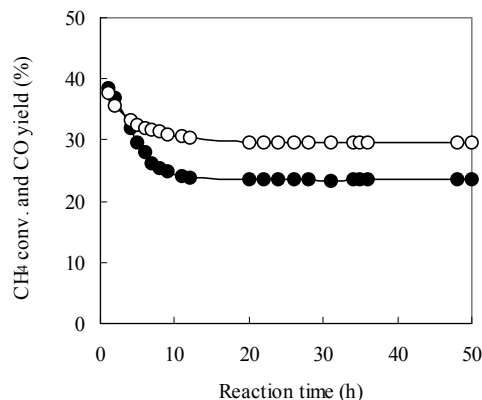

Figure 1. Stability test for 8.8%Ni/MgO-AN at 1.5MPa 1.6×10^4 ml/h·g_{cat} 1023K CH_4/CO_2=1/1. —○— CO yield —●— CH_4 conversion

Pressure and space velocity dependences studies were conducted at pressures varying from 1.0 to 2.0 MPa and at space velocity from 1.2×10^4 to 2.0×10^4 ml/h·g_{cat}. Results show that the stability in these different reaction conditions is the same with the behavior depicted in Figure 1. **Figure 2 and 3** show the effect of pressure and space velocity on CH_4 conversion and CO yield. These results show CH_4 conversion and CO yield decreased with increasing the reaction pressure as well as with increasing the reactant space velocity as expected from thermodynamics analysis. The effect of space velocity on activity implied that the reaction system had eliminated the contribution of mass-transport control.

It has been recognized that carbon deposition is the main cause of the deactivation of supported nickel catalysts in the reforming of CH_4 with CO_2 [10]. TPO measurements (**Figure 4**) show that the amount of carbon deposition on the used catalyst increases slowly with reaction time up to a constant value within 50 h. After 10 h on stream the loading of carbon deposition does not increase any more

with reaction time. The increasing tendency of carbon deposition is inverse proportion with the decreasing tendency of the CH_4 conversion and CO yield during the initial period. Although carbon was deposited on the catalyst, the activities became unchanged thereafter after 10 h on stream. The results imply that the carbon deposition did not block all active sites [5].
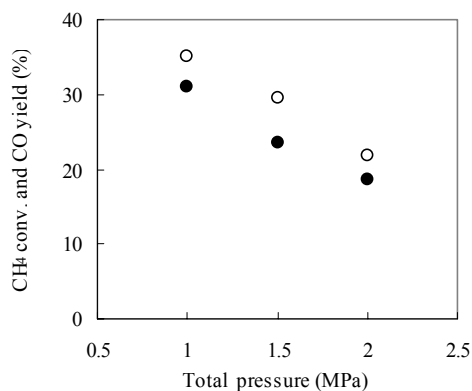

Figure 2. Dependence of activity on total pressure over 8.8%Ni/MgO-AN at 1.6×10^4 ml/h·g_{cat} 1023K CH_4/CO_2=1/1 TOS=50h. —○— CO yield —●— CH_4 conversion
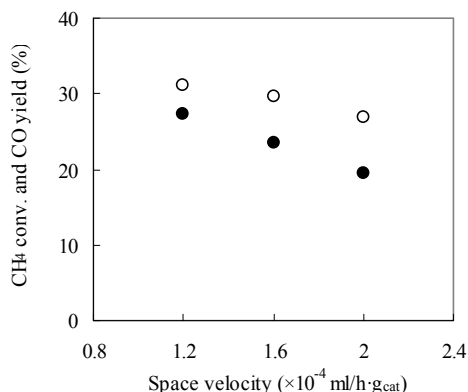
Figure 3. Dependence of activity on space velocity over 8.8%Ni/MgO-AN at 1.5MPa 1023K CH_4/CO_2=1/1 TOS=50h. —○— CO yield —●— CH_4 conversion

The sinter of nickel is another cause of deactivating catalysts in the CH_4/CO_2 reforming [10]. The TEM image of reduced catalyst shows that the metal nickel was dispersed on the magnesia supports uniformly (**Figure 5A**). In the TEM observation of used catalyst, larger nickel particle are found on the surface of catalyst **(Figure 5B)**. At the same time, TEM measurements revealed that the carbon deposits were of the filamentous types that can be removed by reaction with CO_2. The TEM image shows that the filamentous carbon grows from the larger nickel particle and some small nickel crystal stand on the tip and the middle of the filamentous carbon.

From the stable activity and unchanged amount of carbon deposition after 10 h on stream, it can be concluded that the catalyst deactivation was closely related with the amount of carbon deposits on the catalyst. The stable catalysis of Ni/MgO-AN catalyst seems to be associated with its ability to avoid formation of graphitic carbons and to maintain a dynamic equilibrium of the filamentous carbons with the reactant and product molecules at the catalyst surface.
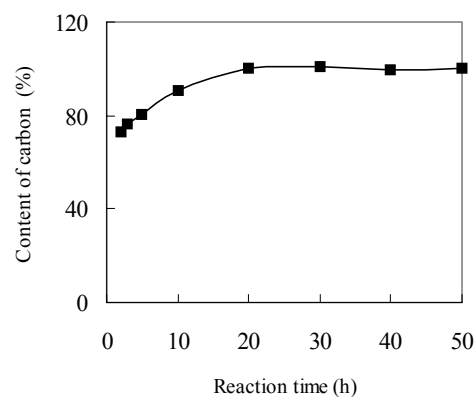
Figure 4. Dependence of the amount of carbon deposition on reaction time over 8.8%Ni/MgO-AN at 1.5MPa 1.6×10^4 ml/h·g_{cat} 1023K CH_4/CO_2=1/1. —○— CO yield —●— CH_4 conversion
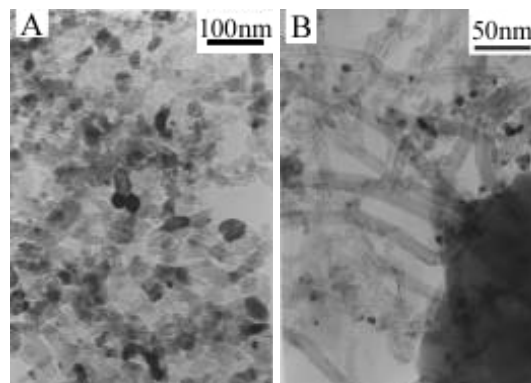

Figure 5. TEM images of fresh and used 8.8%Ni/MgO-AN
A. Reduced on flowing 5.0% H_2/N_2 for 1h at 1123K
B. After 50h on stream at 1.5MPa 1.6×10^4 ml/h·g_{cat} 1023K

References
1. Bradford, M.C.J., Vannice, M.A., *Appl. Catal.* 1996, 142, 73-96.
2. Nagaoka, K., Takanabe, K., Aika, K., *Chem. commun.*, 2002, 1006–1007.
3. Tomishige, K., Himeno, Y., Matsuo, Y., Yoshinaga, Y., Fujimoto, K. *Ind. Eng. Chem. Res.*, 2000, 39, 1891-1897.
4. York, A.P. E., Claridge, J.B., Brungs, A.J., Tsang, S.C., Green, M.L.H., *Chem. Commun.*, 1997, 39-40.
5. Nagaoka, K., Okamura, M., Aika, K., *Catal. Commun.*, 2001, 2, 255-260.
6. Shamsi, A., Johnson, C.D., *Environmental Challenges and Greenhouse Gas Control for Fossil Fuel Utilization in the 21st Century*, 2002, 269-283.
7. Pan W., Song C.S.，*Abstracts of Papers of the Am. Chem. Soc.*, 219: 71-Petr. Part. 2, Mar. 26, 2000.
8. Brungs, A.J., York, A.P.E., Claridge, J.B., Márquez-Alvarez, C., Green, M.L.H., *Catal. Lett.*, 2000, 70, 117-122.
9. Xu B.Q., Wei J.M., Wang H.Y., Sun K.Q., Zhu Q.M., *Catal. Today*, 2001, 68, 217-225.
10. Tomishge, K., Chen Y.G., Fujimoto, K., *J. Catal.*, 1999, 181, 91-103.

Fischer-Tropsch Synthesis: Overview of Reactor Development and Future Potentialities

Burtron H. Davis

Center for Applied Energy Research, University of Kentucky
2540 Research Park Drive
Lexington, KY 40511

Since its discovery in the 1920s, the Fischer-Tropsch Synthesis (FTS) has undergone periods of rapid development and periods of inaction. Within ten years of the discovery, German companies were building commercial plants. The construction of these plants stopped about 1940 but existing plants continued to operate during WWII.

Two types of reactors were used in the German commercial plants: the parallel plate reactors and a variety of fixed-bed tubular reactors. For the parallel plate version, the catalyst bed was located in tubes fixed between the plates which was cooled by steam/water that passed around the tubes within the catalyst bed (figure 1). In another version, the reactor may be regarded as finned-tube in which large fins are penetrated by a large number of parallel or connected catalyst filled tubes. Various designs were utilized for the tubular fixed bed reactor with the concentrical tubes being the preferred one. This type of reactor contained catalyst in the area between the two tubes with cooling water-steam flowing through the inner tube and on the exterior of the outer tube (figure 2).
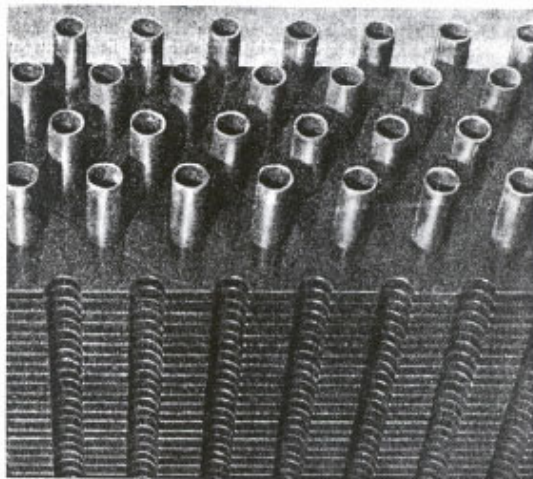
Figure 1. Parallel plate reactor.

The basic reactor designs were considered by Storch to be well defined by 1950. These were described by Kölbel as shown in figure 3 [1]. The parallel plate reactor, normally used for atmospheric pressure synthesis with the cobalt catalyst in Germany, is represented by a in figure 3. Usually fins were attached to the reactor tubes to facilitate the transfer of heat from the catalyst bed to the coolant. The arrangement of the double walled reactor (figure 2) is shown in b, figure 3. Many simple tubes filled with catalyst could be arranged in a shell (tube in shell) reactor system; a version of this type of reactor was and is still utilized by Sasol (Arge reactor) (c, figure 3).

Late 1940-early 1950 was a period of very active research and development for FTS and a variety of reactors were utilized. The circulating fluid bed reactor system had been developed during WWII by Standard Oil (NJ) for catalytic cracking (FCC process). It performed so successfully that it quickly became the dominant reactor
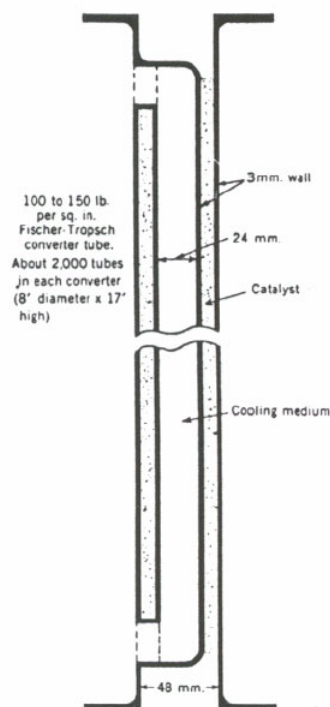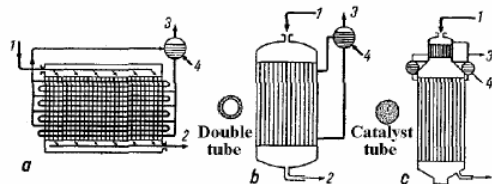

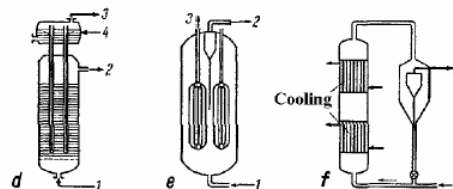**Figure 2. Section of Middle-Pressure Ruhrchemie Synthine reactor tube.**

Figure 3. Reactor types (a, parallel plate, Ruhrchemie 1936; b, double tube, Ruhrchemie 1938; c, Arge tube, Ruhrchemie-Lurgi 1952; d, liquid phase, Rheinpreussen 1943; e, fixed fluid bed, Hydrocol 1948; f, circulating fluid bed, Kellogg 1958; 1, synthesis gas (gas entry and flow pater); 2, unconverted gas and products; 3, cooling vapor; 4, coolant drum).

type for catalytic cracking. Several organizations worked to develop versions of this reactor for FTS. The group headed by HRI developed the fixed fluid bed reactor for their commercial plant located in Brownsville, TX (e, figure 3). The adequate supply and low price of oil from the Middle East caused the plant to be closed just as the operating problems were being solved. Among the major problems was the degradation of the catalyst which created separation problems as well as rapid loss of catalyst from the reactor zone. The Kellogg Company

was a leader in developing a circulating fluid bed reactor for FTS and this is the version adapted by Sasol for their high temperature FTS plants (f, figure 3). In spite of many operating problems that led to Kellogg abandoning the development to Sasol, the problems were overcome and Sasol eventually operated 16 of these reactors at Secunda (producing more than 100,000 b/d) and additional smaller ones at Sasolburg. Recently all of the 16 reactors at Secunda were replaced by 8 fixed fluid bed reactors [2].

During and following WWII, Kölbel and coworkers worked on the development of a slurry phase reactor (d, figure 3). Following WWII a pilot plant was operated with an iron catalyst under conditions selected to produce gasoline range products as the dominant liquid product [3]. This plant utilized a reasonably simple design for the reactor (figure 4). While Kölbel and coworkers developed much understanding of the scientific and engineering principles for the operation of the slurry bubble column reactor, much of which is summarized in a recent book [4], the mass balance during operation of the pilot plant was not adequate or they utilized a catalyst with a selectivity that has not been duplicated since then during 50 years of work by many groups (figure 5). During and for about 10 years following WW II, the US Bureau of Mines operated a 50-70 bbl/day slurry reactor pilot plant at Louisiana, Missouri (flow diagram, figure 6; reactor schematic, figure 7). Because they used fused iron or precipitated catalysts sintered at high temperatures to provide attrition resistance, the catalyst particle density was such that catalyst dispersion was affected by both gas and liquid flow. Operation of the Bureau of Mines pilot plant was terminated after only four runs had been made but laboratory scale work has continued, with some interruptions, since that time. In the early 1990s, Sasol completed development of their slurry bubble column reactor and brought on-stream a 2,500 bbl/d, 5 meter diameter reactor and this has operated without problems for more than 10 years. For the commercial plant in Qatar, 11 meter diameter reactors will be utilized with a cobalt based catalyst.
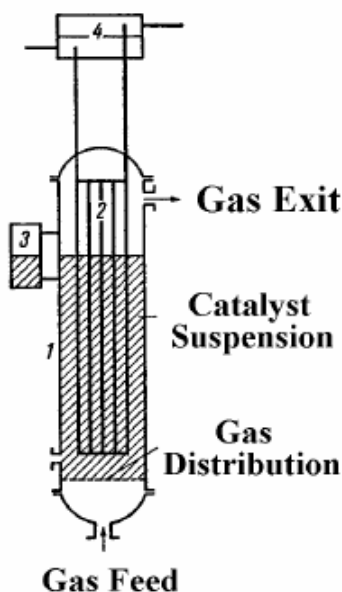
Figure 5. Reactor-wax yield vs. methane yield.

Figure 6. Typical flow diagram of U.S. Bureau of Mines oilcirculation **process.**

Figure 4. Reactor for synthesis in liquid phase (Rheinpreussen-Koppers) (1, cylindrical reactor; 2, cooling tubes; 3, liquid level regulator; 4, vapor-liquid chamber).
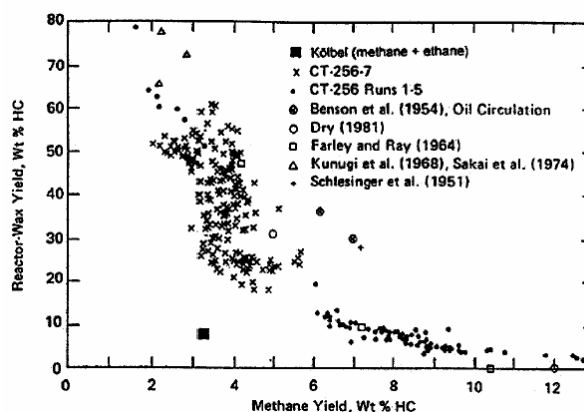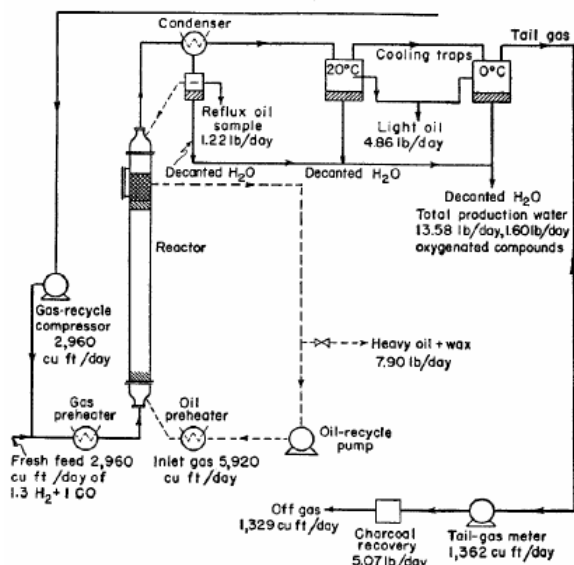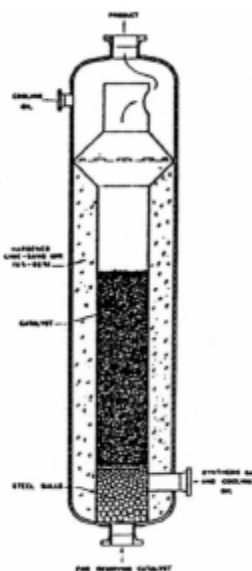
Figure 7. Slurry reactor used by U.S. Bureau of Mines.

In both Germany and the US, attempts were made to utilize a high recycle of unconverted gas (up to about 100:1 recycle:feed) to maintain temperature control in the reactor. A schematic of a multilayer reactor that utilizes cooling coils between the catalyst bed layers is illustrated in figure 8. Multilayer reactors were also used in other process schemes where the catalyst would be cooled by adding a spray of oil at the top of the reactor so that evaporation could remove much of the heat of reaction or the beds could be completely immersed in liquid or foam.
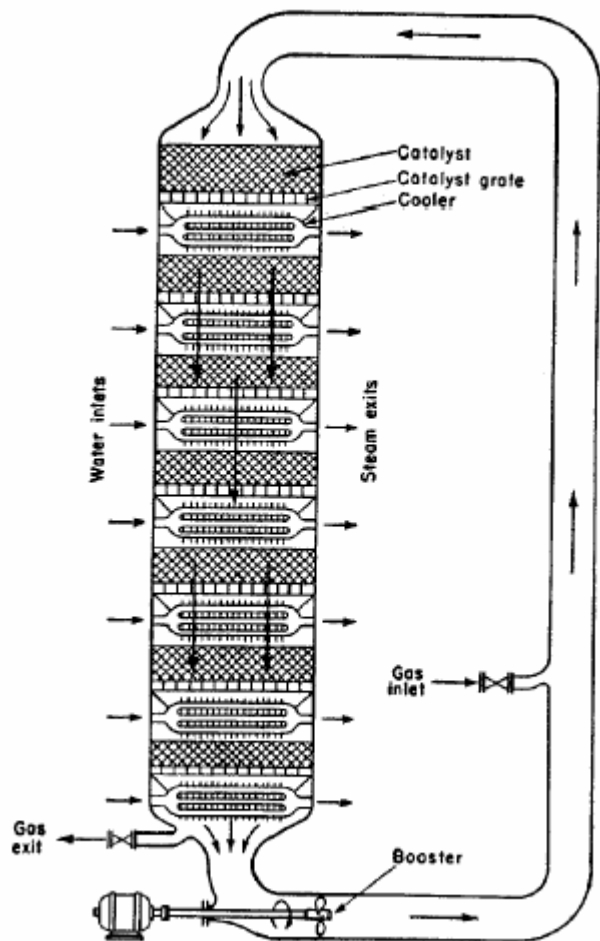
Figure 8. Multilayer converter for gas recycle, 20 atm.

For nearly 75 years, the "art" of reactor development has outpaced the "science and engineering understanding." For example, a translation of "The evaluation of converters for exothermic and endothermic catalytic reactions occurring within narrow temperature limits" was written during 1942 by a worker for I.G. Farbenindustrie A.G. at Leuna, where a major FTS commercial plant was operated[5]. The paper was translated because of interest in the US about design methods used in Germany. The translators considered that the methods were extreme simplifications of the actual physical problems and that their actual description of the phenomena that really occur were questionable. Two examples were cited: (1) the assumption that the heat generated per unit volume of catalyst is constant throughout the reactor could not represent the actual case and (2) the assumption that all of the heat generated was carried away by conduction through the catalyst bed in a direction transverse to the main gas flow to leave the reactor at the same temperature as it enters the reactor ignored the heat

carried out of the reactor by the products. This provides an example of the difficulties modelers had during the pre-computer age. During the past 50 years exceptional advances have been made in reactor engineering and attention has been directed toward modeling bubble column reactors, driven in part by the potential application of these in large 30-50,000 bbl/day plants. Thus, instead of the simple concept of a reasonably uniform reactor volume, it is now recognized that the flows and the material distributions are very complex, as illustrated in the schematic in figures 9 and 10. Extensive modeling and/or experimental works are being conducted by many groups located in many countries. An example of the extent and complexity of the efforts is illustrated in the program at Washington University (located in the US) that is funded by government and industrial organizations (figure 11).

To predict the type of the next generation of reactors is fraught with danger. Today there is extensive interst in micro and this applies to reactors. Chemical companies are considering a variety of microchannel reactors with the intent of replacing one large reactor with many, many smaller reactors that provide improved control of important operating conditions. Others are looking at the adaptation monolith reactor technology that has been so successfully applied to auto catalysis to the more complex situation encountered in FTS.
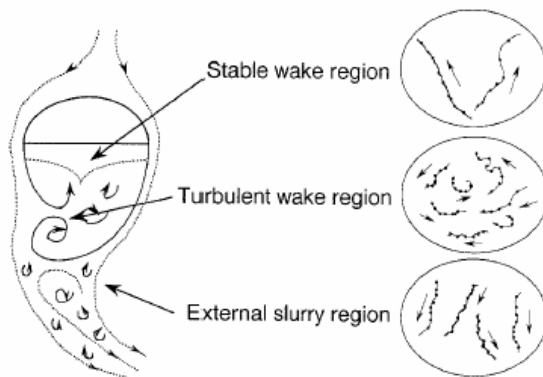

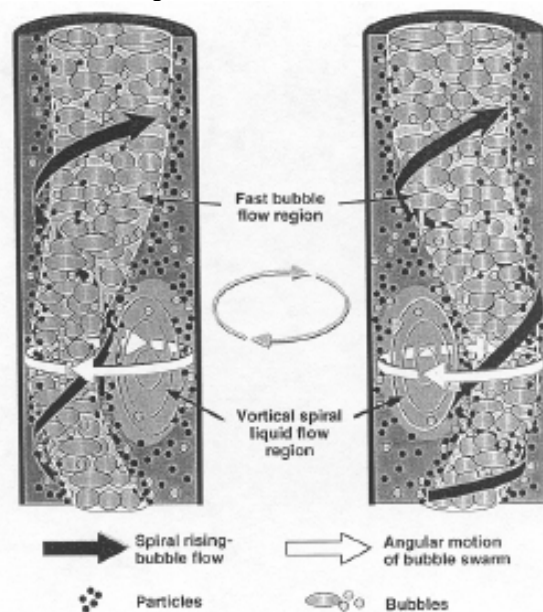**Figure 9.** Typical particle trajectories within three different flow regions around a rising bubble.

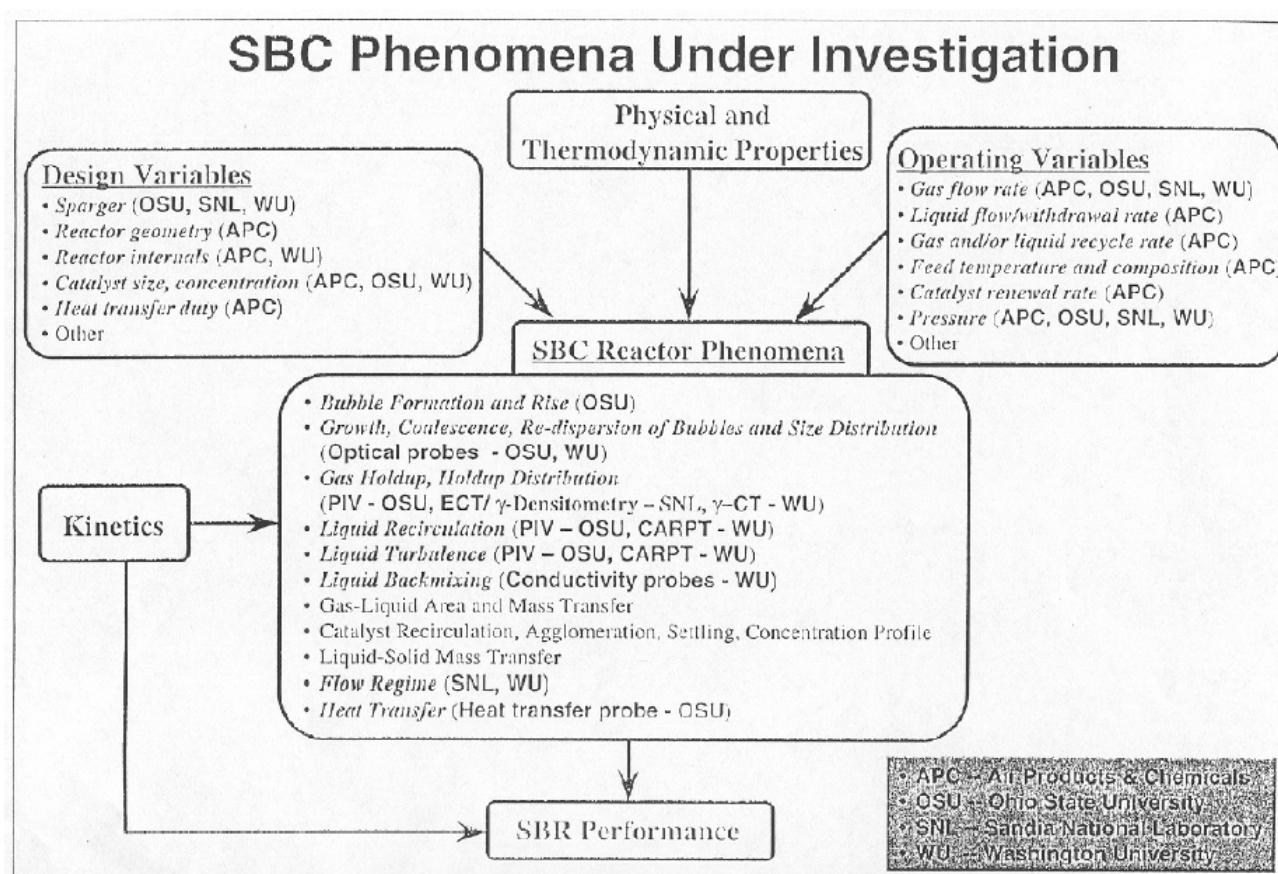**Figure 10.** Model of flow scheme in the slurry bubble column.

Figure 11. SBC phenomena under investigation.

While the reactor development has been slow, the changes in FT process developers have been very rapid. A comparison over a four year period (1999 vs. 2003) shows many changes with mergers and dropouts dominating the scene. This means that the "ownership" of reactor technology will become even less-well defined.

References
1. H. Kölbel in Chimie Organique,(K. Winnacker and L. Küchler, Eds), Part 3, Editions Eyrolles, Paris, 1966, pp 627-740.
2. Jager, B., M. E. Dry, T. Shingles and A. P. Steynberg; Experience with a new type of reactor for Fischer-Tropsch synthesis; Catal. Lettr., 7, 293-302 (1990).
3. Kolbel, Herbert; M. Ralek; The FT synthesis in the liquid phase; Catal.Rev. Sci.Eng. 21 (l980) 225.
4. Deckwer, W.-D.; Bubble Column Reactors; Wiley, 1985.
5. "The evaluation of converters for exothermic and endothermic catalytic reactions occurring within narrow temperature limits," G. Wirth (R.C. Grass and H.J. Kandiner, translators, U.S. Bureau of Mines Information Circular 7587, Nov., 1950.

ConocoPhillips GTL Technology: The COPox™ Process as the SynGas Generator

H. A. Wright, J. D. Allison, D. S. Jack, G. H. Lewis; S. R. Landis

Ponca City Technology Center, ConocoPhillips, PO Box 1267, Ponca City, OK 74602

Abstract

This paper discusses the development of ConocoPhillips GTL technology specially the development of our proprietary COPox™ SynGas technology. This paper discusses what the COPox™ process is; how ConocoPhillips has developed the technology; and where ConocoPhillips is in the development of the technology. This paper will also discuss general syngas chemistry and where the COPox™ process fits into the spectrum of syngas technologies. A comparison with the leading SynGas technology shows that for an integrated GTL plant, COPox™ technology can improve the overall carbon efficiency of the GTL plant.

Introduction

ConocoPhillips has developed proprietary Gas-to-Liquids (GTL) technology to use to convert stranded natural gas to easily transportable fuels. This Gas-to-Liquids technology actually consists of at least three separate technologies that are integrated together to produce a highly efficient GTL process.

1. ConocoPhillips has developed a syngas process, catalyst, and reactor system for syngas generation called the COPox™ process.
2. ConocoPhillips has also developed a proprietary Fischer-Tropsch catalyst and reactor.
3. ConocoPhillips has also developed a proprietary Product Upgrading technology to convert the long chain hydrocarbons to useful fuel range materials.
4. ConocoPhillips has integrated these processes to enable high carbon efficiency; which results in a lower gas consumption per barrel of product produced.

What is the COPox™ Process

This paper concentrates on the COPox™ technology at ConocoPhillips. The COPox™ process is a synthesis gas generation technology. It is based on the catalytic partial oxidation of natural gas:

$$CH_4 + \tfrac{1}{2} O_2 \rightarrow 2 H_2 + CO$$
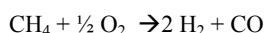
This reaction is exothermic and with preheat can be run autothermally so that no additional external heat source is needed to aid in the generation of synthesis gas. We have found that successful catalytic partial oxidation should be operated with millisecond contact times with Gas Hourly Space Velocities around 500,000 hr^{-1}. The high space velocity of the COPox™ process relative to other systems means that the reactor volumes are considerably smaller leading to lower reactor and catalyst costs.

We started the development of ConocoPhillips GTL technology in 1997. We initially started working on Fischer Tropsch technology but quickly realized that if we were to get a breakthrough in this overall area we would have to tackle the syngas generation costs as well. Some studies were showing that upwards of 60% of the cost of a GTL plant could be in the syngas and related areas of the plant.[1] It was clear, that even a breakthrough in Fischer Tropsch would not make GTL economically viable without more.

In 1998, we started the development of the COPox™ process after a process economics review indicated that it could result in a lower cost, more efficient GTL process than other available technologies.

Since 1998, we have initiated a technology program for the COPox™ process as part of an overall GTL effort. Over 40 full time individuals work in the continuing development of COPox™ technology. This includes work in all areas of the technology commercialization including catalyst development, reactor process and mechanical design, reactor modeling including computational fluid dynamics; and process design engineering for scale up of our technology to the demonstration scale. Another 60 individuals work in the operations and maintenance of our new 400 BPD Demonstration Plant.

We currently have reactors of many different sizes in operation in Ponca City, OK. We learned early on in the development of the COPox™ technology, that most experiments needed to be done in high-pressure pilot reactors instead of the quartz atmospheric reactors often used in academia. We have two demonstration scale reactors that will be started up this summer that are each capable of processing enough natural gas to produce 400 BPD of liquid product out the back end of the plant. Table 1 shows the number and type of COPox™ reactors in operation in Ponca City.

Table 1. COPox™ High Pressure Reactors in Operation in Ponca City

Reactor Type	Number	FT Liquid Production
Demonstration Scale	2	400 BPD
Pilot Scale	2	>2 BPD
Catalyst Testing Scale	12	0.2 – 0.5 BPD

SynGas Chemistry

In addition to the partial oxidation reaction already mentioned, there are several other reactions that need to be accounted for in understanding the various means for syngas generation. The first is the steam methane reforming reaction $CH_4 + H_2O \rightarrow 3H_2 + CO$. The next is full combustion: $CH_4 + 2 O_2 \rightarrow 2 H_2O + CO_2$. The last key reaction is the water gas shift reaction $CO + H_2O \rightarrow CO_2 + H_2$

The combination of these reactions can aid in our understanding of why ConocoPhillips COPox™ technology can result in a very highly efficient GTL process. Each of the other syngas technologies use these reactions and approach thermodynamic equilibrium. Let's compare several possible syngas generators to COPox™ process for GTL plants.

1. Steam Methane Reformer (SMR)
2. Autothermal Reformer (ATR)
3. COPox™ Process
4. Non-Catalytic POX reactor (POX)

An important understanding of a natural gas feed, Cobalt FT catalyst based GTL Process is that H2 is consumed with CO in an overall ratio of 2.0 to 2.2. The closer this ratio is achieved in the syngas manufacturing step coupled with maximizing CO production, the more efficient the GTL Process will be.

There are several competitor syngas technologies used in a GTL process. Some potentially use a SMR to generate syngas. This uses the steam methane reforming reaction to make syngas with a H2/CO ratio of about 3.

An ATR makes syngas from the combustion, reforming, and water gas shift reaction. Oxygen is fed to the reactor so that the

system is autothermal. The H2/CO ratio of the syngas is dependent upon the steam to carbon ratio. Typically the steam to carbon ratio ranges from 0.6 to 1.0 or even more. This S/C ratio results in a syngas with a H2/CO ratio of 2.3 –2.5 or so. As the amount of steam declines the H2/CO ratio of the product syngas moves closer to the desired 2.0.

The COPox™ process will result in a syngas slightly below 2.0 in practice. The higher-pressure operation reduces the ratio from the ideal H2/CO ratio of 2 [2].

A non-catalytic POX reactor will result in a syngas H2/CO ratio in the 1.7-1.8 range. Figure 1 shows the H2/CO ratios of syngas produced by these various means.
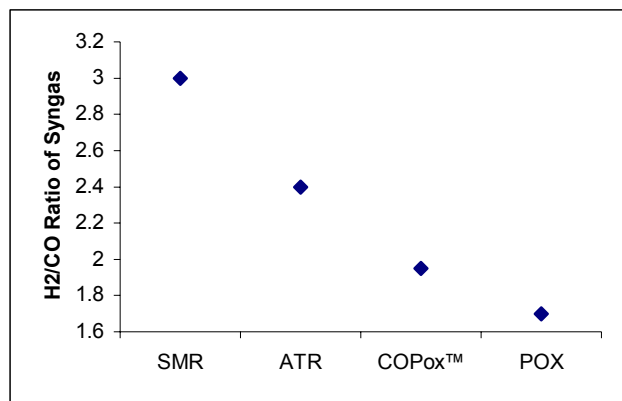

Figure 1. The Hydrogen to CO ratio of the syngas from various syngas generators determines the ultimate efficiency of the GTL process.

Clearly the farther from the Fischer Tropsch ideal ratio slightly greater than 2, then the more inefficient the overall GTL process probably is.

Another way to look at syngas generators is to look at the CO yield of the various means of producing syngas. If you pay for carbon from some natural gas source, it is clear that you want as much of it as possible to end up as CO not carbon dioxide. Figure 2 shows the single pass CO yield of the COPox™ process versus an ATR with a S/C (steam to carbon) ratio of 1.0 and 1.5 (assuming no CO2 or heavy hydrocarbon recycling). You can now see why there will be a continuing drive to lower the steam to carbon ratios in ATR's even further.
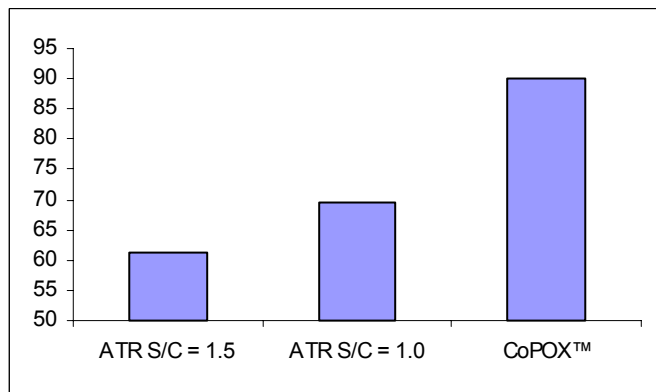

Figure 2. Carbon Monoxide yields for several ATR cases versus a COPox™ process. Assumes no recycle.

Conclusions

In conclusion, the COPox™ process provides the means to have a high efficiency and lower cost GTL facility. ConocoPhillips has spent the last 5 years developing the technology through the demonstration scale.   The Demonstration Plant is in the commissioning stage and includes 2 reactors capable of producing syngas for a 400 BPD Fischer Tropsch plant.

References:
(1) Choi, G.; Kramer, S.; Tam, S.; and Fox, J; Prepr. Pap. - *Am. Chem. Soc., Div. Fuel Chem.*, **1997**, *42* (2), 667-671.
(2) Allison, J. D.; Swinney L. D.; Niu, T; Ricketson, K; Wang, D; Ramani, S.; Straguzzi, G. I.; Minahan, D. M.; Wright, H. A.; Hu, B.; U.S. Patent Application 20020115730; 2002.

Plasma Spray Coatings for Designing Next-Generation Supported Metal Catalysts for Methane Conversion into Clean Fuels

A. Kulkarni and H. Herman

Dept. of Materials Science & Engineering
Center for Thermal Spray Research
State University of New York
Stony Brook, NY 11794

Introduction

The commercial pathway to clean fuel production from methane requires an initial conversion into a mixture of synthesis gas, a mixture of carbon monoxide and hydrogen. This initial step results in more than two-thirds of the total process cost and is a target of extensive research. Ceramic systems such as membranes could play a critical role in synthesis gas production as well as hydrogen separation technologies. Plasma spray methods, in which powder particles are melt-sprayed onto a substrate, where they form a thick film, leaving an integral structure with pores, is a viable approach to fabricating membranes. Through-pores in the range from nano-sized to sub-micron are readily obtainable within such deposited microstructures.   These pore systems can be employed for gas separation, operating at temperatures from ambient through over 2000°C, e.g., using zirconia-based ceramics.

Experimental

Plasma spray is relatively straightforward in concept but rather complex in function. The plasma torch operates on direct current, which sustains a stable, non-transferred electric arc between a tungsten cathode and a annular water-cooled copper anode. A plasma forming gas (generally, argon or other inert gas, complemented by a few percent of an enthalpy enhancing gas, such as hydrogen) is introduced within the torch interior, the gas becoming ionized, and on exiting the anode nozzle, ionic-electron recombination occurs, relealsing consider enthalpy which is sufficient to melt and accelerate refractory ceramics to sonic velocities. The effective temperature of the plasma is in excess of 15,000K for a typical dc torch operating at 40 kW. The powder particles, approximately 40 micrometers in diameter, are accelerated and melted in the flame on their high-speed (100-300 M/sec) path to the substrate, where they impact and undergo rapid solidification.

Plasma spray is used to form deposits of greater than 10 micrometers of a wide range of industrial materials, including nickel and ferrous alloys, refractory ceramics, such as aluminum oxide and zirconia-based ceramics.
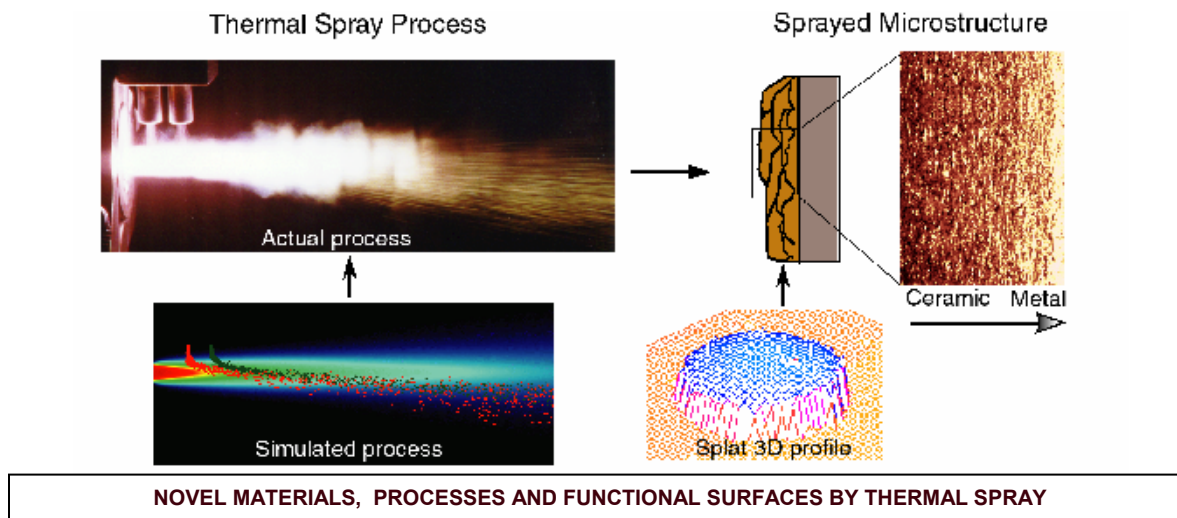
Plasma spray technology has great potential in natural gas-related programs. It is clear that thermal spray can play a special role in the production of ceramic membranes for gas separation processes. In fact, thermal spray has been used for a number of years in the production of both electrodes and interconnects in solid oxide fuel cell (SOFC) manufacture. The NSF-supported Center for Thermal Spray Research, at SUNY-Stony Brook, has pioneered in the processing of controlled-porosity permeable ceramics. Part and parcel of this activity has been the capability to characterize the pore structure using a suite of experimental techniques: Mercury Porosymmetry, and working with NIST, Small-Angle Neutron Scattering (SANS) and X-Ray Computed Microtomography (XCMT).

Results and Discussion

XCMT studies have been carried out at the Advanced Photon Source/Argonne National Laboratory (APS/ANL) and the National Synchrotron Light Source/Brookhaven National Laboratory (NSLS/BNL) to characterize/visualize microstructure of thermal sprayed ceramic coatings (e.g., alumina, zirconia-based ceramics). Experiments focus on quantitative characterization of porosity and its variation with thickness. Through such studies, we wish to further our understanding on the influence of thermal exposure on relative changes in microstructural features in these coatings.

Experiments are being directed at SOFC and porous membranes. It is necessary to characterize multi-layered films of these functional energy-related functional coatings. This allows for characterization of a complete SOFC stack consisting of an interconnect, a cathode, an electrolyte and an anode. The system in case is porous nickel/YSZ cermet anode, a YSZ electrolyte and a porous (La,Sr)MnO3 cathode. While porosity plays a crucial role in operation of these SOFCs, the high operating temperatures (800° – 1000°C) of these structures cause microstructural changes and, thus, degradation of properties. Hence, maintenance of the porous structure is important.

Thermal Spray Process
Actual process
Simulated process

Sprayed Microstructure
Ceramic   Metal
Splat 3D profile

NOVEL MATERIALS, PROCESSES AND FUNCTIONAL SURFACES BY THERMAL SPRAY

PLASMA CO₂ REFORMING OF METHANE VIA CORONA DISCHARGES

Changjun Liu, Genhui Xu

State Key Laboratory of C1 Chemistry and Technology,
School of Chemical Engineering, Tianjin University,
Tianjin 300072, China

Introduction

A lot of attentions have been recently paid to the CO_2 reforming of methane to syngas. A major reason for it is that this reaction can provide us a syngas with a 1/1 ratio of H_2 and CO, which is typically suitable for the synthesis of valuable oxygenated chemicals.[1] Among the catalysts developed, Al_2O_3 supported Ni catalysts were extensively investigated due to their relatively high activity and low cost. The major problem for the further practical application of these nickel catalysts is the deactivation of the catalyst, suffered from carbon deposition on the catalyst during reactions. Many investigators are working on the improvement in this nickel catalyst by using the addition of promoters,[2, 3] using novel reactor configurations,[4] and using different supports.[3] In this work, we attempt to use an AC corona discharge plasma for the CO_2 reforming of methane to syngas. A stable operation of plasma CO_2 reforming of methane has been achieved.

Experimental

The corona discharge dry reforming was carried out in a quartz tube reactor with an I.D. of 6.0 mm and a length of 0.6 m. The reactor system has been described previously.[5] The corona discharge reactor consists of two electrodes, a top metal wire electrode and a lower hollow electrode as the grounded one. The volume between these two stainless steel electrodes is 340 mm³. The feed gases, CO_2, CH_4 and the dilution gas, helium, are introduced into the reactor via flow meters. The feed gas flow enters the upstream wire electrode and exits at the downstream grounded one. The gas discharge is generated between these two electrodes by an AC generator. The AC electric field operates at a frequency of 60 Hz. The AC voltage provides us with an easy way to generate the streamer corona discharge, which takes place only when the voltage reaches a sufficiently high level during each half cycle. In the discharge volume, the interaction between accelerated charged particles (i.e., electrons and ions) and other chemical species (i.e., molecules and radicals) takes place. The feed and effluent product gases are analyzed by an on line gas chromatograph with a TCD detector.

Results and Discussion

Figure 1 shows an effect of input voltage on discharge reactions with a constant CO_2/CH_4 ratio of 4:1. The conversions of CH_4 and CO_2 increase with the increasing input voltage at the beginning. The formation rates of products, syngas and a small amount of C_2 hydrocarbons, also increase with this increasing input voltage. The methane conversion increases slightly with the increasing input voltage after the input voltage reaches 5 kV, but the formation of syngas increases quickly with the increasing input voltage.

Figure 2 presents an effect of residence time on the plasma dry reforming. Evidently, the low residence time (high flow rate) is favored for the production of syngas (C_2 hydrocarbons too). This suggests that the plasma dry reforming is a quickly reaction.
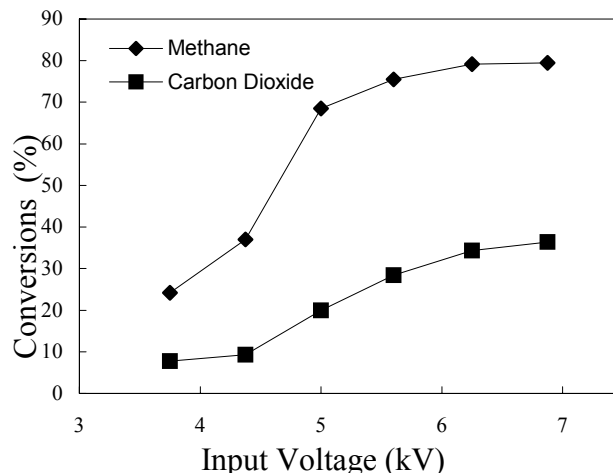

Figure 1. Effect of input voltage (gas composition: CH_4 — 5%, CO_2 — 20%, He — 75%; total gas feed: 100 cm³/s; ac electric field frequency: 60Hz).
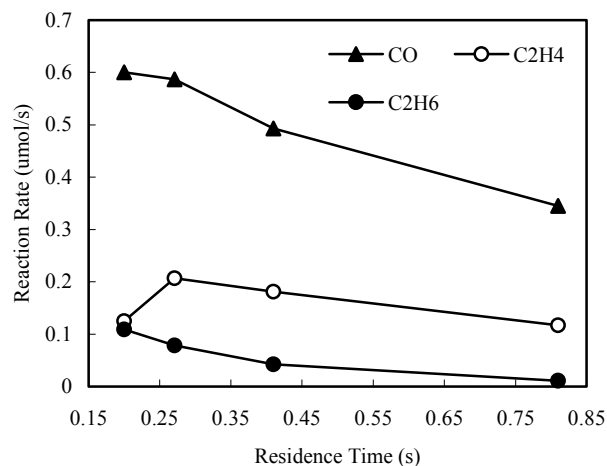

Figure 2. Effect of residence time (gas composition: CH_4 — 5%, CO_2 — 20%, He — 75%; total gas feed: 100 cm³/s; ac electric field frequency: 60Hz).

The present investigation confirms the plasma dry reforming of methane using a simple corona reactor is effective. The major advantage of this plasma dry reforming is its high stability. The ratio of hydrogen and carbon monoxide of syngas produced is based on the feed ratio of methane and carbon dioxide. The input voltage (or the input power) and the residence time (or the feed flowrate) have also a significant effect. Further investigation is being conducted.

References

1. Lunsford J.H., *Cata. Today*, **2000**, 63, 165-174.
2. Lemonidou A. and Vasalos I.A., *Appl. Catal. A*, **2002**, 228, 227-235.
3. Chang J.-S., Park S.E, Yoo Y.W., and Park J.-N., *J. Catal.*, **2000**, 195, 1-11.
4. Wang L., Murata K., and Inaba M., *ACS Symp. Series*, 852, 57-68.
5. Liu C.-J. (1996) Oxidative synthesis of higher hydrocarbons from CO_2 and CH_4 by streamer discharges. ***Chem. Lett.***, 749.

Alkane CH Activation and Catalysis by O-Donor Ligated Ir Complexes

Antek G. Wong-Foy, Gaurav Bhalla, Xiang Y. Liu, Roy A. Periana*

Department of Chemistry
Loker Hydrocarbon Institute
University of Southern California

Highly efficient and selective transition metal mediated methods for the functionalization of alkanes is still largely an unsolved problem that poses significant challenges to both homogeneous and heterogeneous chemists alike. One of the key reasons for this is that the C-H bonds of saturated alkanes are thermodynamically and kinetically difficult to break. However, significant advances have been made in our understanding of how C-H bonds are broken and formed by the use of well defined, homogeneous organometallic complexes.[1] These complexes generally contain either high oxidation state early transition metals or low oxidation state late transition metals. The ligands used in these systems range from C-donor, *e.g.* cyclopentadenty ligands, to mono and multi-dentate P- or N-donor ligands, to chelating NC or PC type ligands. O-donor ligands have been used to a much smaller extent with early transition metals and to our knowledge, for late transition metals, this is absent altogether.
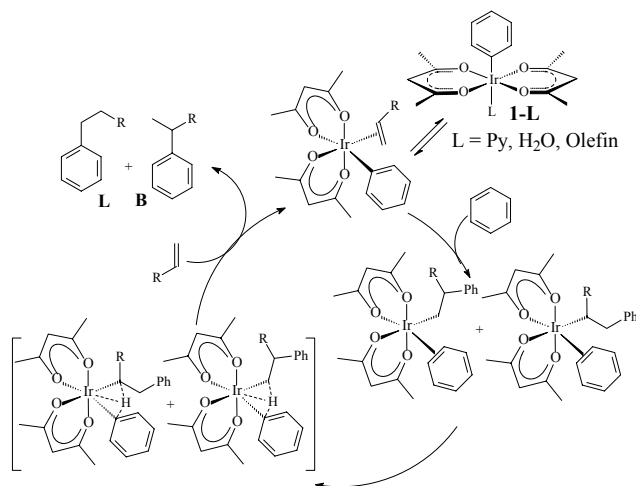

Figure 1. Proposed CH Activation Reaction Mechanism for Hydro-Arylation of Olefins by a bis-acac,O,O-Ir(III) Species.

Recently, we demonstrated that the O-donor Ir(III) complex, bis-acac-O,O-Ir(III)(Ph)(L), **1-L**, catalyzes the hydroarylation of unactivated olefins with unactivated arenes to generate alkyl benzenes with a preference for the anti-Markovnikov product.[2] Other studies have shown that related bis-acac Ir(III) complexes can also isomerize terminal alkenes to mixtures of internal ones.[2c]

Herein we report that bis-acac-O,O-Ir(III)(CH₃) complexes where the phenyl group in **1** is replaced with a methyl group react with alkanes by CH activation to generate the corresponding alkyl-Ir complexes under mild conditions. The synthesis of dinuclear Ir complex, [Ir(μ-acac-O,O,C³)(acac-O,O)Me]₂, **2**, that was used in these studies was prepared as show in Scheme 1. As shown, there is a facile
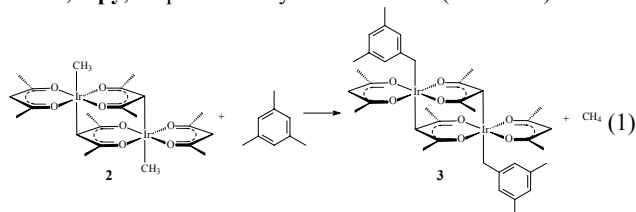
equilibrium between the mono-nuclear Ir complex, **2-solv**, and the dinuclear complex, **2** on dissolution in CH₂Cl₂.

Scheme 1. Synthesis of (acac)₂Ir(CH₃) Complexes
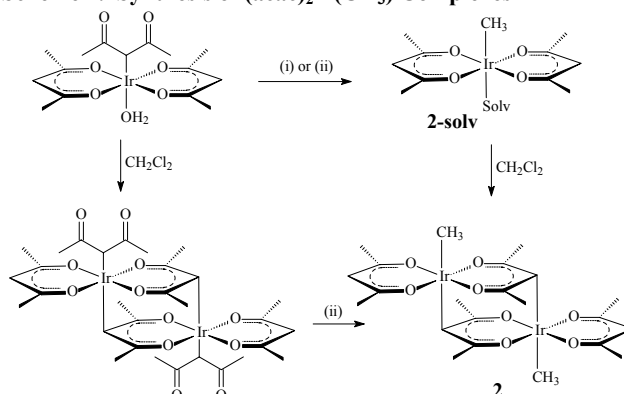
Conditions: (i) excess HgMe₂, MeOH/acetone, 60°C; (ii) 1.1 ZnMe₂, THF/toluene, 90°C

Heating a yellow suspension of **2** (**2-solv** can also be utilized but is less soluble) in mesitylene at 130 °C for 3h results in the formation of a clear yellow solution. ¹H and ¹³C NMR analysis of the crude mixture in CDCl₃ shows clean formation of the dinuclear complexe, bis-acac-O,O-Ir(III) mesityl, **3** (Eq 1). Only benzylic CH activation is observed; no activation is observed at the aromatic positions. If the reaction is run in a sealed NMR tube with mesitylene-*d₁₂*, only mono-deuterated methane is observed to form in the methane region. Heating **2** with cyclohexane as solvent yielded a crude solution of the corresponding dinuclear cyclohexyl complex, **4**. Treatment of this solution with excess pyridine afforded the mononuclear pyridine adduct, **4-py**, in quantitative yield based on **2** (Scheme 2).

Some of the other substrates that react with **2** are shown in Table 1. As the facile equilibrium between mononuclear and dinuclear complexes in these systems can complicate analysis, the products of the reaction were dissolved in CD₃CN in order to ensure that only the mono-nuclear complexes were observed in solution.

These reactions unambiguously show that complexes based on the O-donor (acac)₂Ir(III) motif can activate alkane CH bonds. To our knowledge, this is first late-metal O-donor complex that shows this reactivity. Many systems show CH activation today. However, relatively fewer show catalysis with alkanes.[3,4,5,6,7,8,9] We are particularly interested in developing catalysis based on the CH activation reaction and it important to determine if the systems we are developing are sufficiently stable and selective to allow catalysis with alkanes. It is generally considered that O-donor ligands are kinetically labile, presumably due to the availability of a lone pair that is not present in P- or N-donor ligands. However, we find that complexes based on (acac)₂Ir(III) can be quite stable. For example, **1** can be refluxed in benzene or acetic acid for days without any signs

of decomposition. In acetic acid **1** is converted to the acetate analog. Another key key reason for examining the use of O-donor ligands with late metals for CH activation is that we anticipated that metal complexes based on O-donor ligands could be sterically and electronically different from those based on C, N or P-donor ligands. Specifically, given the higher electronegativity and "hardness" of O, it seemed likely that metal complexes would be less electron rich and if CH activation could be maintained could be more suited to oxidation catalysis. While this reduction in electron density might be expected to disfavor reaction such as oxidative addition, it could be expected that O-donor complexes could favor the oxidative functionalization reactions that are required in oxidation catalysis by facilitating conversion of M-R intermediates to functionalized RX products.

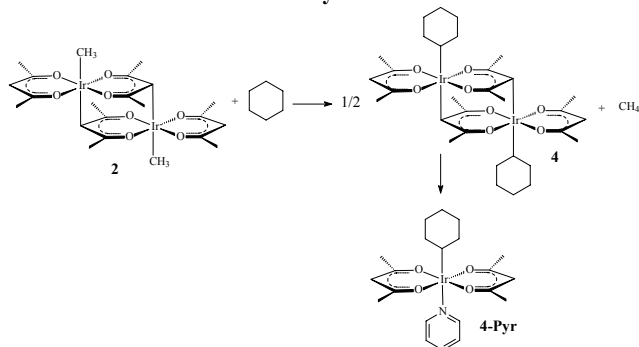**Scheme II. CH Activation of Cyclohexane**

Table 1. C-H activation Products from Reaction of 2.

| Entry	Substrate	Temp (°C)	Time	Product (major)
1		120	3 h	
2		130	3 h	
3		80	17 h	
4		100	1 h	

Indeed, consistent with the poorer electron-rich characteristics of O-donor complexes, we find that **1** will not bind olefin or CO except at high pressures. This is an important observations and most likely accounts for the efficient hydroarylation activity of **1**; more electron rich complexes would be expected to bind olefins more tightly and be inhibited.

To begin to explore alkane catalysis based on the CH activation reaction with O-donor ligated complexes, we examined the use of **2** to catalyze the H/D exchange between benzene-d_6 and various alkane substrates. Thus, an equimolar solution of benzene and cyclohexane was heated to160C with **1**. Analysis by GC/MS and NMR show that H/D exchange between C_6D_6 and RH cleanly occurs without any evidence of catalyst decomposition, except conversion of **2** in the

phenyl analog, **1**. A likely catalytic cycle for this reaction is shown in Scheme II.

Preliminary experiments show that CH_4 exchanges with C_6D_6, Mesity-D_{12} or CD_3CO_2D solvents at ~160°C. These results show that the (acac)$_2$Ir(III) motif is capable of catalysis with alkanes, including methane. The next step of research will be to explore the use of **2** to catalyze oxidation reactions, for example the conversion of methane to methyl products such as methanol or methyl acetate.

Scheme III. Proposed Mechanism for H/D Exchange
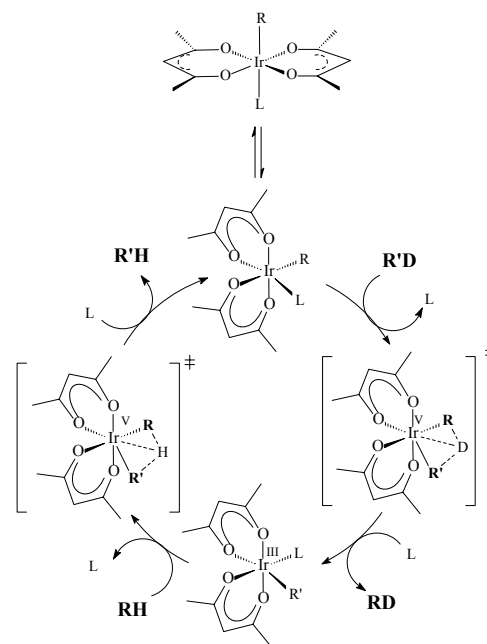
[1] (a) Jia, C.G.; Kitamura, T.; Fujiwara, Y. *Acc of Chem Res* **2001**, *34* 633. (b) "Isotope Effects in C-H Bond Activation Reactions by Transition Metals." Jones, W. D. *Accounts of Chemical Research* **2003**, *36*, 140-146

[2] (a) Periana, R. A.; Liu, X. Y.; Bhalla, G. *Chemical Communications* **2002**, 3000-3001. (b) Matsumoto, T.; Periana, R. A.; Taube, D. J.; Yoshida, H. *Journal of Molecular Catalysis a-Chemical* **2002**, *180*, 1-18. (c) Matsumoto, T.; Periana, R. A.; Taube, D. J.; Yoshida, H. *Journal of Catalysis* **2002**, *206*, 272-280. (d) Matsumoto, T.; Taube, D. J.; Periana, R. A.; Taube, H.; Yoshida, H. *Journal of the American Chemical Society* **2000**, *122*, 7414-7415

[3] (a) Chen. H. Y.; Schlecht, S.; Semple, T.C.; Hartwig, J. F. *Science*, **2000**, *287*, 1995.

[4] Periana, R. A.; Taube, D. J.; Gamble, S.; Taube, H.; Satoh, T.; Fuji, H. *Science*, **1998**, *280*, 560.

[5] (a) Kanzelberger, M; Singh, B; Czerw, M; Krogh-Jespersen, K; Goldman, A. S. *J. Am. Chem. Soc.* **2000**, *122*,11017

[6] (a) Lin, M; Shen, C; Garcia-Zayas, E. A.; Sen, A. *J. Am. Chem. Soc.* **2001**, *123*, 1000.

[7] Burk, M. J.; Crabtree, R. H. *J. Am. Chem. Soc.* **1987**, *109*, 8025

[8] (a) *Activation of Saturated Hydrocarbons by Transition Metals*, Shilov, A. E. Reidel: Dorrecht, 1984 and references therein

[9] Sakakura, T.; Sodeyama, T.; Sasaki, K.; Wada, K.; Tanaka, M. *J. Am. Chem. Soc.* **1990**, *112*, 7221.

CATALYTIC PARTIAL OXIDATION OF METHANE TO METHANOL AND FORMALDEHYDE

Ayusman Sen and *Minren Lin*

Department of Chemistry
The Pennsylvania State University,
University Park, Pennsylvania 16802, U. S. A.
E-mail: asen@chem.psu.edu

Introduction

Methane is the least reactive and the most abundant member of the hydrocarbon family. Ethane comes second in both categories. Together, their known reserves approach that of petroleum [1]. Thus, the selective oxidative functionalization of these alkanes to more useful chemical products is of great practical interest [2-7]. The current technology for the conversion of alkanes to oxygenates involves *multi-step* processes. Clearly, the *direct* partial oxidation of the lower alkanes to oxygenates would be far more attractive from an economic standpoint. Of particular interest would be the formation of the *same* end product from different starting alkanes, thus obviating the need to separate the alkanes. For example, natural gas is principally methane with 5-10% ethane. A system that converts both to the same C_1 product, would not require the prior separation of the alkanes. We will discuss two catalytic systems for the direct partial oxidation of methane by dioxygen.

Results and Discussion

The first system involves the catalytic oxidation of methane to methanol by dioxygen in a mixture of water and trifluoroacetic acid [8,9]. A combination of metallic palladium and copper chloride acts as the catalyst and either carbon monoxide or dihydrogen is required as a coreductant. Studies indicate that the overall transformation encompasses three catalytic steps in tandem (Scheme 1). The first is the water gas shift reaction involving the oxidation of carbon monoxide to carbon dioxide with the simultaneous formation of dihydrogen. It is possible to bypass this step by replacing carbon monoxide with dihydrogen. The second catalytic step involves the combination of dihydrogen with dioxygen to yield hydrogen peroxide (or its equivalent). The final step involves the metal catalyzed oxidation of the alkane by hydrogen peroxide (or its equivalent). The activation parameters for the overall reaction, determined under the condition when the rate is first-order in both methane and carbon monoxide, are: $A = 2 \times 10^4$ s^{-1}; $E_a = 15.3$ kcalmol^{-1}.
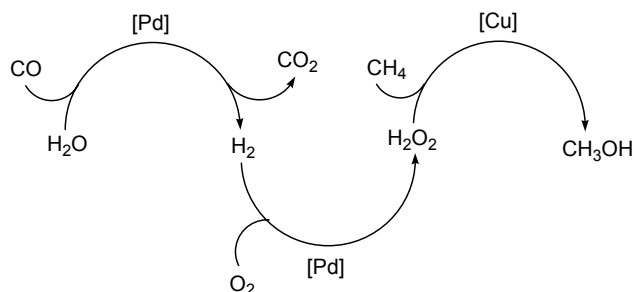
Scheme 1. Proposed catalytic three-step mechanism for methane oxidation.

The role of metallic palladium is two-fold. First, it generates hydrogen peroxide (or its equivalent). Second, it causes non-specific overoxidation of the substrate using the hydrogen peroxide thus generated. This latter reaction is suppressed when copper chloride is added; instead, copper chloride appears to catalyze the selective hydroxylation of the alkane by hydrogen peroxide. An interesting reactivity pattern exhibited by the bimetallic system is the preference for C-C cleavage over C-H cleavage for higher alkanes. Indeed, we are unaware of any other catalytic system that effects the oxidative cleavage of alkane C-C bonds under such mild conditions.

A curious aspect of the bimetallic system is that, apart from its ability to simultaneously activate both dioxygen and alkane, it requires a coreductant: carbon monoxide or dihydrogen. Thus, there is a striking resemblance with monooxygenases. In nature, while the dioxygenases utilize the dioxygen molecule more efficiently, it is the monooxygenases that carry out "difficult" oxidations, such as hydroxylation of alkanes. In the latter, one of the two oxygen atoms of dioxygen is reduced to water in a highly thermodynamically favorable reaction and the free-energy gained thereby is employed to generate a high-energy oxygen species, such as a metal-oxo complex, from the second oxygen atom.

The second catalytic procedure involves the gas-phase partial oxidation of methane and ethane to formaldehyde by dioxygen [10]. NO_x acts as catalyst and is *not* consumed in the reaction. The yield of oxygenates from methane is over 11%. The yield increases to over 16% when a trace of ethane (0.7%) is added to the gas mixture (Table 1). As might be expected, the yield of oxygenates from ethane is higher: over 24%. A catalytic cycle involving NO_2 as the C-H activating species is proposed (Scheme 2). The results that we have obtained thus far are noteworthy in several respects. First, the same C_1 product (formaldehyde) is obtained from both methane and ethane. Thus, the prior separation of the latter alkane is not required for this process. Second, in the context of partial oxidation of methane to oxygenates by dioxygen, there are few other system in the open literature that simultaneously exhibits such high conversion and selectivity.

Table 1. Methane Oxidation in Presence of Trace Ethane

Experiment No.	1	2
Temperature, °C.	600	600
Flow rate, mL/sec	2.26	5.65
Yield of CH_3OH^1, %	---	1.00
Yield of CH_2O^1, %	13.96	15.30
Yield of HCO_2H^1, %	2.27	0.64
Yield of CO^1, %	14.26	8.50
Total conversion^1, %	30.5	25.4
Selectivity^2, %	53.2	66.5
Yield^3, %	16.2	16.9
Total products, mmol.	3.08	6.21
[CH$_4$ (inlet) – CH$_4$ (outlet)] + CH$_3$CH$_3$ x 2, mmol	3.23	5.82

Gas mixture: CH_4, (16.6%); CH_3CH_3, (0.7%); NO, (11.0%); O_2, (5.5%); N_2, (16.6%); He, (49.7%).
1. Based on total carbon in CH_4 and CH_3CH_3.
2. Selectivity: $\Sigma(CH_2O + CH_3OH + HCO_2H)/\Sigma(\text{total products})$.
3. Yield: Total conversion x Selectivity.

CH₂O, HCO₂H, CO ← NO₂ ←

CH₄ → NO → O₂
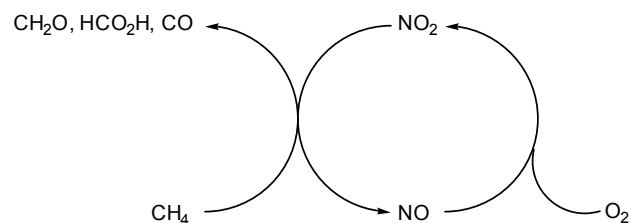
Scheme 2. Proposed mechanism for NO$_x$-catalyzed methane oxidation.

References
(1) M. G. Axelrod, A. M. Gaffney, R. Pitchai, and J. A. Sofranko, In *Natural Gas Conversion II*, H. E. Curry-Hyde and R. F. Howe (eds.), Elsevier, Amsterdam, **1994**, p. 93.
(2) A. Sen, *Top. Organomet. Chem.*, **1999**, *3*, 81.
(3) G. A. Olah, A. Molnár, *Hydrocarbon Chemistry*, Wiley, New York, **1995**.
(4) R. H. Crabtree, *Chem. Rev.*, **1995**, *95*, 987.
(5) T. J. Hall, J. S. J. Hargreaves, G. J. Huchings, R. W. Joyner, and S. H. Taylor, *Fuel Process. Technol.*, **1995**, *42*, 151.
(6) J. L. G. Fierro, *Catalysis Lett.*, **1993**, 2267.
(7) M. J. Brown and N. D. Parkyns, *Catalysis Today*, **1991**, 8305.
(8) M. Lin, T. Hogan, and A. Sen, *J. Am. Chem. Soc.*, **1997**, *119*, 6048.
(9) A. Sen, *Acc. Chem. Res.*, **1998**, *31*, 550.
(10) A. Sen and M. Lin, *Stud. Surf. Sci. Catal.*, **2001**, *136*, 227.

Ni/ADM: A HIGH ACTIVTY AND SELECTIVTY TO C$_{2+}$OH CATALYST FOR CATALYTIC CONVERSION OF SYNTHESIS GAS TO HIGHER ALCOHOLS

Debao Li, Kan Zhang, Wenhuai Li*, Yuhan Sun and Bing Zhong

State Key Laboratory Coal Conversion, Institute of Coal Chemistry, Chinese Academy of Sciences, Taiyuan, P.R. China 030001

Introduction

Commonly, methyl tertiary butyl ether (MTBE) is the primary oxygenates used for reformulated gasoline (RFE), however, recent issues showed that the application of MTBE could cause some disadvantages such as contamination of drinking water.[1] For a long time, higher alcohols (C$_1$-C$_5$) are thought as an potential additive to gasoline to boost octane number and reduce emissions. The current interest is focused on the application of this process to produce high value gasoline octane enhancers in view of both utilization of resources and environmental protection.[2-3]

Catalysts used for the production of higher alcohols can be classified into the following categories: (i) modified high-pressure methanol–synthesis catalyst; (ii) modified low-pressure methanol–synthesis catalyst; (iii) alkali-doped molybdenum sulfide (ADM) catalysts.[3-5] Among the various catalysts, alkali-doped molybdenum sulfide (ADM) catalyst was one of the most promising systems due to its higher selectivity to alcohols, higher activity for water-gas shift. Previous studies revealed that the additions of Co could enhance the higher alcohols (C$_2^+$) selectivity due to its strong ability to promote carbon chain growth, however the studies of other F-T elements such as Ni and Fe were fairly rare.[6-7]

It was well known that nickel was excellent for methanation, but its other catalytic capabilities have been neglected for a long time. Recent investigates on Ni-SiO$_2$ catalyst revealed that strong ability of CO insertion reaction and excellent resistance to sulfur poisoning for feed gas.[8-9] In present paper, we reported ADM catalyst modified by Ni, which showed high performance for higher alcohol synthesis(HAS).

Experimental

Catalyst Preparation. Ni/ADM (Ni/K$_2$CO$_3$/MoS$_2$) catalyst was prepared by co-precipitation method. The solutions of nickel(II) acetate Ni(CH$_3$COO)$_2$• 4H$_2$O and (NH$_4$)$_2$MoS$_4$ were dropped to the solution of acetic acid. After stirred and reacted thoroughly, the resulted solution was aged over night. After filtration, the precipitates was dried under vacuum followed by mixed with K$_2$CO$_3$ and thermal decomposed at 500℃ under N$_2$. ADM (K$_2$CO$_3$/MoS$_2$) catalyst was prepared by thermal decomposition of mixture of (NH$_4$)$_2$MoS$_4$ and K$_2$CO$_3$ at 500℃ under N$_2$. The catalysts were then pelleted and crushed to 40-60 mesh and stored in nitrogen for use.

Characterization Methods. X-ray powder diffraction (XRD) patterns of the tested catalysts were obtained on a Rigaku D/Max 2500 powder diffractometer using Cu Kα radiation as the X-ray source. SEM imagines were obtained using a LEO 438VP SEM (20KV).

CO Hydrogenation. The catalytic reactions were carried out using a stainless fixed-bed reactor with 2ml of catalyst. The products were analyzed by gas chromatographs The mass balance was based on carbon and the error of the balance of oxygen and hydrogen was within 5%. The activity of synthesis of alcohols was expressed as space-time-yield (STY), g ROH/Kg cat. h and the alcohols selectivity was based on carbon molar selectivity on a CO$_2$ free basis.

* Corresponding author. Fax: +86-351-4068405; E-mail:lwh@sxicc.ac.cn & leedebao@sohu.com

Results and Discussion

Table1 Performance of CO hydrogenation over Ni/ADM catalysts [a]

Catalyst	CO conv. (mol %)	STY (g/(ml • h))		Selectivity (mol%)	
		ROH	C$_{2+}$OH	Alc.	HC.
ADM Ni-ADM	17.02	101	42	76.21	23.79
Ni/Mo 1/4	20.31	119	77	73.44	26.56
1/3	34.11	160	130	69.89	30.11
1/2	28.02	138	113	70.78	29.22
1/1	18.68	124	60	76.90	23.10

[a]Reaction condition: T=573K, P=8.0MPa, GHSV=4000h^{-1} H$_2$/CO=1.0

Table 2 Alcohol distributions over Ni/ADM catalysts

Catalyst	Alcohols (C-atom %)				
	MeOH	EtOH	PrOH	BuOH	Others[b]
ADM Ni-ADM	51.78	32.86	10.92	4.05	0.39
Ni/Mo 1/4	29.20	47.23	17.15	6.01	0.41
1/3	13.27	33.84	27.11	23.26	2.53
1/2	13.28	35.36	28.97	19.92	2.46
1/1	36.66	47.42	11.63	3.68	0.61

[b] Includes C$_{5+}$OH, aldehydes, esters and ethers.

The results of CO hydrogenation were listed in **Table1** and **Table 2.** It can be seen that the promoter of Ni improved the CO conversion and STY of alcohols greatly. Moreover, the selectivity to higher alcohols (C$_2$-C$_4$) increased compared with that of traditional ADM catalyst. The remarkable effect of Ni promoter indicated that nickel had strong promotion for chain propagation. For the Ni/ADM catalyst, the optimum Ni/Mo ratio was about 1/3~1/2, at which the STY and CO conversion reached the maximum.
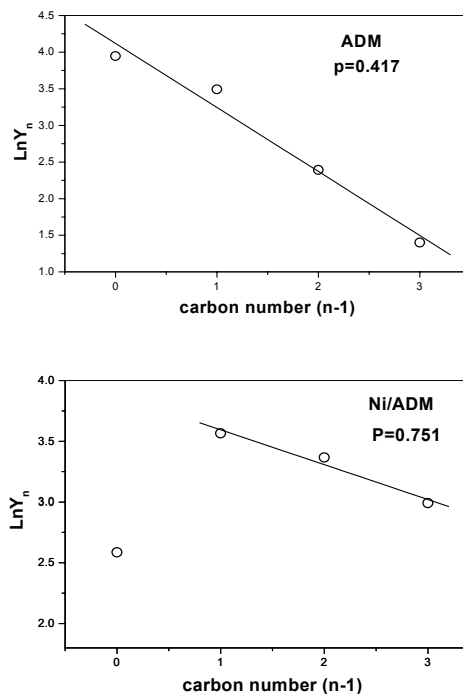

Fig. 1. A-S-F distributions of alcohol over ADM and Ni/ADM catalyst (Ni/Mo=1/2)

The individual distributions of alcohols over ADM and Ni/ADM catalysts were depicted in **Fig. 1**, as an A-S-F distribution:

$$Y_n = P^{n-1}(1 - P)$$

Where Y_n is the mole fraction of the alcohols with a carbon number of n and P is the chain-growth probability. Over ADM catalyst, the carbon number distribution of the alcohols obeyed the traditional A-S-F distribution. However, for Ni/ADM catalyst, methanol deviated the A-S-F distribution greatly. Moreover, the chain-growth probability P obtained through $C_2 - C_4$ alcohols was much higher than that of ADM catalyst. It seemed that the promoter Ni exerted strong promotion for carbon chain growth, especially for the step of C_1 to C_2.

For Ni/ADM catalyst, the morphology of Ni played an important role for the performances of HAS. The XRD patterns of Ni/ADM catalysts(**Fig.2**) showed clear crystal phases of Ni_2S_3. As the Ni/Mo ratio increased, the intensities of diffraction peaks also increased.
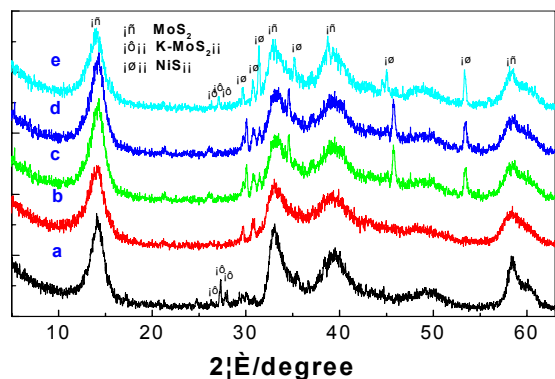

Fig. 2. The XRD patterns of catalysts
a.K_2CO_3/MoS_2,b.Ni/Mo=1/4,c.Ni/Mo=1/3,d.Ni/Mo=1/2,e. Ni/Mo=1

Scanning electron microscope (SEM) micrographs of catalysts were shown in **Fig.3**. The morphological differences among these samples were evident. The Ni/ADM samples showed an irregular shape and significant porosity, and the surface of the MoS_2 appeared covered with a great deal of small-conglutinated particles. In these micrographs a progressive surface decoration is observed as a function of the concentration of promoter nickel. With high concentration of nickel, the conglutination became weaker and larger particles were formed on the surface of MoS_2. Studies of metal catalysts with various dispersion revealed that the structure of some active element (such as Ni, Pd) played an important role for CO hydrogenation: catalysts with small crystallites had advantage to produce alcohols while larger crystallites to methane.[10] For Ni/ADM catalyst, the promoter of Ni showed similar structure effect. At the optimum Ni/Mo ratio, namely 1/3~1/2, there must have strong synergy effect between Ni and Mo which was favorite for Higher alcohols synthesis.
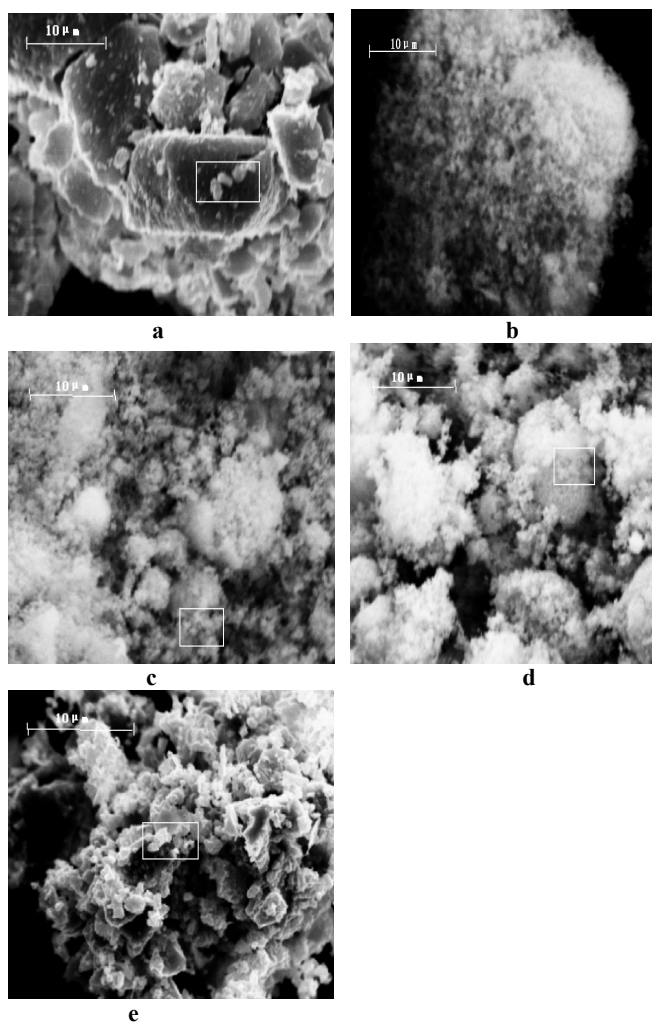
Acknowledgment

Fig. 3. SEM micrographs of catalysts
a ADM, Ni/ADM: b Ni/Mo=1/4, c Ni/Mo=1/3, d Ni/Mo=1/2, e Ni/Mo=1.

References
1. A. J. Lucero, R. E. Klepper, W. M. O'Keefe,and V. K. Sethi, *Fuel Chemistry Division Preprints*, **2001**, 46(2), 413.
2. A. Beretta, Q. Sun, R. G. Herman, K. Klier, *Ind. Eng. Chem. Res.*, **1997**, 36, 3085.
3. R. G. Herman, *Catal. Today*, **2000**, 55, 233.
4. Xiaoding Xu, B. M. Doesburg, J. F. Sckolen, *Catal. Today*, **1987**, 2, 125.
5. E. Tronconi, N. Ferlazzo, P. Forzatti, I. Pasquon, *Ind. Eng. Chem. Res.*, **1987**, 26, 2122.
6. G-Z Bian, Li Fan, Y-L Fu K.Fujimoto, *Ind. Eng. Chem. Res.*, **1998**,37, 1736.
7. J. Iranmahboob, D. O. Hill, H. Toghiani, *Appl. Catal.*, **2002**, 231, 99.
8. S. S. C. Chuang, S. I. Pien, *Catal, Lett.*, **1989**, 3, 323.
9. S. A. Hedrick, S. S. C. Chuang, A. Pant, A. G. Dastidar, *Catal. Today*, **2000**, 55 247.
10. Zhongrui Li, Yilu Fu et al., *Catal. Lett.*, **1989**, 65,43.

ATOM-ECONOMICAL REDUCTION OF CARBON MONOXIDE TO METHANOL: IS THE CATALYST SINGLE-SITE OR MULTI-SITE?

Devinder Mahajan

Energy Sciences and Technology Department, Brookhaven National Laboratory, Upton, New York 11973-5000 USA
and
Department of Materials Science & Engineering, Stony Brook University, Stony Brook, NY 11794 USA

Introduction

Hydrocarbons and methanol are considered the preferred products of catalytic reduction of carbon monoxide derived from clean natural gas. Pathways to these liquid energy carriers are collectively known as gas-to-liquid (GTL) technology. Methanol has particularly attractive attributes as a fuel, an additive in conventional fuels, and a versatile building block in the synthesis of chemicals[1,2]. Methanol is presently manufactured from synthesis gas using supported Cu/ZnO heterogeneous catalyst at 250 - 300°C and between 5 - 10 MPa operating pressure[3]. Methanol synthesis is highly exothermic (ΔH_{298} = - 128.6 kJ.mol^{-1}) that poses thermodynamic limitations and together with poor process heat control allows < 20% per pass gas conversion during the reaction[4]. A homogeneous catalyst that affords high reaction rates at low temperatures would offer superior reaction heat management, higher yields per pass, and may afford attractive economics. Efforts have been made to synthesize oxygenates from synthesis gas using homogeneous systems. The use of transition metal carbonyls specially those of Ru (5) and Rh (6) for synthesis of methanol, ethanol, other higher alcohols and ethylene glycol is well documented for synthesis gas conversion but with these systems the overall reaction parameters are not economically attractive.

We are investigating the use of single-site catalyst precursors to maximize CO conversion into methanol that may allow methanol production cheaply enough to consider methanol as a feedstock. We recently reported[5] the use of nickel complexes as versatile catalysts to homogeneously catalyze CO reduction to methanol under mild conditions of temperature (T: 80° - 130°C) and pressure (2000 - 5000 kPa). Under these conditions, CO conversion and methanol selectivity approach > 90% and > 95%, respectively. This paper describes the potential of the low temperature facile interconversion of various mono- and multi- nuclear Ni species under the reaction conditions and the role of such these species in defining the actual catalyst species in homogeneously catalyzed methanol synthesis.

Experimental

Materials. Potassium methoxide (>95% pure) and nickel complexes were purchased from Alfa and used as received. Methanol and p-dioxane were obtained from Aldrich and purified before use. Pure CO, H_2, and syngas mixture (66% H_2, 34% CO) were purchased from Scott Specialty Gases. Syngas mixtures were calibrated to reconfirm stoichiometries certified by the vendor.

Batch Studies. A commercially available stainless steel MagneDrive II Packless Zipperclave 0.5L reactor, manufactured by Autoclave Engineers, Inc. (AE) and modified for use in this study, is shown in Figure 1. The reactor was equipped with a Dispersamax six-blade impeller to ensure efficient gas/liquid mixing. Ports were provided for loading reactant gases, sampling vapor and liquid phases. The batch CSTR unit ratings were as follows: stirrer = O - 2000 rpm, T = 25 - 450 C, P = 100 - 14000 kPa.

Run Procedure. A specified amount of $KOCH_3$ and the Ni complex was weighed inside a Labconco glove box under N_2, mixed with the desired solvent mixture in the reactor and the reactor was quickly sealed after purging several times with N_2. The reactor was immediately pressurized with ~ 750 psig syngas, stirred and heated to the desired temperature. The temperature and pressure in the reactor were recorded until the pressure decreased to about 100 to 150 psig, at which time the reaction was quenched by replacing the heater with an ice-water bath. Once the reactor reached room temperature, the final pressure and temperature were recorded. Gas and liquid samples were taken for analysis and the final liquid volume was measured. Vapor and liquid phases were analyzed to obtain a mass balance for each run.
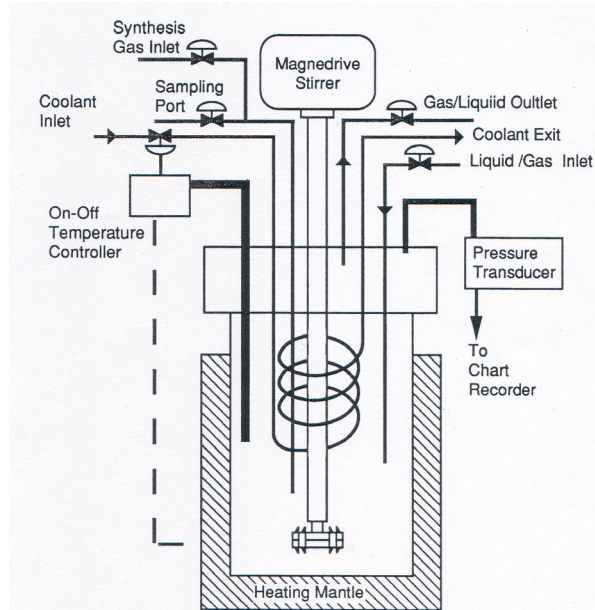

Figure 1. A modified AE Zipperclave batch unit for methanol synthesis.

Results and Discussion

Catalytic Activity Data. The activity data for homogeneous CO reduction to methanol catalyzed by various Ni complexes and activated by potassium methoxide base is shown in Table 1. The data show that the reaction is facile and CO, chloride and acetylacetonate (acac) ligated Ni complexes are versatile catalysts under mild temperature (120°C) and pressure (4700 kPa) conditions. In all 6 runs, the CO conversion per pass exceeded 90%. In Run 2, the triglyme co-solvent was replaced with tetrahydrofuran (THF) that resulted in an increase in reaction rate. The absence of potassium methoxide in Run 4 rendered the Ni catalyst totally inactive confirming the crucial role of the base in these reactions. The phosphine ligands are unsuitable for the reaction (Runs 6 and 7) and result in a totally inactive system. The selectivity to methanol was up to 99% and the by-products consisted of methyl formate (MF) and dimethyl ether (DME). Methane was observed only as a trace (< 0.001%). The rate data (mmol gas consumed/minute) in Table 1 were normalized to obtain batch rate data to yield a maximum rate of 20 g-mol MeOH.L Cat[-1].h[-1] at 120°C and 4700 kPa. The rates are higher as compared to the commercial system (6 MeOH.L Cat[-1].h[-1]/Lcat.h) that operates at a higher temperature of 250°C and a comparable pressure of 5000 kPa. It is to be emphasized that the solution remains homogeneous throughout the run.

Table 1. Catalytic activity of various Ni complexes for methanol synthesis.

Run	Catalyst	Batch Rate, mmol/min	Product Selectivity,%		
			MeOH	MF	DME
1	$Ni(CO)_4$	54	>99	<1	Trace
2	$Ni(CO)_4$	66	95.7	4	0.3
3	$NiCl_2$	98	99.2	0.2	0.6
4	$NiCl_2$	-	-	-	-
5	$Ni(acac)_2$	72	98	1.4	0.6
6	$Ni(PPh_3)(CO)_3$	-	No activity		
7	$Ni(PPh_3)_2(CO)_2$	-	No activity		

0.5 L AE Zipperclave batch reactor, Solvent: 90% Triglyme/10% MeOH = 120 mL, [Ni] = 0.05 M, KOMe = 1.0 M, Syngas: 66% H_2/34% CO, T = 120°C, P_I = 4700 kPa.

Mechanistic Considerations. The low temperature concept of methanol synthesis has been the subject of research by several groups[6]. The mechanistic study on a catalyst system that is closely related to the catalyst system presented here has been reported in literature[7]. A mechanistic cycle, shown in Figure 2, has been
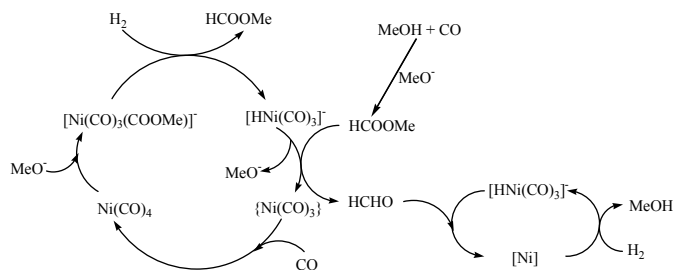

Figure 2. Proposed mechanistic pathway to methanol synthesis from balanced synthesis gas (H_2/CO = 2) catalyzed by homogeneous nickel complexes activated by sodium methoxide (from reference 6).

proposed based on the high-pressure infrared data[6]. This study emphasized FTIR as a tool to discern the mechanism of the $Ni(CO)_4$/NaOMe system. The proposed steps involve a nucleophilic attack of the methoxide anion ($^-$OMe) on a coordinated CO of $Ni(CO)_4$ followed by production of methyl formate (MF) and anionic hydridotricarbonylnickel species ($[HNi(CO)_3]^-$). Methyl formate is hydrogenated by the anionic Ni species to two moles of methanol via the intermediacy of formaldehyde and addition of CO regenerates $Ni(CO)_4$ to complete the catalytic cycle. The function of Ni is then primarily to hydrogenate methyl formate.

Though the proposed mechanistic cycle in Figure 2 is plausible, whether same intermediate species are involved during methanol synthesis catalyzed by the presented $Ni(CO)_4$/KOMe system needs to be confirmed. More importantly, it is suggested in Figure 2 that the mononuclear Ni species likely catalyzes CO reduction to methanol. We are presently investigating the role of
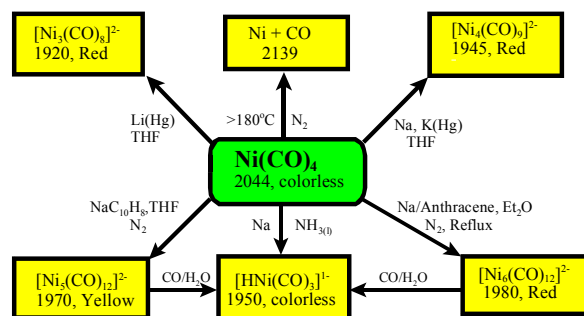

Figure 3. Possible interconversion of nickel carbonyl cluster anions (data from reference 8).

various Ni species that could potentially catalyze the methanol synthesis reaction at low temperatures. Related to this, a lot of work has been reported on the facile interconversion of Ni species[8,9] that is shown in Figure 3. The number in each box below the species represents the value of signature IR band and the cation associated with the anionic Ni species are selected from K^+, Na^+, Li^+, PPN^+, Me_4N^+. The Ni species in Figure 3 are mostly soluble in H_2O and are the result of the redox condensation reaction that is accompanied by a change in the oxidation state of Ni from Ni^0 to Ni^{2+}. A facile equilibrium may set up in the reactions shown in figure 3 as follows:

$$Ni(CO)_4 \quad \rightleftharpoons \quad [Ni_x(CO)_y]^{2-}$$
$$[Ni_x(CO)_y]^{2-} + H^+(H_2O) \quad \rightleftharpoons \quad [HNi_x(CO)_y]^{1-}$$
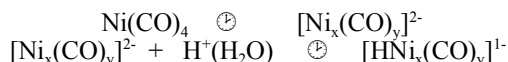
The foregoing information shows that the identification of the active catalytic species remains a challenge. Work is presently under to truly establish a pathway that makes the Ni based catalyst system so active for homogeneous methanol synthesis.

References
1. Keim, W., Editor. Catalysis in C_1 Chemistry, D. Reidel Publishing Company, Dordrecht, 1983. Keim, W. J. Organomet. Chem. **372** (1989), 15.
2. I. Wender, I. Catal. Rev. Sci. Eng. **26** (1985) 3.
3. Lee, S. Methanol Synthesis Technology, CRC Press, Inc., Boca Raton, Florida, 1990.
4. Strelzoff, S. Chem. Eng. Prog. Symp. Ser. **66** (1970) 98.
5. Mahajan, D., Krisdhasima, V., Sproull, R.D. Can. J. Chem. **79** (5/6) (2001) 848.
6. Marchionna, M., Lami, M., Raspolli Galletti, A.M. CHEMTECH, April 1997, 27 and references therein.
7. Marchionna, M., Basini, L., Arogno, A., Lami, M., Ancilloti, F. J. Mol. Catal. **75** (1992) 147.
8. Longoni, G., Chini, P., Cavalieri, A. Inorg. Chem. **15(12)** (1976) 3025.
9. Beattie, J.K., Hambley, T.W., Masters, A.F., Meyers, J.T. Inorg. Chim. Acta. **213** (1993) 49.

IN SITU ATR/FTIR OBSERVATION OF TRANSFORMATION OF THE NICKEL SPECIES IN LOW TEMPERATURE METHANOL SYNTHESIS

Seiichi Ohyama

Centra Research Institute of Electric Power Industry
2-11-1 Iwado-kita Komae-shi,
Tokyo 201 8511, Japan

Introduction

Low-temperature methanol synthesis rapidly proceeds in liquid media at temperatures of around 373 K over appropriate catalytic systems. Brookhaven National Laboratory claimed two active catalytic systems: the catalyst prepared from nickel acetate, *tert*-amyl alcohol and NaH (denoted as $Ni(OCOCH_3)_2$/*tert*-amyl alcohol/NaH)[1] and a mixture of $Ni(CO)_4$ and CH_3OK (denoted as $Ni(CO)_4/CH_3OK$).[2] Over these catalysts, methanol (MeOH) are considered to be formed through the carbonylation of MeOH to methyl formate (MF), followed by the subsequent hydrogenation of MF to MeOH:

$$CH_3OH + CO \rightarrow HCOOCH_3,$$
$$HCOOCH_3 + 2H_2 \rightarrow 2CH_3OH.$$
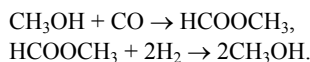
The author provided an illustration to indicate the above reaction pathway in $Ni(CO)_4/CH_3OK$ and showed that hydridocarbonylnickel anion ($[HNi(CO)_3]^-$ or $[HNi_2(CO)_6]^-$) derived from $Ni(CO)_4$ was responsible for the latter step of the reaction.[3] With regard to $Ni(OCOCH_3)_2$/*tert*-amyl alcohol/NaH, the catalytically active species still remains unknown. This study aims to identify the catalytically active form of $Ni(OCOCH_3)_2$ and also to clarify the relation between the two nickel precursors, *i.e.*, $Ni(OCOCH_3)_2$ and $Ni(CO)_4$ based on in situ ATR/FTIR observation.

Experimental

In place of $Ni(OCOCH_3)_2$/*tert*-amyl alcohol/NaH, $Ni(OCOCH_3)_2/CH_3OK$, *i.e.*, a mixture of $Ni(OCOCH_3)_2$ (5 mmol) and CH_3OK (20 mmol) was employed for the reaction. Also, $Ni(CO)_4/CH_3OK$ was employed for reference, which was composed of 5 mmol of $Ni(CO)_4$ and 20 mmol of CH_3OK. CH_3OK was employed in the form of 30% CH_3OK solution in methanol, 5 cm^3 of which contained 20 mmol of CH_3OK and 105 mmol of methanol. The catalysts were dispersed in triethylene glycol dimethyl ether (triglyme), forming 50 cm^3 of the solution.

The reaction was carried out in batch operation in an autoclave (175 cm^3), which housed an attenuated total reflectance (ATR) accessory. Syngas with a ratio of $H_2/CO = 2$ was pressurized into the reactor up to 3.0 MPa at 333 K. The gas and liquid components after the run were analyzed by GC. In situ FTIR spectra were collected on Nicolet Magna 560 FTIR spectrometer equipped with an MCT detector and the ATR probe (TerminatIR from ASI Applied Systems), the crystal of which was immersed in the liquid in the autoclave. The experimental details are described elsewhere.[3]

Results and Discussion

Figure 1 (A) illustrates the time courses of temperature and pressures during the run over $Ni(OCOCH_3)_2/CH_3OK$ and its corresponding FTIR spectra are shown in Fig. 1 (B). The reaction was conducted at 333 K, a lower temperature than usual, which retarded the reaction rate to observe transformations in the liquid phase. The pressure decreased immediately after charging syngas at 333 K. The reactor was held at 333 K for 21 h and the pressure fell to 0.45 MPa. Upon charging the syngas, the absorption at 1730 cm^{-1} assigned to the $\nu(CO)$ of MF was immediately generated (Fig. 1 (b))

and enlarged (Fig. 1 (c)-(d)), which was observed during the reaction (Fig. 1 (c)-(f)) except for the end of the run (Fig. 1 (g)).
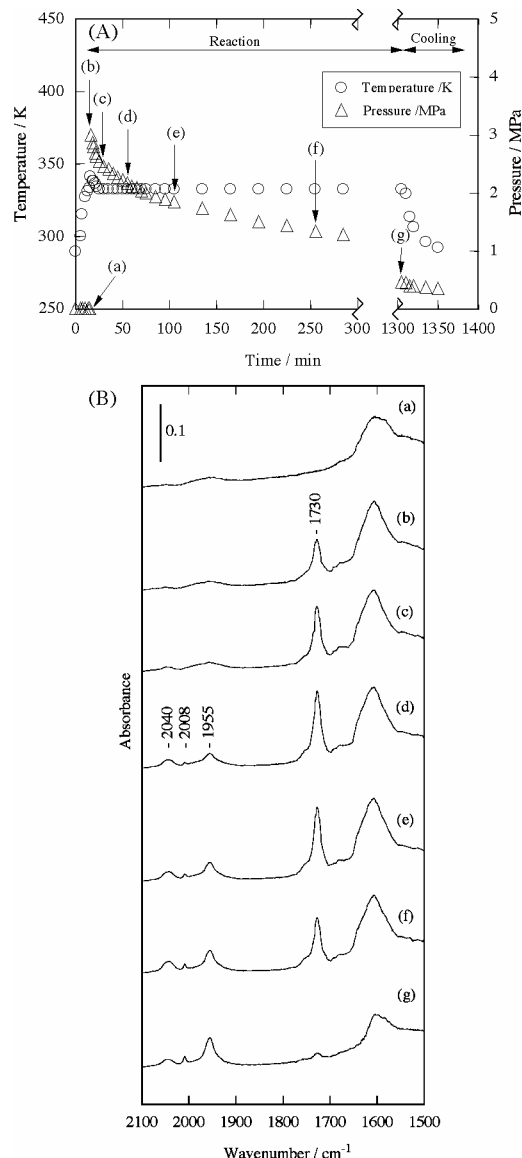

Figure 1. Time courses of temperature and pressure (A) and FTIR spectra (B) of $Ni(OCOCH_3)_2/CH_3OK$. The spectra (a)-(g) were collected at the corresponding points in figure (A).

For the first 10 min after charging the syngas, no absorptions were observed in the region of 2100-1800 cm^{-1} as shown in Fig. 1 (b)-(c). However, after 10 min, three small absorptions were recognized simultaneously at 2040, 2008 and 1955 cm^{-1} (Fig. 1 (d)). The bands showed a slight and monotonous increase (Fig. 1 (e)-(g)). The band at 2040 cm^{-1} was assigned to $Ni(CO)_4$, whereas the other bands at 2008 and 1955 cm^{-1} would be assigned to hydridocarbonylnickel anions ($[HNi(CO)_3]^-$ or/and $[HNi_2(CO)_6]^-$).[4] These two hydridocarbonylnickel anions have similar IR frequencies in the region and are labile and interchangeable with each other.[4] Thus, it is uncertain whether the bands represent $[HNi(CO)_3]^-$, $[HNi_2(CO)_6]^-$ or a mixture of both. To simplify the discussion, we just refer them to the hydridocarbonylnickel anion. Consequently, in situ observation of the solution revealed that the homogeneous nickel

species, i.e., Ni(CO)$_4$ and the hydridocarbonylnickel anion were simultaneously generated from Ni(OCOCH$_3$)$_2$ under the reaction condition.

Figure 2 illustrates time courses of MeOH and MF concentrations during the run, which were determined from the absorptions at 3500 and 1730 cm^{-1}, respectively. MF showed a rapid and immediate increase after the syngas charge. After the MF concentration became high and saturated (10 min after the syngas charge), the MeOH concentration began to increase sluggishly and showed a monotonous increase through the run. Meanwhile, MF gradually diminished and quite low at the end of the run. These products profiles showed a pattern typical of a consecutive reaction involving MF as an intermediate for the formation of MeOH, which indicates that in Ni(OCOCH$_3$)$_2$/CH$_3$OK, MeOH is produced on the same pathway as in Ni(CO)$_4$/CH$_3$OK.[4] Furthermore, formation of the nickel anion corresponded to the increase of the MeOH concentration. This supports the fact that the nickel anion catalyzes the hydrogenation of MF to MeOH, because we have already confirmed that Ni(CO)$_4$ itself does not catalyze the hydrogenation of MF.[4] Thus, the low-temperature methanol synthesis proceeds as homogeneous liquid phase reaction even in Ni(OCOCH$_3$)$_2$/CH$_3$OK as well as in Ni(CO)$_4$/CH$_3$OK.
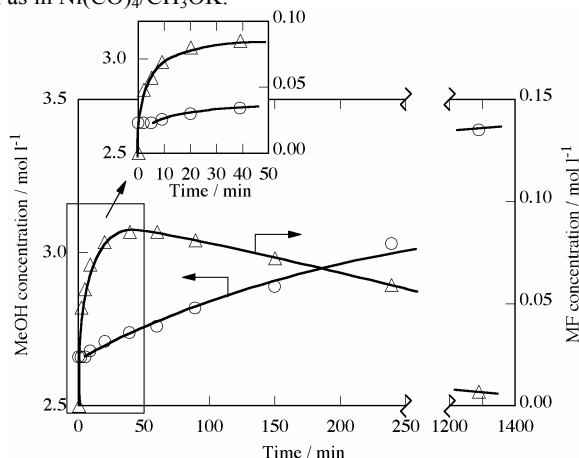

Figure 2. Variations in the concentrations of MeOH and MF during the run. The charging point of syngas was set at 0 min in the time scale.
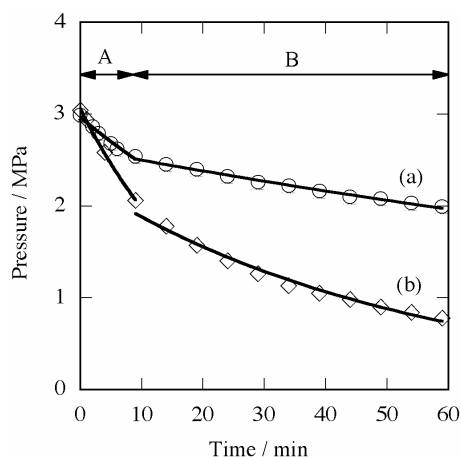

Figure 3. Time courses of pressure during the run. Catalyst: (a) Ni(OCOCH$_3$)$_2$/CH$_3$OK; (b) Ni(CO)$_4$/CH$_3$OK.

Figure 3 compares pressure profiles over Ni(OCOCH$_3$)$_2$/CH$_3$OK and Ni(CO)$_4$/CH$_3$OK with the runs performed at 333 K and 3 MPa. Ni(CO)$_4$/CH$_3$OK exhibited a larger pressure drop than

Ni(OCOCH$_3$)$_2$/CH$_3$OK. Assuming that the reaction rate obeys the first-order kinetics, two different fitting curves were applied to each pressure drop profile. The profiles were classified into two regions (denoted as A and B in Fig. 3). Good first-order rate plots were obtained over the both regions for the both catalysts. Based on in situ FTIR observations, it is apparent that the carbonylation of MeOH to MF exclusively proceeded over region A (the first 10 minutes after the syngas charge), whereas the hydrogenation of MF to MeOH limits the overall reaction rate in region B. The rate constants over region A are similar; 3.1×1^{-4} and 7.3×10^{-4} sec^{-1} for Ni(OCOCH$_3$)$_2$/CH$_3$OK and Ni(CO)$_4$/CH$_3$OK, respectively. This is reasonable because the both catalytic systems employed the same amount of CH$_3$OK as a catalyst component for the carbonylation of MeOH. In contrast, in region B, the rate constant for Ni(CO)$_4$/CH$_3$OK was 4 times higher than that for Ni(OCOCH$_3$)$_2$/ CH$_3$OK (3. ×1^{-4} and 8.0×10^{-5} sec^{-1}, respectively). The difference in the rate constant would be attributed to the amount of the catalytically active nickel species, i.e., the hydridocarbonylnickel anion. As shown in **Figure 4**, the absorptions assigned to the nickel anion (2008 and 1955 cm^{-1}) is 5 times larger in Ni(CO)$_4$/CH$_3$OK than in Ni(OCOCH$_3$)$_2$/CH$_3$OK, whereas the absorption assigned to Ni(CO)$_4$ (2040 cm^{-1}) was similar in intensity for both the catalytic systems. Thus, the ratio of the rate constants over the region B roughly agrees with the ratio of the absorptions assigned to the nickel anion, which indicates that the nickel anion is responsible for the hydrogenation of MF.
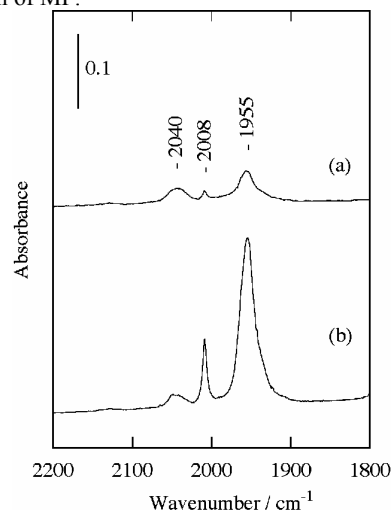

Figure 4. In situ FTIR spectra of (a) Ni(OCOCH$_3$)$_2$/CH$_3$OK and (b) Ni(CO)$_4$/CH$_3$OK at 333 K.

In summary, we concluded that under the reaction condition, part of Ni(OCOCH$_3$)$_2$ was converted into tetracarbonylnickel (Ni(CO)$_4$) and the hydridocarbonylnickel anion, the latter of which was responsible for the MF hydrogenation step in the low-temperature methanol synthesis. The difference in the catalytic activity between Ni(OCOCH$_3$)$_2$/CH$_3$OK and Ni(CO)$_4$/CH$_3$OK was explained by the concentrations of the hydridocarbonylnickel anion.

References
(1) R.S. Sapienza, W.A. Slegeir, T.E. O'Hare and D. Mahajan, *US Patent* 4,614,749, **1986**; 4,619,946, **1986**; 4,623,634, **1986**.
(2) D. Mahajan, R.S. Sapienza, W.A. Slegeir and T.E. O'Hare, *US Patent* 4,992,480, **1991**.
(3) S. Ohyama, *Appl. Catal. A*, 2001, **220**, 235.
(4) M. Marchionna, L. Basini, A. Aragno, M. Lami and F. Ancillotti, *J. Mol. Catal.*, **1992**, 75, 147.

MAPPING METAL CATALYSTS USING SYNCHROTRON COMPUTED MICROTOMOGRAPHY (CMT) and MICRO X-RAY FLUORESCENCE (μXRF)

K. W. Jones[1], H. Feng[2], and D. Mahajan[3]

[1]Laboratory for Earth and Environmental Sciences, Environmental Sciences Department, Brookhaven National Laboratory, Upton, New York 11973-5000 USA
[2]Department of Earth and Environmental Studies, Montclair State University, Montclair, NJ 07043 USA
[3]Energy Sciences & Technology Department, Brookhaven National Laboratory, Upton, NY 11973-5000, USA and Department of Materials Science & Engineering, Stony Brook University, Stony Brook, NY 11794 USA

Introduction

Gas-to-liquids (GTL) remains a viable pathway to synthesize clean fuels that are derived from natural gas, a clean energy source. There have been technological advances in natural gas conversion technology to a point that, for example, has led several companies to make investment in the Fischer-Tropsch route to synthesize clean hydrocarbon fuels. But a highly efficient gas conversion process that will allow companies to capitalize on remote natural gas in Alaska and other parts of the world still remains elusive. A major breakthrough is sought in developing a new catalyst that combines the environmentally sound process design.

Heterogeneous catalyst assemblies are typically utilized in the GTL conversion reactions. An in-depth characterization of catalytic materials is needed to design the next-generation catalyst. Computed Microtomography (CMT) and micro X-ray fluorescence (μXRF), techniques available at the National Synchrotron Light Source (NSLS), Brookhaven National Laboratory (BNL), are complementary techniques that allow mapping of catalyst constituents.

CMT is a non-invasive method that produces visualization of the interior of specimens based either on their linear x-ray attenuation coefficients or on the emission of characteristic x-rays from specific elements. The XRF technique uses a micrometer-size beam to make point-by-point measurements on elemental distributions in a thin section of a sample. This is a destructive method, but is valuable since the minimum-detection limits are superior to other methods.

Catalysts proposed for GTL work include Fe, Co, and Mn micron-sized or nano-sized particles supported on substrates of γ-alumina, silica, and potentially polymeric compounds. A schematic representation of the material is shown in Figure 1. While the individual catalyst particles are less than .001 mm in size, the presence of larger-sized clusters and the distribution in the support matrix can be effectively measured using CMT and XRF. Here, we draw attention to previous work on catalysts using these techniques through the presentation of results obtained on several catalytic materials. Improvements to the CMT apparatus now make possible high-spatial resolution measurements that show the microstructure of supported catalysts on mm-size scales. Methods of data analysis have also developed rapidly so that it is now possible to determine porosity, pore structures and connectivities for these 3-dimensional data sets. It is also feasible to determine property changes following use of the catalysts in a GTL reactor. This capability will have direct applications in the development and tests of GTL reactors.
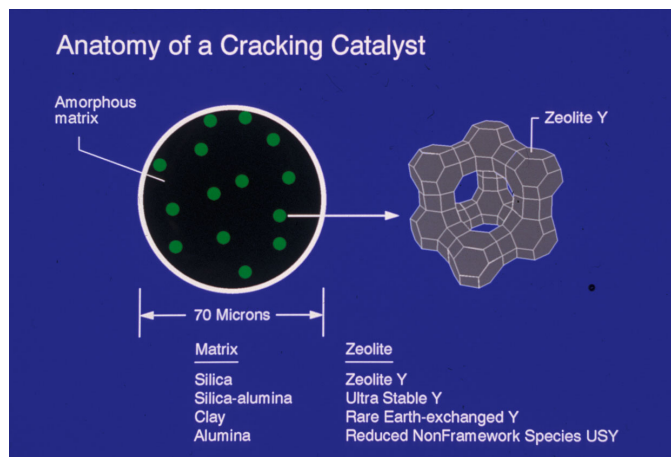

Figure 1. This schematic diagram shows the components of a supported catalyst particle.

Experimental

Apparatus. The experiments were performed at the National Synchrotron Light Source (NSLS) at BNL using several bending magnet beam lines. The synchrotron x-ray source provides high-intensity beams of x-rays that are the key to making measurements that are not feasible with conventional x-ray apparatus. The CMT work was done using a collimated beam of x rays to produce images with a scan-translate approach. The XRF work was also performed by accumulating images during a raster scan over an area of a thin section of the supported catalyst of interest. The spatial resolutions for the measurements were less than .010 mm.

Sample Preparation for CMT Measurements. The experiments were done at atmospheric pressure. The sample size was generally of the order of 1 - 10 mm. Thin sections were obtained using a microtome. We used two types of samples: Ni-Mo hydro-treating catalysts and Cr-SiO$_2$ polyethylene polymerization particles[1-4].

Results and Discussion

The work on the Ni-Mo hydrotreating catalysts made non-destructive sections through used and unused catalysts. As can be seen in Figure 2, the used catalyst shows evidence for an increase of the linear x-ray attenuation coefficient at the periphery of the particle and an increase in the amount of porosity in the interior of the particle when compared to the section through the unused particle. The distribution of Mo in these particles can be found by making measurements just above and just below the Mo K-x ray absorption edge and then subtracting the two images to determine the Mo contribution. The result of this experiment is shown in Figure 3.
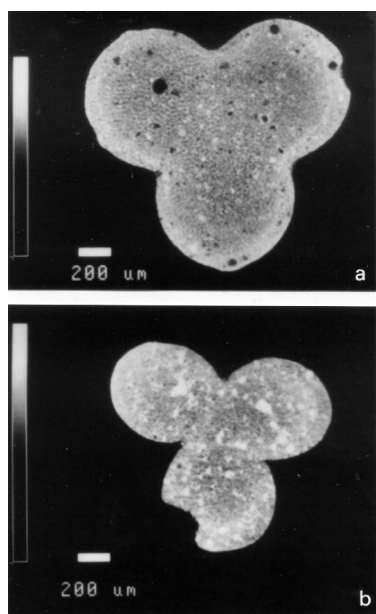
Figure 2. The tomographic slice obtained for a used Ni-Mo hdyrotreating catalyst is shown in Figure 2a and for an unused catalyst in Figure 2b.

The production of polymerization particles with the silica-based Cr catalyst is one that relies on fragmentation of the catalyst and a subsequent distribution through the polymer. Measurements were made on the particles using the CMT techniques described above. Thin sections were also made of a particle and maps were made of the distribution of the Cr using μXRF. The detection limit for Cr was roughly 10 parts-per-million by weight. The map obtained for the Cr distribution is shown in Figure 4. It can be seen that there is a rather constant concentration of Cr observed over the entire section with the exception of two regions where the enhance Cr concentration is evidence for only a partial disintegration of the catalyst.
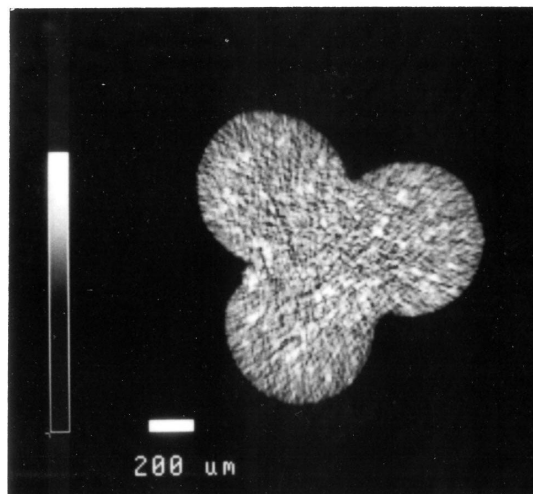

Figure 3. Mo concentration found is tomographic section of an unused Ni-Mo hydrotreating catalyst.
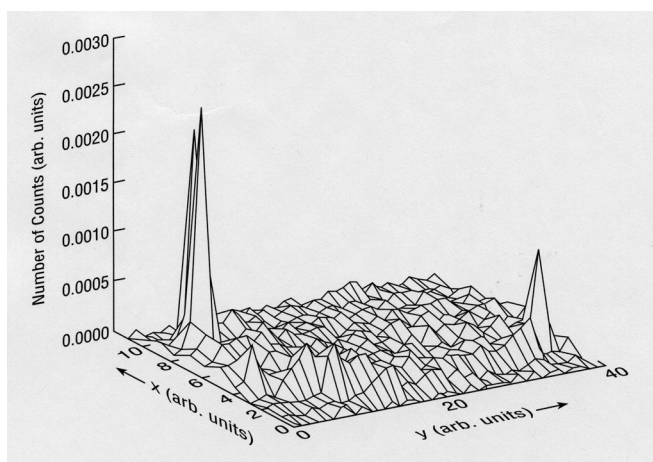

Figure 4. Distribution of Cr observed in a section of a polyethylene polymerization particle.

Conclusions

We have presented data illustrating the application of synchrotron based x-ray techniques to the study of hydrotreating and polyethylene polymerization catalyst. The CMT is a versatile technique for mapping changes in the composition of the catalyst constituents that in turn affects the catalytic activity. It is especially the case of F-T products that produce a significant amount of high molecular weight waxes that can clog the catalyst pores and adversely affect the catalyst performance over time. We are now focusing our work on imaging F-T catalysts. We hope to measure the changes in catalyst porosity that is so crucial to control the reactant gases to pass through the catalyst material to reach the active catalyst sites. The versatility of the CMT technique will allow us to monitor changes in the catalyst composition before and after the F-T reaction. The presented results show that the application of present state-of-the-art methods will be of great importance for work on GTL processes.

References
1. Conner, W. C., Webb, S. W., Spanne, P., and Jones, K. W. The use of x-ray microscopy and synchrotron microtomography to characterize polyethylene polymerization particles. Macromolecules 23, 4742-7 (1990).
2. Jones, K. W., Spanne, P., Webb, S. W., Conner, W. C., Beyerlein, R. A., Reagan, W. J., and Dautzenberg, F. M. Catalyst analysis using synchrotron x-ray microscopy. Nucl. Instrum. Methods B56/57, 427-32 (1991).
3. Ferrero, M. A., Sommer, R., Spanne, P., Jones, K. W., and Conner, W. C. X-ray microtomography studies of nascent polyolefin particles polymerized over magnesium chloride-supported catalysts. J. Polymer Science: Part A: Polymer Chemistry 31, 2507-12 (1993).
4. Jones, K. W., Berry, W. J., Borsay, D. J., Cline, H. T., Conner, W. C., Jr., and Fullmer, C. S. Applications of synchrotron radiation-induced x-ray emission (SRIXE). X-Ray Spectrometry 26, 350-8 (1997).

CATALYTIC CONVERSION OF METHANE TO METHANOL OVER LANTHANUM-COBALT-OXIDE SUPPORTED MOLYBDENUM BASED CATALYSTS

Xin Zhang, Dehua He*, Qijian Zhang, Boqing Xu and Qiming Zhu

State Key Laboratory of C_1 Chemistry and Technology,
Department of Chemistry, Tsinghua University
Beijing 100084, P.R. China

Introduction

Selective oxidation of methane is one of the most attractive potential industrial processes for the use of abundant natural gas resources. In the past decades, a great deal of effort has been made to develop catalysts and understand catalytic properties [1-2]. The MoO_3/SiO_2 and V_2O_5/SiO_2 catalysts have been reported to be the most active in the production of methanol [1-2]. The Mo(V)-loading has significant effects on the properties such as structure and reducibility of the catalysts, which determine the catalytic performance [1-2]. Generally speaking, the catalysts with the low Mo(V)-loading (high dispersion) show good activity and selectivity compared to the catalysts with the high Mo(V)-loading [1-2]. The participation of the lattice oxygen species (O^{2-}) or the adsorbed oxygen species (O^-) playing important roles on the formation of C_1-oxygenate has not been clear [1-2]. Other carriers such as Al_2O_3, Al_2O_3-SiO_2, MgO, TiO_2, TiO_2-SiO_2, SnO, ZnO_2, HZSM-5 and US-Y etc. have been used to support MoO_3 (V_2O_5), but their catalytic performances are quite poor [1-2]. Therefore, it is necessary to develop the effective catalysts for selective oxidation of methane to methanol.

The pervoskite-type oxide such as $LaCoO_3$ has high ability to activate and diffuse oxygen, due to its structure deficient. To our knowledge, such oxide catalysts showed good activity in combustion of methane, partial oxidation of methane to syngas, and oxidative coupling of methane etc. The pervoskite-type oxide supported Mo-based catalysts for selective oxidation of methane to C_1-oxygenate have been scarcely studied so far. Here, we report the catalytic performance of MoO_x/La-Co-oxide catalysts with the low Mo-loading in selective oxidation of methane, and characterize the properties of the catalysts so as to establish their relation to catalytic performance.

Experimental

Catalysts preparation. La-Co-oxide was prepared by using citric acid sol-gel method as described in elsewhere [3]. The Mo/La-Co-oxide catalysts (described as n-MLC, in which n express wt% of Mo) were prepared by impregnation of La-Co-oxide powder with different amount of $(NH_4)_6Mo_7O_{24}$ (Tianjing Chemical Co. Ltd., A.R.) aqueous solution. The precursor was dried at 383 K for 8 h, and calcined at 773 K for 8 h.

Catalytic test. Catalytic test was carried out in a continuous vertical-flow fixed-bed reactor, which was a 460 mm long quartz line tube (6.7 mm *i.d.*) tightly fixed in a stainless steel tube. Flow rate of reactant was controlled by a mass flow controller (Brooks 5850E serried) and pressure was controlled by a back-pressure regulator (Tescom Co.). Effluent gas kept at 423 K was analyzed by on-line gas-chromatograph (SHIMADZU, GC-8A, TCD) equipped with two columns: GDX-403 for separating CH_3OH, HCHO, C_2H_4, C_2H_6, H_2O, CO_2, and TDX-01 for N_2, O_2, CH_4, CO. The addition of N_2 in feed gas acted as both diluent and internal standard.

Characterization methods. The BET surface areas of catalysts were measured by using nitrogen adsorption/desorption isotherms method in ASAP-2010C adsorptionmeter. XRD measurement was carried out by BRUKER D8 Advanced X-rays powder diffractometer with Cu $K\alpha$ (λ=0.15046 nm). LR spectra were recorded on RENISHAW RM1000 Raman spectrometer quipped with He^+/Ne^+ laser (λ=514 nm, W=15 mW). TPR experiments of the samples were carried out in home-buildt TPR apparatus. XPS measurements were performed by PE PHI-5300 ESCA spectrometer, Al $K\alpha$ (1486.6 eV, 10.1 kV).

Results and Discussion

The results of catalytic test are shown in **Table 1**. Firstly, the effect of gas-phase homogeneous oxidation of methane was investigated. The reactor packed with quartz wool at constant temperature zoon (blank test) showed 4.9% CH_3OH selectivity at low CH_4 conversion, indicating that the gas-phase oxidation of methane had no great contribution to the formation of CH_3OH under such reaction conditions. In order to minimize the contribution of any gas-phase reactions, the space of up and down the catalyst bed (0.5 g, 20~40 mesh) was filled with quartz wool. The La-Co-oxide alone demonstrated the activity in combustion of methane. MoO_3 showed 6.9% HCHO selectivity with 1.6% CH_4 conversion. Catalytic performance of MoO_x/La-Co-oxide catalysts strongly depended on the Mo-loading. The highest CH_3OH selectivity (*ca.* 60%) and yield (*ca.* 6.7%) were achieved on the 7%wt Mo/La-Co-oxide. The results suggest that the synergetic effect between molybdenum oxide and La-Co-oxide occurred, and molybdenum oxide might be active sites for the formation of methanol.

It can be seen from **Table 1** that the BET surface areas of the MLC catalysts slightly increased with increasing Mo-loading. XRD results show that both La-Co-oxide and MoO_x/La-Co-oxide catalysts were mainly composed of $LaCoO_3$ and Co_3O_4 (**Figure 2**). LRS was used to determine the molecular structure of molybdenum oxide. The molybdenum oxide on the 3%wt Mo/La-Co-oxide catalyst was the isolated $[MoO_4]^{2-}$ species (889 and 858 cm^{-1}) [4]; likewise, the isolated and distorted $[MoO_4]^{2-}$ species (912, 821 and 322 cm^{-1}) located on the 7%wt Mo/La-Co-oxide catalyst [4]. The $[Mo_7O_{24}]^{6-}$ species (930 cm^{-1}) were detected on the 10%wt Mo/La-Co-oxide catalyst [4]. The XRD and LRS results indicate that molybdenum oxide was amorphous and its molecular structure depended on the Mo-loading. Considering the results of catalytic test, the studies reveal that the isolated and distorted $[MoO_4]^{2-}$ species enhanced the production of CH_3OH since $Mo-OCH_3$ intermediate might easily generate and transfer to CH_3OH on the species.
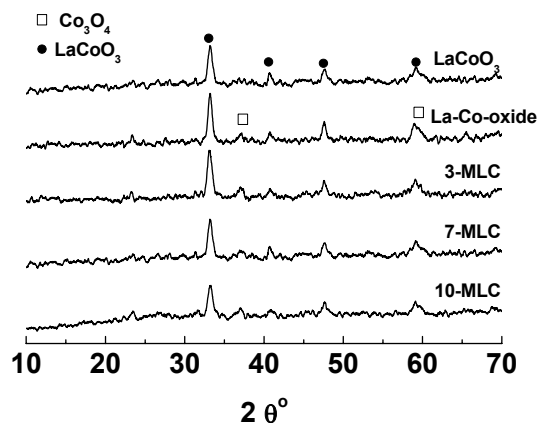

Figure 1. XRD patterns of the catalysts

Table 1 Catalytic performance of these catalysts in selective oxidation of methane to methanol

Catalysts	$S_{BET}(m^2/g)$	Temp (^{o}C)	Conv CH$_4$ (%)	Selectivity %			Yield %
				CH$_3$OH	CO	CO$_2$	CH$_3$OH
Reactor	-	420	0.9	4.9	43.1	51.8	0.04
La-Co-oxide	10.8	420	4.2	-	8.6	91.4	-
3-MLC	10.8	420	8.9	28.8	11.2	60.0	2.6
5-MLC	10.6	420	10.2	41.6	21.5	36.8	4.2
7-MLC	11.2	380	5.0	5.0	59.1	35.7	0.3
		400	9.2	31.4	41.8	26.6	2.9
		420	11.2	60.0	21.8	18.2	6.7
		460	11.4	38.2	36.5	25.3	4.3
10-MLC	11.8	420	11.6	33.2	31.7	34.8	3.9
MoO$_3$	-	420	1.6	6.9HCHO	40.8	52.2	0.1HCHO

Reaction conditions: 4.2 MPa, CH$_4$/O$_2$/N$_2$=9/1/1, 14400 ml/(g.cat).h^{-1}.

XPS studies indicate a slight increases of binding energy of Co$_{2p}$, La$_{3d}$ and Mo$_{3d}$ with increasing Mo-loading. The results imply that the deficient sites gradually reduced in the catalysts with the Mo-loading, leading to weaken the electron shield for the nucleus of ions. Detailed analysis and Lorentizian curve fitting of the O$_{1s}$ XPS spectra reveal the existence of oxygen species in mixed value state on the catalysts: O$^{2-}_{1s}$ at 528.8~529.0 eV, O$^{-}_{1s}$ at 530.1~530.2 eV and OH^{-}/CO$_3^{2-}$ at 532.1~532.5 eV [3, 5]. The O^{-}/O^{2-} ratio can be estimated according to the area of these sub-peaks. It is worth of noticing, the O^{-}/O^{2-} ratio gradually reduced with the increase of Mo-loading.
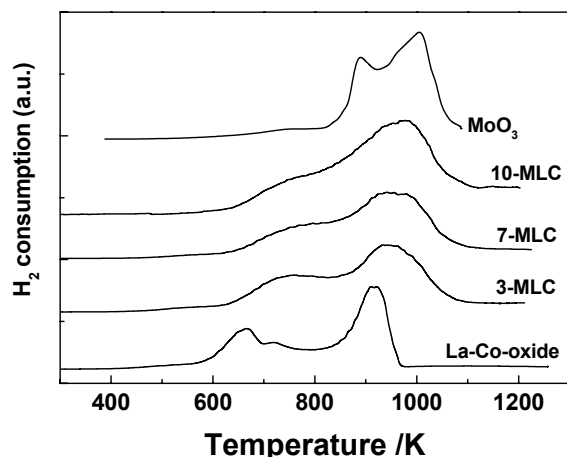

Figure 2. H$_2$-TPR profiles of the catalysts

Figure 2. gives some useful information of the reducibility of the catalysts. The TPR peaks temperature shifted toward the high temperature with the increase of Mo-loading. And, the TPR profiles of the MoO$_x$/La-Co-oxide catalysts were different from those of both La-Co-oxide and MoO$_3$. The results further indicate that the interaction between molybdenum oxide and La-Co-oxide occurred, which modified the reducibility of the catalysts. In addition, the reducibility of MoO$_x$/La-Co-oxide catalysts gradually reduced with the increase of the Mo-loading. The H$_2$ consumption of the MLC catalysts slightly increased with the Mo-loading, probably due to the increase of the reducible oxide species.

The results obtained in this work clearly show that molybdenum oxide loading on the carrier La-Co-oxide induced some change of properties such as molybdenum oxide structure, reducibility, oxidation state of ions, and surface composition, which in turn determined the catalytic performance. The effects were a function of the Mo-loading.

The changes of properties of the MLC catalysts might be due to the occurrence of interaction between molybdenum oxide and the La-Co-oxide. The electronegativity of Mo^{6+} is 2.16, Co^{3+} is 1.88 and La^{3+} is 1.08 [6]. Hence, the differences of the ions electronegativity resulted in the interaction. The catalysts with the low Mo-loading showed the strong interaction compared to the catalysts with the high Mo-loading, leading to more deficient sites and high reducibility. The deficient sites and reducibility influenced the activation and transform of oxygen species as the sequence: O$_2$ $_{(gas)}$ $\Leftrightarrow$ O$_2$ $_{(surface)}$ $\Rightarrow$ O^{2-} $_{(surface)}$ $\Rightarrow$ O$_2^{2-}$ $_{(surface)}$ $\Leftrightarrow$ O^{-} $_{(surface)}$ $\Rightarrow$ 2O^{2-} $_{(lattice)}$ [3, 5], therefore, the O^{-}/O^{2-} ratio varied with the Mo-loading.

The reducibility and the O^{-}/O^{2-} ratio were close relation to the catalytic performance. It is well known that both O^{-} species and O^{2-} species are active in selective oxidation of methane to methanol [1-2]. And, it seems that the O^{-} species are more active than the O^{2-} species [1-2]. However, the O^{-} species also have high activity in oxidation of methanol [3]. Likewise, the proper improvement of reducibility can enhance the activation of methane [1-2]. The much high reducibility can result in deep oxidation of methane and methanol [1-2]. Hence, it is necessary that the catalysts with the proper reducibility and the O^{-}/O^{2-} ratio enhanced the production of methanol in selective oxidation of methane.

References
1. Tabata K, Teng Y, Takemoto T, Suzuki E, Banares M.A, Pena M.A, and Fierro J.L, *Catal. Rev.,* **2002**, *44(1)*, 1-58
2. Faraldos M, Banares M.A, Anderson J.A, Hu H, Wachs I.E, Fierro J.L.G, *Fuel.Process.Tech*. **1995**, *42,* 214-225.
3. Wang W, Zhang H.B, Lin G.D, Xiong Z.T, *Appl.Catal. B*., **2000**, *24*, 219-232.
4. Mestl G, Srinivasan T.K.K, *Catal. Rev-Sci. Eng.*, **1998,** *40(4)*, 451-570.
5. Wan H.L, Zhou X.P, Weng W.Z, Long R.Q, Chao Z.S, Zhang W.D, Chen M.S, Luo J.Z, Zhou S.Q, *Catalysis Today* **1999**, *51 (1)*, 161-175.
6. Weast R.C, Astle M.J.A, Beyer W.H, *CRC Handbook of Chemistry and Physics*, 64th EDITION, CRC Press, Inc. Boca Raton, Florida.

Biomimetic Oxidation Studies: Alkane Functionalization in Aqueous Solution Utilizing Methane Monooxygenase Model Enzyme Assemblies

Karine Neimann,[a] Ronny Neumann,[a] Alain Rabion,[b] and Richard H. Fish [b]

[a]Department of Organic Chemistry, Weizmann Institute of Science, Rehovot, Israel 76100 [b]Lawrence Berkeley National Laboratory, University of California, Berkeley, California, 94720

Introduction

Methane monooxygenase (MMO) and cytochrome P-450 enzymes, although active in aqueous media, have a structure wherein the diiron non-porphyrin and iron porphyrin active sites, respectively, are embedded within a hydrophobic pocket, which enables the uptake and subsequent functionalization (hydroxylation) of alkanes. In the continuing search for biomimetic models for these metalloenzyme oxidation catalysts, the emphasis is usually placed on the structure of the active site, and if this biomimic can perform alkane functionalization chemistry. Generally, the macroenvironment and the efficacy of the oxidation process in aqueous media with the various monooxygenase model complexes has not been a focus of the bioinorganic catalysis community. Nevertheless, for metalloporphyrins, some significant research has been directed toward alkene epoxidation and alkane functionalization in aqueous media, by embedding the active site model compounds within lipid bilayers, thermotropic liquid crystals, and micelles. However, in the more nascent field of MMO biomimetic catalysis, the question of the macroenvironment and the possibility of alkane functionalization in aqueous media has not been extensively studied.[1]

In order to study the functionalization of hydrophobic alkanes in aqueous media using a biomimetic MMO enzyme assembly, including the active site and a hydrophobic pocket, we have developed both a derivatized amorphous silica, which allows one to balance the hydrophilicity and the hydrophobicity of a silicate surface, and a classically formed aqueous micelle system utilizing a cationic surfactant, cetyltrimethylammonium hydrogensulfate.[1] In our derivatized amorphous silica technique, hydrophilic poly(ethylene) oxide (PEO) and/or hydrophobic poly(propylene) oxide (PPO) were covalently attached to siloxane monomers. The siloxane monomers were then polymerized using sol-gel synthesis that yields an amorphous silicate with PEO and/or PPO anchored to the silica surface. The PEO/PPO phases are to be considered comparable to anchored solvents, where the anchoring of the solvent is somewhat analogous to the use of bonded phase columns in gas chromatography in place of simple, physically adsorbed phases. Therefore, active MMO biomimetic complexes, such as *in situ* formed $[Fe_2O(\eta^1-H_2O)(\eta^1-OAc)(TPA)_2]^{3+}$, **1**, TPA = tris[(2-pyridyl)methyl]amine), from the $[Fe_2O(\mu-OAc)(TPA)_2]^{3+}$ analog, **2**, at pH = 4.2, can then be embedded into the PEO and PPO tethered silica (Figure 1). Thus, the placement of the precatalyst into the anchored solvents allows one to potentially functionalize alkanes in aqueous solution with *t*-butyl hydroperoxide (TBHP) in the presence of oxygen gas (O_2) and, in this paper, we compare this former MMO model enzyme system to the latter mentioned technique, where the precatalyst, alkane, and oxidants were dissolved within the hydrophobic layers of the aqueous micelle dispersions (Figure 2).[1]
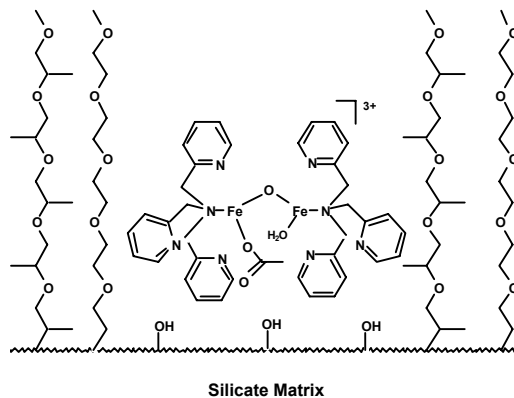

Silicate Matrix

Figure 1: A schematic representation of *in situ* formed $[Fe_2O(\eta^1-H_2O)(\eta^1-OAc)(TPA)_2]^{3+}$, **1**, embedded in the PEO, PPO derivatized silica, for alkane functionalization in water at pH 4.2.
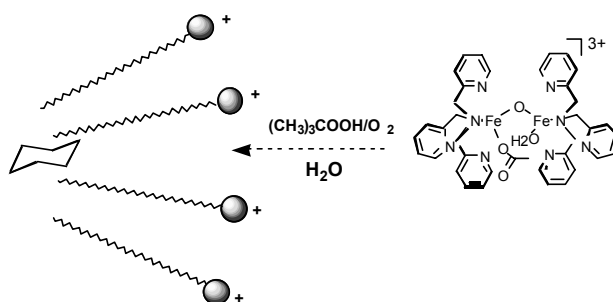

Figure 2: A schematic representation of *in situ* formed **1** diffusing, along with the oxidants, TBHP/O_2, into aqueous micelles formed with the surfactant, cetyltrimethylammonium hydrogensulfate, for alkane functionalization in water at pH 4.2.

Results and Discussion

Alkane Functionalization Studies with Surface Derivatized Silicates

As an initial example of alkane functionalization using various surface derivatized silicates, the oxidation of cyclooctane was carried out with *in situ* formed (pH = 4.2) $[Fe_2O((\eta^1-H_2O)(\eta^1-OAc)(TPA)_2]^{3+}$, **1**, as the precatalyst, in the presence of TBHP/O_2. From the results presented in Table 1, one can clearly observe that silicates with both hydrophobic PPO and hydrophilic PEO tethers provided a significantly improved reaction medium, compared to either PEO or PPO alone, with ~140 turnovers (TON, mmol of product/mmol of catalyst) being observed with 10 mol% PPO and 10 mol% PEO–SiO_2, while approximately 25 TON were observed with PPO–SiO_2 or PEO–SiO_2. It is interesting to note that $Fe(ClO_4)_3$ showed no alkane functionalization activity when impregnated in 10 mol% PPO and 10 mol% PEO–SiO_2, which indicates that the TPA ligands might be necessary for solubilization in the anchored polyether solvents, and therefore, for catalysis to occur.

The reaction selectivity also differed as a function of the silicate support. For example, with PPO–SiO$_2$ or PEO–SiO$_2$, the major product was cyclooctanone and the minor product was cyclooctene, formed consistently in a ratio of ~1.2:1. Futhermore, very minor amounts (<5%) of cyclooctanol and the mixed dialkylperoxide, cyclooctyl-$t$butylperoxide, were also formed. For 10 mol% PPO and 10 mol% PEO–SiO$_2$, about 25% of the products formed was the dehydrogenated cyclooctene, while the remaining 75% of oxygenated products, cyclooctanol, cyclooctanone, and cyclooctyl-t-butylperoxide, were formed in approximately a 1:3:2 ratio. The reaction was carried out at pH = 4.2 and, as in previous studies, the solution turned colorless from its original yellow color with formation of the proposed [(TPA)Fe^{2+}(μ-OH)Fe^{3+}(TPA)] complex that designates a Haber-Weiss process in the decomposition of TBHP. This observation is further supportive of the Haber-Weiss process in that after the TBHP oxidant was completely decomposed, the yellow color returned.

Table 1. **Oxidation of Cyclooctane with Complex 1 Embedded in Surface Derivatized Silica.[a]**

Silica Support	Total TON (hr^{-1})	Products[b]
10% PEO–SiO$_2$	19 (6.3)	43%, 55%, 1%, 1%
20% PEO–SiO$_2$	25 (8.3)	42%, 56%, 1%, 1%
10% PPO,10% PEO–SiO$_2$	142 (47.3)	26%, 35%, 13%, 25%
10% PPO–SiO$_2$	24 (8.0)	40%, 55%, 0%, 5%
20% PPO–SiO$_2$	21 (7.0)	37%, 49%, 0%, 4%
none	< 1	na

[a]Reactions were carried out by mixing 0.38 mmol cyclooctane, 3.8 mmol TBHP in 5 mL water at pH 4.2 and 0.38 µmol of *in situ* formed (as 1% wt. [Fe$_2$O((η^1-H$_2$O)(η^1-OAc)(TPA)$_2$]$^{3+}$ on derivatized silica) for 3 h at room temperature. [b]Mol% total products for cyclooctene, cyclooctanone, cyclooctanol, and cyclooctyl-t-butyl peroxide, respectively. Yields based on TBHP were 80-90%.

Thus, it is clearly evident that alkane functionalization reactions with TBHP/O$_2$ as oxidants, and in the presence of MMO biomimetic complexes, such as **1**, as well as other metal complexes, are initiated by formation of t-BuO• and t-BuOO• radicals.[1] In this case, by invoking the Haber-Weiss mechanism, the intermediate cyclooctyl radical can react with either dioxygen leading to the formation of cyclooctanone and cyclooctanol, via the proposed cyclooctyl hydroperoxide, or with a t-BuO• radical to form the mixed dialkyl peroxide. Interestingly, and uniquely for cyclooctane, cyclooctene was formed as a significant product, plausibly by an intramolecular oxidative dehydrogenation pathway from the cyclooctyl radical. Moreover, cyclooctene is *not* formed by dehydration of cyclooctanol as its use as a substrate, under typical reaction conditions, yielded no cyclooctene, but was converted to cyclooctanone.

The scope of the alkane functionalization reaction in aqueous solution with TBHP/O$_2$ and complex **1** in 10 mol% PPO and 10 mol% PEO–SiO$_2$ was extended to additional substrates (Table 2). For cycloalkanes, it was found that the activity sequence was: cyclohexane > cycloheptane ~ cyclooctane. However, in contrast to the reaction with cyclooctane, no alkene dehydrogenation products were observed, but the product ratios, ketone:alcohol:dialkyl peroxide, were similar. Alkyl aromatic compounds were also oxidized to benzylic ketones and alcohols.

Furthermore, a representative linear alkane, nonane, yielded ketones and secondary alcohols in a 2:1 ratio (Table 2).

Table 2. **The Oxidation of Alkanes with 1% wt. Complex 1, 10 % PPO, 10% PEO–SiO$_2$.[a]**

Substrates	Total TON	Products[b,c]	
cyclohexane	238	cyclohexanone	51%
		cyclohexanol	16%
		cyclohexyl-t-butyl peroxide	33%
cycloheptane	146	cycloheptanone	55%
		cycloheptanol	19%
		cycloheptyl-t-butyl peroxide	26%
tetrahydronaphthalene	141	α–tetralone	94%
		α–tetralol	6%
ethylbenzene	157	acetophenone	72%
		1-phenylethanol	28%
n-nonane	31	2-, 3-, 4-nonanone	68%
		2-, 3-, 4-nonanol	32%

a) Reactions were carried out by mixing 0.38 mmol alkane, 3.8 mmol TBHP in 5 mL water at pH 4.2 with 0.38 µmol precatalyst (as 1% wt. **1** on 10% PPO, 10% PEO–SiO$_2$) for 3 h at room temeperature. b) products as mol% total products. c) Yields based on TBHP were 80-90%.

Alkane Functionalization Studies with Aqueous Micelles

We chose cetyltrimethylammonium hydrogensulfate (CTAHS) to create micelles for the oxidation of cyclohexane with TBHP/O$_2$ in aqueous solution with precatalyst, [Fe$_2$O((η^1-H$_2$O)((η^1-OAc)(BPIA)$_2$]$^{3+}$, **3**, (BPIA = bis[(2-pyridyl)methyl][2-(1-methylimidazolyl)methyl]amine) (Figure 2). The results show that as the concentration of cyclohexane and TBHP were varied, a dependence on the TON of the products for each reactant was observed with catalyst **3**. We also observe that an increase in the cyclohexane concentration from 150 to 750 mmols concomitantly increases the amount of oxidation products from 11 TON to 32 TON and, more importantly, an increase in the CyOH/CyONE ratio from 0.47 to 0.82. By halving the amount of TBHP, we observe a decrease in the amount of oxidation products by a factor ~1.8, while the CyOH/CyONE ratio does not change. *These overall results strongly suggest that the cyclohexane oxidation occurs within the micelles.* We also evaluated other substrates, such as toluene (500 mmol) and octanol (500 mmol), in our aqueous micelle system, under similar conditions. We found that toluene provided only benzyl alcohol and benzaldehyde in a ratio of 1.5 with a total TON of 7, while octanol provided only octanal with a total TON of 3. It is intertesting to note, in the latter result, that in the absence of the surfactant (CTAHS) that ~ 1 TON was observed..

In conclusion, we have demonstrated the first example of the functionalization of hydrocarbon substrates with MMO biomimetic complexes embedded in a derivatized surface silica system and compared this synthesized macroenvironment with an aqueous micelle system using TBHP/O$_2$ as the oxidants. These free radical, alkane functionalization reactions were presumably initiated by the favorable redox chemistry of complexes **1** and **3** in both of the above-mentioned macroenvironments that provided t-BuO• and t-BuOO• radicals (Haber-Weiss process).

Reference
Neimann, K.; Neumann, R.; Rabion, A.; Buchanan, R. M.; Fish, R. H. *Inorg. Chem.* **1999**, *38*, 3575 and references therein**.**

SINGLE-CRYSTAL NEUTRON DIFFRACTION: A VALUABLE TOOL FOR PROBING BOND ACTIVATION IN σ COMPLEXES

Thomas F. Koetzle and Arthur J. Schultz

IPNS Division
Argonne National Laboratory
Argonne, IL 60439

Introduction

Neutron diffraction has the unique capacity to provide precise hydrogen atom positions in crystalline solids. For more than 20 years, this capability has been exploited in a series of single-crystal studies that shed light on bond activation in σ complexes. Topics investigated include H–H activation in molecular hydrogen complexes,[1] C–H activation in agostic systems[2] and, most recently, B–H activation in a catecholborane metal complex.[3] This paper illustrates some of these results, drawing upon studies carried out using both steady-state monochromatic beam and pulsed time-of-flight Laue diffraction techniques.

Despite its noteworthy successes including those that we illustrate here, single-crystal neutron diffraction generally has seen limited application to date due to the need for very large crystals. Revolutionary improvements are anticipated with the advent of a new generation of sources now under construction or in the planning stage, including the Spallation Neutron Source (SNS) that is scheduled to become operational at Oak Ridge in 2006. Some speculations will be offered on the exciting possibilities envisioned for the single-crystal diffractometer (SCD) that is being planned for SNS.[4]

Experimental

Large, well-formed crystals of the compounds under investigation were mounted on an SCD instrument at the High Flux Beam Reactor[5] (HFBR) at Brookhaven National Laboratory or at the Intense Pulsed Neutron Source (IPNS) at Argonne National Laboratory. The samples were generally cooled to temperatures of 100 K or below for intensity data collection using a closed-cycle helium refrigerator. At HFBR, measurements were carried out sequentially with a steady-state monochromatic beam technique and a neutron wavelength near 1 Å, employing a point detector. Measurements at IPNS utilize a white beam time-of-flight Laue technique with a time- and position-sensitive detector[6] to sample many reflections in parallel (see **Figure 1** for a schematic view of IPNS SCD). These single-crystal neutron diffraction experiments can require a considerable amount of beam time. For example the catecholborane complex mentioned above, which is triclinic and has a unit-cell volume of 642 Å^3, required 14 d for intensity measurement on IPNS SCD using a 4 mm^3 single crystal. Data collection times for our experiments at HFBR were generally similar.

Neutron intensity data were corrected for background, for the Lorenz effect, and for absorption. Time-of-flight data from IPNS were also corrected for the incident neutron spectrum and for the wavelength-dependent detector efficiency. Extinction corrections were included in the least-squares structure refinements, as required.

Results and Discussion

Molecular Hydrogen (η-H$_2$) Complexes. The discovery by Kubas in 1984 that transition metals can bind molecular hydrogen forming η-H$_2$ complexes, also termed "non-classical hydrides," has opened a new field of investigation and has allowed some earlier reaction mechanisms or reactivity patterns to be more precisely
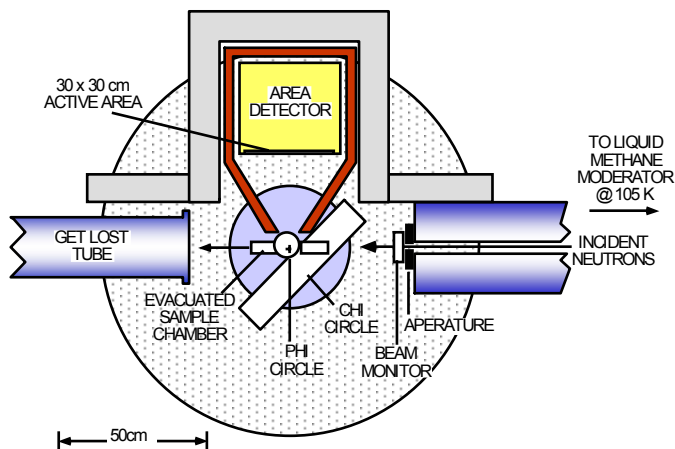

Figure 1. Schematic view of IPNS SCD instrument.

defined or even reconsidered.[7] The crucial step in the hydrogenation reaction path is the coordination to the metal center of an H$_2$ molecule and its activation via the formation of a non-classical η-H$_2$ complex, with the subsequent cleavage of the H–H bond (oxidative addition) leading to a classical M(H)$_2$ hydrido complex (**Figure 2**).
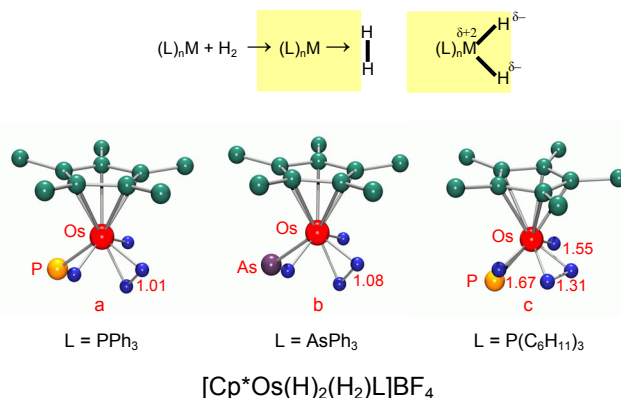

Figure 2. Molecular structures of three cationic osmium molecular hydrogen complexes. The phenyl and cyclohexyl groups bound to phosphorus and arsenic, and the methyl group hydrogens on the pentamethylcyclopentadienyl ligand, are not shown for clarity.

A detailed knowledge of the metal-hydrogen bonding interaction is essential for a better understanding of these reactions. To this end, single-crystal neutron diffraction studies of (H$_2$) complexes at low temperatures (< 25 K) have established that the H–H separation can cover a wide range of distances, from ~ 0.8 Å (strong H–H bond) to ~1.4 Å (weak H–H bond), thus neatly spanning the oxidative addition pathway and giving support to the mechanistic studies of this most important reaction. Single-crystal neutron diffraction provided the first unambiguous experimental proof of the existence of the so-called "stretched" (i.e., activated) H–H bonds (>1.0 Å).[1,7] Recently a series of cationic osmium complexes (see **Figure 2**) containing

hydrides and dihydrogen in varying degrees of activation has been studied.[8] The reason for the rotation and activation of the H_2 ligand is not completely clear from just these three structures. In order to understand the relative contributions of electronic and steric properties of the ancillary ligands, a question still open to discussion, the series needs to be expanded to include other ligands such as trimethylphosphine. To date, it has not been possible to produce suitably large crystals for neutron diffraction. In the future we hope to be able to tackle this problem at SNS using 0.1 mm^3 crystals, which are readily available, and to use the experimentally observed trends as a check of high-level quantum mechanical calculations.
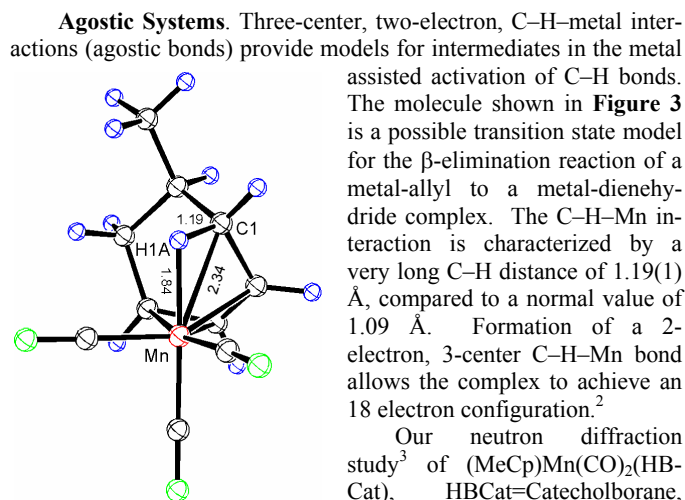
Agostic Systems. Three-center, two-electron, C–H–metal interactions (agostic bonds) provide models for intermediates in the metal assisted activation of C–H bonds.

Figure 3. Molecular structure of $(C_7H_{11})Mn(CO)_3$.

The molecule shown in **Figure 3** is a possible transition state model for the β-elimination reaction of a metal-allyl to a metal-dienehydride complex. The C–H–Mn interaction is characterized by a very long C–H distance of 1.19(1) Å, compared to a normal value of 1.09 Å. Formation of a 2-electron, 3-center C–H–Mn bond allows the complex to achieve an 18 electron configuration.[2]

Our neutron diffraction study[3] of $(MeCp)Mn(CO)_2(HB-Cat)$, HBCat=Catecholborane, illustrated in **Figure 4** below, indicates that this σ-borane possesses an extremely elongated B–H bond (1.384(6) Å). This type of highly activated σ-complex is expected to be typical of reaction intermediates that precede oxidative addition of substrates in catalytic hydroborations. The molecular geometry found here features a lateral configuration of the borane (Mn–H–B = 88.8(3)°) and a four-legged piano-stool arrangement with OC–Mn–CO = 90.7(2)°.
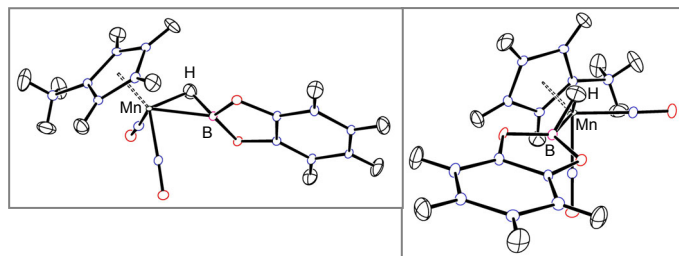

Figure 4. Structure of $(MeCp)Mn(CO)_2(HBCat)$, HBCat= Catecholborane, viewed approximately normal to the Mn–H–B plane (left) and perpendicular to this plane (right).

Future Developments. As we have noted above, revolutionary advancements are anticipated with the advent of a new generation of neutron sources now under construction or in the planning stage. These include the SNS at Oak Ridge, which will generate approximately two orders of magnitude more neutron flux than is now available at IPNS (see **Figure 5**). The SCD instrument planned for SNS[4] will include an extensive area detector array and will be optimized for rapid data collection on moderate size unit cells with up to ca. 50 Å axial repeats. A major objective is to be able to study small, 0.1 mm^3, samples approaching the size that are routinely used

in many laboratories for single-crystal X-ray studies. A schematic layout of the instrument conceptual design is shown in **Figure 6**.

In order to maximize scientific impact, SNS SCD includes provision for magnetic scattering experiments, using polarized neutron beams to study unpaired electron distributions, and for diffuse scattering measurements to attack problems involving short-range order. *By greatly expanding the range of materials that can be explored, SNS SCD is expected to revolutionize single-crystal neutron diffraction as we know it, especially from the viewpoint of the practicing synthetic chemist.*
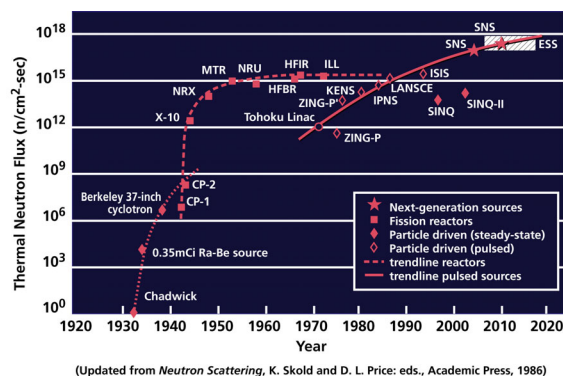

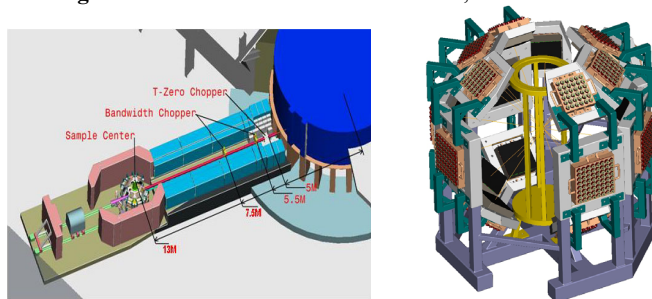**Figure 5**. Flux increase at neutron sources, 1930 - .

Figure 6. Conceptual design of SNS SCD with the beam line layout (left), and a detail of the sample enclosure and detector array (right). Top access is provided for mounting auxiliary equipment, including cryostats and magnets.

References
(1) Koetzle, T. F. *Trans. Am. Crystallogr. Assoc.* **1995**, *31*, 57-68.
(2) Schultz, A. J.; Teller, R. G.; Beno, M. A.; Williams, J. M.; Brookhart, M.; Lamana, W.; Humphrey, M. B. *Science* **1983**, *220*, 197-199.
(3) Koetzle, T. F.; Schultz, A. J.; Wang, X. P.; Hartwig, J. F.; Schlecht, S.; Albinati, A. *Am. Crystallogr. Assoc. Meeting Abstracts, Los Angeles, CA,* 2001.
(4) Hoffmann, C. *Conceptual Design for a Single Crystal Diffractometer at SNS*, 2002.
(5) The HFBR facility was permanently shut down in 1999.
(6) Schultz, A. J. *Trans. Am. Crystallogr. Assoc.* **1993**, *29*, 29-41.
(7) Kubas, G. J. *Metal Dihydrogen and σ-Bond Complexes*, Kluwer Academic: Dordrecht, 2001.
(8) Gross, G. L.; Young, D. M.; Schultz, A. J.; Girolami, G. S. *J. Chem. Soc., Dalton Trans.* **1997**, *18*, 3081-3082.

METHANOL AND HYDROGEN FROM METHANE, WATER, AND LIGHT

Charles E. Taylor

U.S. Department of Energy
National Energy Technology Laboratory
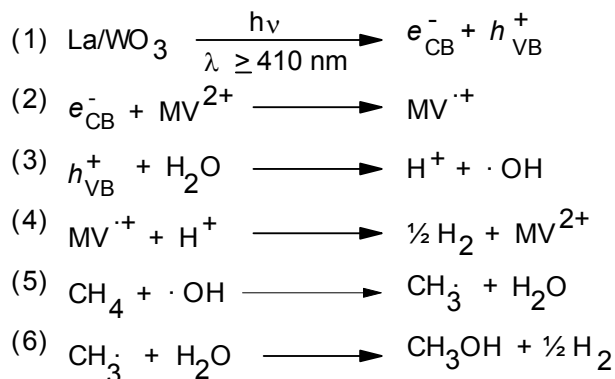P.O. Box 10940
Pittsburgh, PA 15236-0940

Introduction

Research on the conversion of natural gas (methane) has been an ongoing effort at the National Energy Technology Laboratory (NETL) for over 20 years. A long-term goal of our research team is to explore novel pathways for the direct conversion of methane to liquid fuels, chemicals, and intermediates.

Literature reports have indicated that photochemical oxidation of methane may be a commercially feasible route to methanol [1, 2]. In these studies, methane, water and light are reacted at moderate temperatures and pressures.

Research in our laboratory [3] has shown that, methane, dissolved in water, at temperatures > 70 °C, with a semiconductor catalyst, can be converted to methanol and hydrogen. The use of three relatively abundant and inexpensive reactants - light, water, and methane - to produce methanol is an attractive process option. The main advantage of using a photocatalyst to promote the photoconversion of methane to methanol is that the presence of the catalyst, in conjunction with an electron transfer agent, allows reaction to occur with visible light instead of with ultraviolet. This greatly simplifies reactor design and will permit flexibility in the selection of the light source. The products of the reaction of interest, methanol and hydrogen, are both commercially desirable as fuels or chemical intermediates. The limiting factor for conversion of methane appears to be the solubility of methane in water. We hypothesized that if the concentration of methane in water can be increased, conversion should also increase. Methane hydrates might provide a method of increasing the amount of methane dissolved in water, because at standard temperature and pressure (STP), one volume of saturated methane hydrates contains approximately 180 volumes of methane.

Methane hydrates were first observed in the laboratory in 1810. It wasn't until nearly 150 years later that they were observed in nature. Hydrates can occur in permafrost, in sediment where gas exists under moderate to high pressure and low temperatures, and offshore beneath deep water. Hydrates are a problem in the oil and gas production industry because they can form in the well or pipelines, thereby blocking the flow of fuel. Estimates by the U.S. Geological Survey project that world hydrate deposits contain approximately 2×10^4 trillion cubic meters of methane [4]. Estimates of methane hydrate deposits off the coast of the United States is approximately 9×10^3 trillion cubic meters of methane with an additional 17 trillion cubic meters of methane in the permafrost on the north slope of Alaska [1].

Our vision is to immobilize methane and water in close proximity by formation of the methane hydrate. The reaction will involve the formation of hydroxyl radical (•OH) within the methane hydrate by photochemical means. The proximity and restricted mobility of the •OH and the CH_4 would then favor the formation of CH_3OH. Successful demonstration of this principle would then open the possibility of using hydrates to immobilize reactants in a way that favors the desired selectivity. This is the basis of our Patent [5].

$$(1) \quad La/WO_3 \xrightarrow[\lambda \geq 410\ nm]{h\nu} e^-_{CB} + h^+_{VB}$$

$$(2) \quad e^-_{CB} + MV^{2+} \longrightarrow MV^{\cdot+}$$

$$(3) \quad h^+_{VB} + H_2O \longrightarrow H^+ + \cdot OH$$

$$(4) \quad MV^{\cdot+} + H^+ \longrightarrow \tfrac{1}{2} H_2 + MV^{2+}$$

$$(5) \quad CH_4 + \cdot OH \longrightarrow CH_3^{\cdot} + H_2O$$

$$(6) \quad CH_3^{\cdot} + H_2O \longrightarrow CH_3OH + \tfrac{1}{2} H_2$$

e^-_{CB} = electron in conduction band, h^+_{VB} = positive hole in valance band

Scheme 1: Proposed pathway for the photocatalytic conversion of methane and water

EXPERIMENTAL

The tungsten oxide semiconductor photocatalysts were synthesized following a modification of the procedure in the literature [6]. Four dopants, copper, lanthanum, platinum, and a mixture of copper and lanthanum, were selected for study on the tungsten oxide catalyst base. The titania photocatalyst used in this study is a proprietary sol-gel TiO_2 catalyst obtained from Attia Corporation.

The 1.0 MPa, a commercially supplied 1-liter quartz photochemical reaction vessel, was fitted to meet the needs of this research. This included use of a Teflon-coated magnetic stirring bar in the reactor, a fritted glass sparger, a nitrogen line used to cool the UV lamp, and an injection port.

In a typical 1.00 MPa pressure experiment, the sintered catalyst is suspended, by mechanical stirring, in double-distilled water (~750 mL) containing an electron-transfer reagent, methyl viologen dichloride. A mixture of methane (5 mL/min) and helium (16 mL/min) is sparged through the photocatalytic reactor. The helium is an internal standard for on-line analysis of the reactor effluent. The reaction temperature is maintained at ~371 K by circulation of heated (~393 K) silicone oil in the outer jacket of the reactor. A high-pressure mercury-vapor quartz lamp is used as the light source.

All pressurized and hydrate reactions were conducted in a high-pressure view cell. The cell is constructed of 316 stainless steel 6.35 cm (2.5 inches) OD and 27.4 cm (11 inches) in length. The internal volume of the cell is ~ 40 mL. The cell is fitted with 2 machined endcaps, one which contains a sapphire window to allow for observation of the contents of the cell using a CCD camera. The cell is fitted with ports to accommodate the fill gas inlet and reaction product outlet, a pressure transducer to monitor the internal pressure of the gas inside the cell, and a thermocouple that terminates inside the cavity of the cell to monitor the temperature of the liquid/hydrate mixture. While the working pressure of the cell is rated at 220 MPa (32,000 psia), all experiments were conducted at 13.8 MPa (2000 psig) or less. The temperature of the cell is controlled by the flow of a glycol/water solution from an external circulating temperature bath through a coil of 0.64 cm (¼ inch) copper tubing that is wrapped around the outside of the cell. Several layers of insulating material are wrapped around the cell to help maintain constant temperature.

A typical experiment involves filling the cell with 40 mL of double-distilled water. A Teflon® coated stir bar is added, followed by portions of the photocatalyst. The endcap is placed on the cell and tightened to specifications. An external magnetic stirrer is used to obtain a high degree of vortex mixing inside the cell. The cell is connected to the gas manifold and purged several times with

methane. Following the purge procedure, the cell is charged with methane at pressures of 5.5 – 13.8 MPa (800-2000 psig). Using the external circulating temperature bath, the temperature of the water in the cell is lowered until formation of the methane hydrate is observed. After formation of the hydrate, the temperature of the cell is lowered to -5 °C and held constant. Illumination of the hydrate is then performed using a high-pressure 350-watt mercury-vapor lamp, with the light directed toward the sapphire window. After illumination for a set period of time, the cell is allowed to warm slowly to room temperature. When the cell and its contents have reached room temperature, the contents of the cell are vented and a gas chromatograph and/or a mass spectrometer are used to analyze the products.

RESULTS

Of the four-tungsten oxide (doped with platinum, lanthanum, copper, and a 50/50 molar mixture of copper and lanthanum) and the sol-gel titania catalysts studied, the tungsten oxide catalyst doped with lanthanum exhibited the largest methane conversion and methanol yield. This catalyst was the one chosen for use in this study (Figure 1).
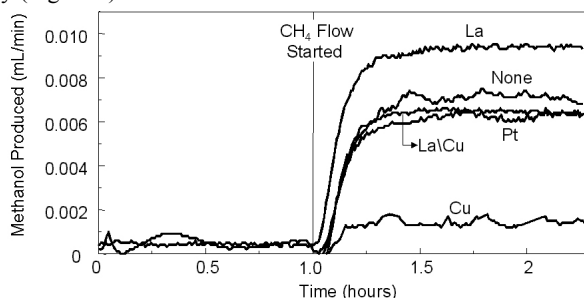

Figure 1. Methanol production with various promoted tungsten oxide photocatalysts.

Figure 2 shows the results of a typical photocatalytic methane conversion experiment at 1.0 MPa. Methane conversions are ~4% with hydrogen and methanol as the main products of reaction. Note that after the UV lamp is turned off, the detected flow of methanol decreases slowly to zero (over ~2 hours). It was hypothesized that this behavior was due to stripping of methanol from the water in the reactor by the reactant gases. To confirm this, methanol was injected into the reactor, previously filled with 750 mL water at the operating temperature, and the concentration of methanol in the gas flow from the reactor was measured as a function of time. A decrease in methanol concentration over several hours, similar to that observed in experiments undergoing methane photoconversion, was observed.

As noted previously, the proposed reaction sequence of interest initially produces hydroxyl radical, which then reacts with methane to produce methanol. To test the validity of this hypothesis, a 30% solution of hydrogen peroxide, a good source of hydroxyl radicals, was injected into the reactor during photocatalytic methane conversion. After peroxide injection, conversion of methane increases from ~4% to ~10%, methanol production increases 17 fold, and carbon dioxide increases 5 fold, along with modest increases in hydrogen and carbon monoxide. A drop in methane conversion to zero for approximately 12 min after injection of the hydrogen peroxide solution was observed in all experiments. This drop in methane conversion can be explained by assuming that prior to injecting hydrogen peroxide solution; a steady-state condition existed between the methane dissolving in the water and methane being consumed. It is likely that the introduction of excess hydroxyl radicals depleted the dissolved methane. At the temperature where the reactions were conducted, the solubility of methane in water is

very low (0.017 ml of methane per ml of water [7]). This low solubility results in little methane available for conversion until steady-state conditions could be re-established.
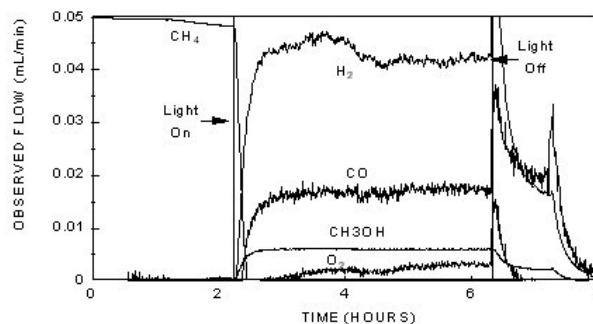

Figure 2. Products of the photocatalytic conversion of methane in water at 1.00 MPa and 370 K.

Note that in Figure 2, after the UV lamp is turned off, the detected flow of methanol decreases slowly to zero (over ~2 h). This is due to stripping of dissolved methanol from the water in the reactor by the reactant gases. Gas chromatographic analysis of the liquid product that had condensed in the trap at 273 K revealed the presence of methanol and acetic acid. Further analysis to identify other components by GC-MS was not possible due to the low concentration of products in the trap. The products were diluted by water carried over from the reactor in the flow of helium that is used as an internal standard.

The tungsten oxide photocatalyst is reported to function at wavelengths >410 nm. All results reported above were obtained using the UV lamp's total spectrum output In order to separate reactions initiated by radiation with UV light from reactions initiated by visible light, a filter was constructed to block the UV portion of the lamp's energy output. The filter, a Pyrex ® sleeve fitted around the lamp, absorbs nearly all radiation below ~310 nm. The total energy output of the lamp with the filter in-stalled is ~50% of that without the filter. Experiments using the filter around the lamp were conducted under conditions described above. The results of experiments conducted with the UV filter installed gave similar conversions and product selectivities as those observed using the full spectrum of the lamp (Figure 3).

Photocatalytic conversion of methane and water at 10.1 MPa produced a product slate similar to that obtained at atmospheric pressure. What is of note is that while no conversion of methane was observed for the experiments conducted at atmospheric pressure at temperatures less than 343 K, at 10.1 MPa conversion occurred at 323 K.

The majority of the photocatalytic research, including the photocatalytic conversion of methane in methane hydrates, was performed with the lanthanum-promoted tungsten oxide photocatalyst. Figure 3 shows the results of photocatalytic conversion of methane dissolved in water at atmospheric pressure and 97°C for various dopants. As is shown, the catalyst doped with lanthanum out performs the other doped catalyst for the production of methanol.

Photocatalytic conversion of the methane contained within the methane hydrate molecule produced results similar to the two previously described experiments; methanol and hydrogen were the main products. This is an interesting result as at atmospheric pressure, no photocatalytic conversion of methane dissolved in water is observed at temperatures below 70°C. The photocatalytic conversions of the methane hydrate occurred at temperatures of –5°C and below.
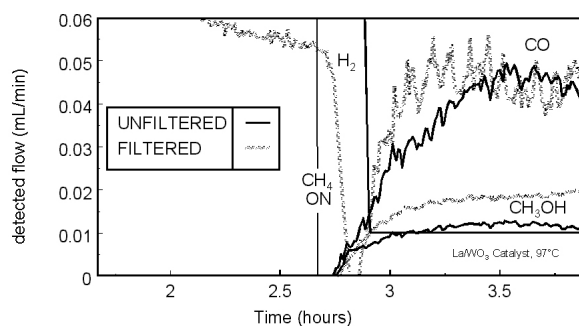
Figure 3. Products of the photocatalytic reaction of methane dissolved in water at atmospheric pressure and 97°C with full spectrum and filtered (visible) light.

Analysis, by mass spectrometry (Figure 4), of the gas contained in the headspace of the cell after illumination revealed the presence of methanol, hydrogen, ethane, oxygen, formic acid, and carbon dioxide. The formation of methanol and hydrogen are the primary products of reaction. The other products observed are formed by side reactions. Photocatalytic splitting of water (a side reaction not shown but observed in our laboratory when using this catalyst) forms oxygen. Ethane is formed by the combination of two methyl radicals (produced in Equation 5), and the formic acid and carbon dioxide are the result of further reactions of methanol.

The results of photocatalytic conversion of methane contained within methane hydrates with a sol-gel titanium dioxide photocatalyst are similar to the tungsten oxide photocatalyst with the exception that while methanol and hydrogen are produced by the reaction, oxygen is the main product of the titanium sol-gel photocatalyst.
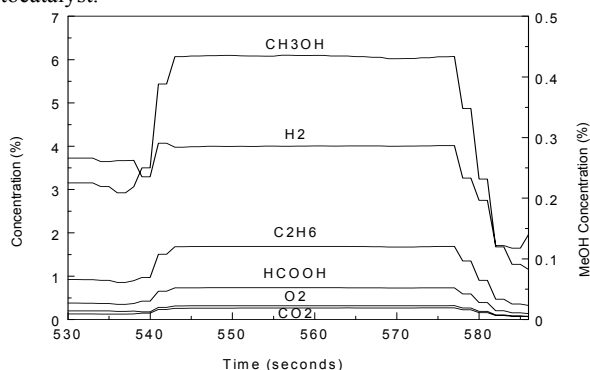

Figure 4. Products of the photocatalytic conversion of methane in methane hydrate with lanthanum-promoted tungsten oxide photocatalyst.

CONCLUSIONS

By use of a photocatalyst and electron-transfer reagent, we have been able to convert methane and water to methanol and hydrogen. Products of conversion at atmospheric pressure and 10.1 MPa were similar. While photoconversion of methane and water to methanol and hydrogen did not occur below 343 K at 1.0 MPa, conversion was observed at 323 K at 10.1 MPa and at temperatures as low as 258 K in methane hydrates. We also observe several side reactions of methane conversion in all instances, the production of ethane, oxygen, formic acid and carbon dioxide.

Under the conditions used in the 1 MPa experiments, the photocatalytic reaction produced 1.7 g of methanol-per gram of catalyst-per hour in the steady-state mode and produced 43 g of methanol-per gram of catalyst-per hour when hydrogen peroxide solution was added.

The use of a filter removed the UV component from the lamp. Experimental results show that little difference between the filtered and unfiltered lamp was observed in the case of the platinum-doped tungsten oxide sample. This indicates that the photocatalyst is operating using visible light, the UV portion of the lamp's output is negligible in the photocatalytic con-version of methane to methanol, and that a limiting factor in conversion may be the solubility of methane in water.

In all experiments, conversion of methane and the production of methanol are augmented by the addition of hydrogen peroxide solution, consistent with the postulated mechanism that invokes a hydroxyl radical as an intermediate in the reaction sequence. The use of other radical initiators would be of interest to deter-mine if the enhanced conversion could be sustained.

After the hydrate had formed and the pressure in the cell equilibrated, the UV lamp was turned on to initiate the photocatalytic conversion process. During illumination, a decrease in the pressure of the cell is observed. Following illumination, the cell was maintained at -2°C for several hours before warming to room temperature. Also of note is that the final pressure of methane is less than the starting methane pressure due to conversion of the methane within the hydrate.

Mass spectrometric analysis of the gas vented from the cell after illumination revealed the presence of methanol, hydrogen, ethane, oxygen, formic acid, and carbon dioxide, as shown in Figure 4. Side reactions that occur during the photocatalytic conversion process are responsible for producing these additional species. Photocatalytic splitting of water forms oxygen, ethane is formed by the combination of two methyl radicals, and the formic acid and carbon dioxide are the result of further reactions of methanol.

Attempts to use GC to identify products dissolved in the water after reaction were of limited value. In an effort to detect these products dissolved in the water, the cell and its contents were heated to 70°C prior to venting. Analysis of the gas headspace resulted in the detection of similar products as those obtained at room temperature. If products dissolved in the water were present, their concentration was too low to be detected with our setup. We are currently refining our detection system to correct this problem.

Experiments were also performed where the double-distilled water was replaced with simulated seawater. The results of these experiments were similar to those performed with double-distilled water.

DISCLAIMER. Reference in this report to any specific commercial product, process, or service is to facilitate understanding and does not necessarily imply its endorsement or favoring by the United States Department of Energy.

REFERENCES

(1) Ashokkumar, M. and Maruthamuthu, P. *J. Mat. Sci. Le*tt.**1988**, 24, 2135-39.
(2) Ogura, K. and Kataoka, M. *J. Mol. Cat.* **1988**, 43, 371-79.
(3) Noceti, R.P. and Taylor, C.E. U.S. Patent 5,720,858 **February 24, 1998**.
(4) Collett, T.S. and Kuuskraa, V.A. *Oil and Gas J.* **May 11, 1998**, 90.
(5) Taylor, C.E., Noceti, R.P., and Bockrath, B.C. U.S. Patent *6,267,849* **July 31, 2001**.
(6) P. Maruthamuthu, M. Ashokkumar, Int. J. Hydrogen Energy 14(4) (1989) 275.
(7) J.A. Dean (Ed.), Lange's Handbook of Chemistry, 13th Ed., 1985, p. 10-5.

NEUTRON REFLECTIVITY STUDIES OF THE GAS/SOLID/LIQUID INTERFACE

Miriam Rafailovich, Tadanori Koga, Young Soo Seo, Devinder Mahajan, Jonathan Sokolov

Department of Materials Science and Engineering, Stony Brook University, Stony Brook, NY 11794 USA

Benjamin Chu
Department of Chemistry, Stony Brook University, Stony Brook, NY 11794 USA

Sushil Satija
NIST, Gaithersburg, MD 20879 USA

Introduction

Polymer films form convenient matrices catalysis. In particular when highly reactive Fe or Co nanoparticles are encapsulated in polymer films the polymer can serve both as mechanical support as well as protective coating against fouling. On the other hand, since many of the reactions are gas phase, the same protective properties inhibit flow of the reactants and reduce the efficiency of the catalyst. Recently, using neutron reflectivity (NR), it has been demonstrated that $scCO_2$ may serve as a "universal solvent" near polymer surfaces and in thin films within a narrow temperature and pressure regime, known as the "density fluctuation ridge"[1,2]. Even thin films of glassy polymers, such as polystyrene (PS) and poly(methyl methacrylate), the films were observed to swell up to 40 % along the ridge near the critical temperature of CO_2 (T_c=31.3 ºC),[3] at temperature well below their glass transition temperatures ($T_g \sim 100$ ºC), while the bulk swelling was less than 10 %. In addition, we found that the effect could be frozen by a flash evaporation of CO_2 via the polymer vitrification process[4] without the formation of voids[5,6] as previously reported in the bulk.[7,8] Since CO_2 is a "green solvent" which does not react with many of the catalytic particle inclusions, one can in principal use this process to produce polymer films with high throughput for the reactants which also provide a protective support for the catalyst. Here we will report on the physical properties of theses films, such as density and melting and explore the effects of nanoparticle additions on the interactions between the polymer and CO_2.

Experimental

The films qualities were investigated by using x-ray reflectivity (XR), where the XR is more sensitive than NR to concentration profiles over small distances, and spectroscopic ellipsometry. Samples used in this study were two kinds of hydrogenated PS (PS1:M_w=2.0×10^5, PS2:M_w=6.5×10^5). Both polymers were obtained from Polymer Lab. and their polydispersity indices were 1.05. The thin films were spun cast on HF etched Si substrates and were pre-annealed for 5 hours in vacuum of 10^{-6} Torr at 150 °C. The films were first placed in the high-pressure chamber and immersed in $scCO_2$ at the ridge condition ($T = 36$ °C and $P = 8.2$ MPa) for an annealing time of 2 hours, and then quickly depressurized to atmospheric pressure within 10 sec. It should be noted that the surface remained flat even after the quick evaporation with the root-mean-square (rms) roughness ($\sigma = 6$Å) between the polymer/air interface, which is identical to that of the unswollen film.[5] The XR measurements have been carried out at the X10B beamline of the National Synchrotron Light Source (NSLS), Brookhaven National Laboratory (BNL) using photon energy of 11 keV. In order to obtain the density profile in the direction normal to the surface, we performed the Fourier transformation (FT) analysis for the XR data.[9] FT is powerful tool to analyze even a low x-ray contrast interface of multilayers. A H-VASE spectroscopic ellipsometry (J.A. Woollam Co., Inc.) was used to study the freezing samples with a wide spectral range of 300-800 nm with 10 nm increments. The angles of incidence for all the measurements were varied from 60 to 75º with 5º increments from the vertical.

Results and Discussion

Figure 1(a) shows the representative XR profile $I(q_z)$ for freezing PS1 (unswollen film thickness (L_0 = 110 Å), where the reflectivity is plotted as a function of the momentum transfer normal to the surface, $q_z = 4\pi \sin\theta / \lambda$ with θ being the glancing angle of incidence and λ, the x-ray wavelength, respectively. Figure 1 (b) shows the FT profile of XR data shown in Fig. 1(a), which is related to the corresponding one-dimensional Patterson function, i.e.,

$$F(d,q_1) = \left| \int_{q_1}^{q_2} q_z^4 I(q_z) \exp(iq_z d) dq_z \right|^2 \qquad (1)$$

where q_1 is the lower q limit, q_2 is the higher q limit and d is the film thickness. The q_1 value, which is sensitive to the shape of the FT, and the q_2 value, which is given by the q_z-range of the data, were set as q_1=0.053 Å^{-1} and q_2=1.0 Å^{-1}, respectively, for the integration in q_z-space. From the figure we can see two small peaks (shown by asterisks), which indicate an existence of two layers having different thickness and density in the film, and one large peak, which is equivalent to the total thickness of the freezing film (164 Å). It is noteworthy that no small peaks are seen in the unswollen film, i.e., the film is thoroughly homogenous, as previously discussed.[9] In order to refine these XR and FT data simultaneously, we used a four-layer model, i.e., silicon substrate, native oxide and two PS layers having the different densities. As shown in Fig. 1 (c), the best-fit result showed that the film was incorporating a constrained 30 Å layer at the Si interface having the bulk PS dispersion value δ of 1.92×10^{-6}) in the refractive index for x-ray[10] and an intermediate layer of 134 Å thickness with δ = 1.27×10^{-6} between air and the constraint layer. Surprisingly, the latter δ value corresponds to an approximately 35 % lower density than the bulk PS density. Hence, we can easily produce tailor-made lower density films as exposed to $scCO_2$ and subsequent quick evaporation.

Next, we shall focus on the optical index of refraction of the vitrified films, which is a density-dependent physical property, by using spectroscopic ellipsometry. The polymer used was PS2 in order to clarify whether the production of the lower-density layer was specific to the polymer. The sample preparation for the vitrified films was exactly same as that for the PS1 films. Fig. 2 shows the refractive indices of the mobile layers as a function of the unswollen thickness. From the figure we can clearly see that the indices of refraction for the mobile layers decreased with increasing S_f values over the wide wavelength range of 450-800 nm. It is noted that this trend is in good agreement with the previous report for PMMA-CO_2 mixtures using ellipsometry experiments.[18]

In conclusion, we found a novel method for producing stable low density and low index of refraction polymer films by using supercritical carbon dioxide. Furthermore, the density-fluctuation-induced swelling may be not specific to either the gas or the polymer

system. Experiments are currently in progress on polymer films containing Fe and Co nanoparticles. Since these particles provide high x-ray contrast, the XR reflectivity yields both the density of the film as well as the distribution of the particles within the films. We, therefore, are able to study the effects of nanoparticle size, concentration, and chemical nature on the on the interactions of supercritical solvents such as ethane and scCO$_2$ with polymer support films.

Acknowledgements

References

1. McHugh, M. A.; Krukonis, V. Supercritical Fluids Extraction Principles and Practice; Woburn, MA, 1994.
2. Koga, T.; Seo, Y.-S.; Zhang, Y.; Shin, K.; Kusano, K.; K., N.; Rafailovich, M. H.; Sokolov, J. C.; Chu, B.; Peiffer, D.; Occhiogrosso, R.; Satija, S. K. Phys. Rev. Lett. **2002**, 89, 125506.
3. Koga, T.; Seo, Y.; Shin, K.; Zhang, Y.; Rafailovich, M.; Sokolov, J.; Chu, B.; Peiffer, D.; Satija, S. K. Submitted to Macromolecules.
4. Koga, T.; Seo, Y.; Hu, X.; Kwanwoo, S.; Zhang, Y.; Rafailovich, M. H.; Sokolov, J. C.; Chu, B.; Satija, S. K. Europhys. Lett. in press.
5. Koga, T.; Shin, K.; Zhang, Y.; Seo, Y.-S.; Rafailovich, M. H.; Sokolov, J. C.; Chu, B.; Satija, S. K. J. Phys. Soc. Jpn, **2001**; 70, 347.
6. RamachandraRao, V. S.; Gupta, R. R.; Russell, T. P.; Watkins, J. J. Macromolecules **2001**, 34, 7923.
7. Arora, K. A.; Lesser, A. J.; McCarthy, T. J. Macromolecules **1998**, 31, 4614.
8. Stafford, C. M.; Russell, T. P.; McCarthy, T. J. Macromolecules **1999**, 32, 7610.
9. Seeck, O. H.; Kaendler, I. D.; Tolan, M.; Shin, K.; Rafailovich, M. H.; Sokolov, J. C.; Kolb, R. Appl. Phys. Lett. **2000**, 75, 2713.
10. δ is expressed by $\delta = r_e N_A /(2\pi) \rho \sum_i (Z_i / A_i)$ where r_e is the classical electron radius, N_A is Avogadro's number, ρ is the density, A_i and Z_i are atomic weight and atomic number of the element i.
11. DeMaggio, G. B.; Frieze, W. E.; Gidley, D. W.; Zhu, M.; Hristov, H. A.; Yee, A. F. Phys. Rev. Lett. **1997**, 78, 1524.
12. Polymer Handbook 4th Ed.; John Wiley & Sons, Inc.: NY, 1999.
13. S_f was calculated from the equation $S_f = (L-L_0)/(L_0-x)$, where L is the measured thickness of the swollen films and x is the thickness of the constrained layer, respectively.
14. The maximum thickness for four-layer model was approximately 650 Å for PS2. The difference between two PS could be due to the R_g scaled swelling behavior.
15. Koga, T. et al, manuscript in preparation.
16. Philipp, E. D., 1. In Handbook of Optical Constants of Solids; Palik, E. D., Ed,; Harcourt Brace Javanovich:Orland, 1985; Vol. 1.
17. Jellison, G. E. J. Appl. Phys. **1991**, 69, 7627.
18. Sirard, S. M.; J., Z. K.; Sanchez, I. C.; Green, P. F.; Johnston, K. P. Macromolecules **2002**, 35, 1928.
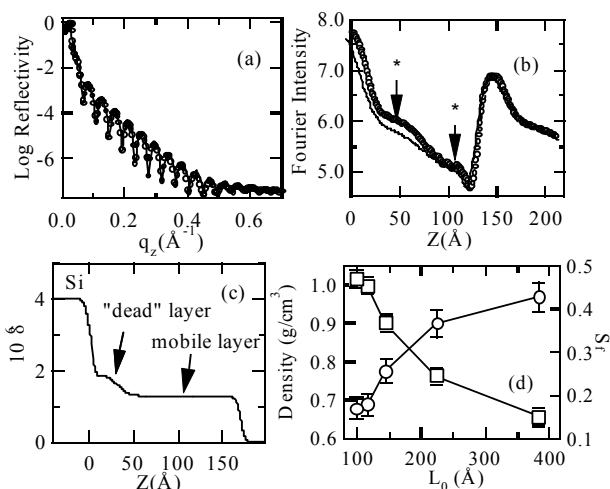
Figure 1. (a) Measured RF (symbols) and refinement (solid line) of the freezing PS1 (L$_0$=110 Å) film. (b) FT of measured (symbols) and calculated (solid) RFs. (c) Dispersion profile used for the refinement. (d) Thickness dependence of ρ(○) and S$_f$(□).
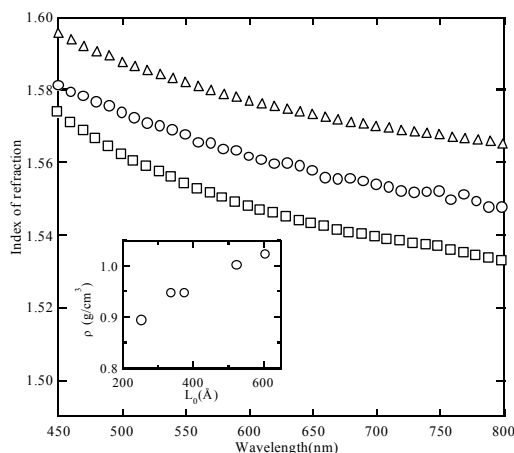

Figure 2 Index of refraction for PS2: Unswollen (△), L$_0$=523 Å (S$_f$=0.16) (○) and L$_0$=337 Å (S$_f$= 0.21) (□). In the inset, thickness dependence of ρ for PS2 is shown.

KINETIC REPRODUCIBILITY OF METHANE PRODUCTION FROM METHANE HYDRATES

Phillip Servio & Devinder Mahajan

Energy Sciences and Technology Department
Brookhaven National Laboratory
Upton, New York 11973-5000, USA

Introduction

Natural gas is the cleanest of all available fossils fuels and its use is increasing globally. This increasing demand is raising concerns regarding the long-term supply of this precious resource. Recent estimates have put the amount of stored methane in methane hydrates at several orders of magnitude higher than all presently known sources of methane. In order to pursue this abundant reserve, technological hurdles must be solved which will allow the safe capture of methane from dispersed hydrate sources around the world.

Experimental

A new experimental apparatus has been developed for the measurement of hydrate formation and decomposition kinetics, see figure 1. The main component of the hydrate phase equilibrium apparatus is a high-pressure reactor fabricated from 316 stainless steel. The vessel has rectangular viewing windows constructed from borosilicate and is immersed in a temperature-controlled bath consisting of an equal volume mixture of ethylene glycol and water. Experimental gas and water are brought into contact, in the reactor, in a countercurrent fashion. Water enters from the top, while the gas enters from the bottom to help agitate the liquid and clay sediments and achieve a uniform system. The experimental temperature of both the gas and liquid phases are measured with the aid of type K thermocouples. The pressure is measured by differential pressure transducers. The experimental methane gas flow rate into the system is measured and regulated by a mass flow controller (Brooks) with a range of 0-2000 ml per minute. A back pressure regulator is used to ensure constant pressure during both a formation and decomposition experiment. A dry test meter is used on the back pressure regulator side to measure the amount of gas exiting the high pressure vessel
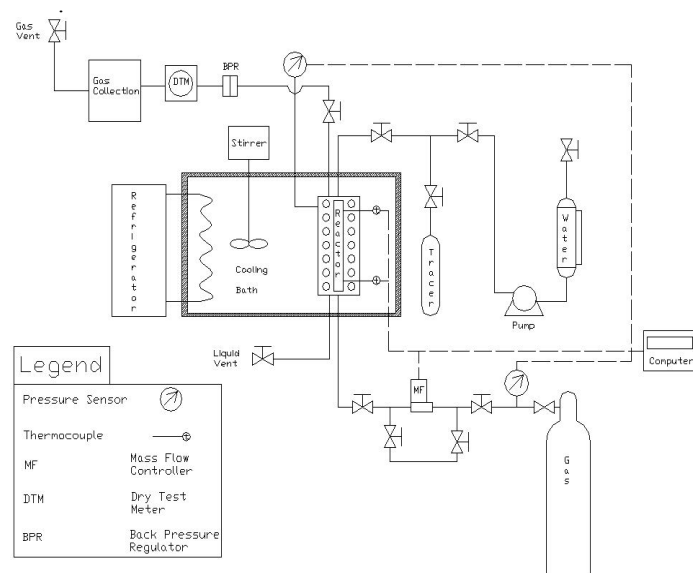

Figure 1. Newly Commissioned Unit for Hydrate Kinetic Study at BNL.

during the formation or decomposition process. Tracers may also be injected in order to determine sediment stability during the cycle of hydrate formation and decomposition.

Results and Discussion

The Kinetics of hydrate formation can be described in two steps, nucleation and growth. Nucleation is characterized as the time required for hydrate crystals to achieve a critical size nucleus that can sustain growth. The nucleation time is believed to be a stochastic phenomenon that cannot be predicted (Parent and Bishnoi, 1996). Hydrate growth is the process where hydrate nuclei have achieved the necessary critical size and continue to grow and form hydrate crystals. The driving force for hydrate growth is the difference in the fugacity of the dissolved gas and the three-phase equilibrium fugacity at the experimental temperature. Figure 2 shows a typical plot of moles of gas consumed vs. time during a hydrate formation experiment.
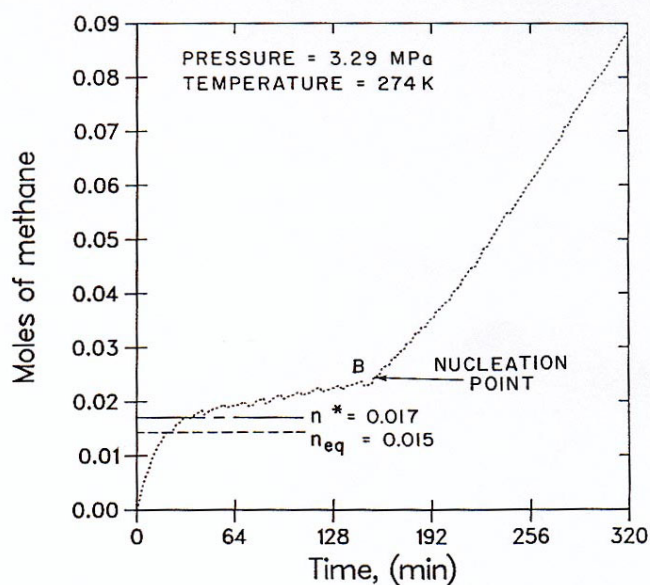

Figure 2. Moles of gas consumed vs. time for a methane hydrate formation experiment (adapted from Englezos et al., 1990).

In figure 2, the onset of hydrate formation occurs at the nucleation point, B, which is known as the turbidity time. The turbidity time denotes the first appearance of stable hydrate crystals and is the beginning of the hydrate growth phase. n^* is the number of moles of methane gas corresponding to a vapor-liquid water equilibrium. This equilibrium is hypothetical because hydrates form at these conditions. This would be the solubility of methane in water in the absence of hydrates. n_{eq} is the number of moles of methane dissolved in liquid water corresponding to a vapor-liquid-hydrate equilibrium pressure at the system temperature (Servio and Englezos, 2002). At the system temperature, the pressure is known as the incipient equilibrium hydrate formation pressure, P_{eq}. The value of n_{eq} is less then n^* in the hydrate formation region because it corresponds to a lower pressure, P_{eq}, then the experimental pressure. Experimental work by Servio and Englezos (2002) validated these results. It was hypothesized that the difference in moles of gas between point B (n_B) and n_{eq} accounts for the amount of gas consumed in the formation of hydrate nuclei as postulated by Englezos et al. (1987).

The hydrate decomposition process has not been as extensively studied as that of hydrate growth; fortunately the two processes have many similarities. A decomposition process can be viewed as decomposing particles surrounded by a desorption "reaction" layer, followed by a cloud of evolved gas (Kim et al, 1987). The decomposition of solid hydrates is an endothermic process that gives gas and liquid water as its products. Hydrate decomposition is thought to consist of the following two steps:

1) The destruction of the clathrate host lattice at the surface of the particle followed by the desorption of the guest molecule from the surface into the reaction layer.
2) The diffusion of gas from the reaction layer into the bulk liquid

The driving force is represented by the difference in fugacity of the gas at the three-phase equilibrium conditions (equilibrium temperature and pressure) and the dissolved gas fugacity at the experimental temperature and pressure. The latter fugacity is assumed to be equivalent to the fugacity of the gas at the solid particle surface.

Our current study relates to the methane hydrate formation and decomposition cycle in a recently commissioned unit. First, the baseline kinetic study is being carried out with CH_4/H_2O mixture under the temperature/pressure conditions that mimic the methane hydrate stability zone in the subsurface environment to establish data reproducibility. The baseline study will be followed by a kinetic study in the Euxinic seawater/CH_4 mixture to mimic seafloor environment. The known kinetic models will be reviewed with respect to their relevance to the measured data.

Typical models that will be evaluated for the production of methane gas from methane hydrate include those of Yousif et al. (1991) and Goel et al. (2001). Figure 3 shows the molar ratio of methane gas trapped at various dissociation pressures (Goel et al., 2001). Figure 4 gives the cumulative gas produced from hydrates at
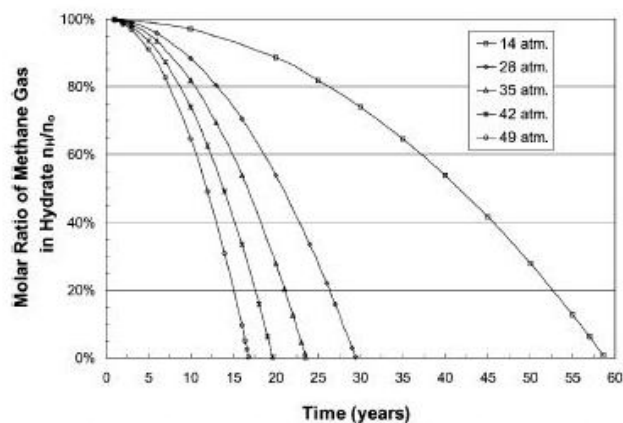

Figure 3. Molar ratio of methane trapped in hydrates at various dissociation pressure drops (adapted from Goel et al., 2001).

various dissociation pressure drops. It is important to note that figures 3 and 4 were produced under the assumption that the pressure drop is constant through the dissociation of the hydrates. In a reservoir the pressure drop is variable and is taken into consideration in the model of Goel et al. (2001).
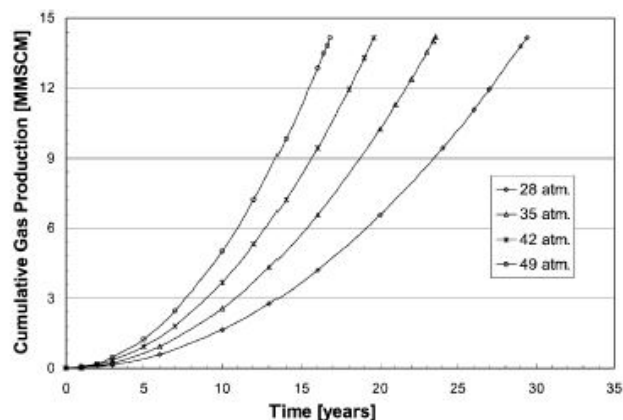

Figure 4. Cumulative gas produced from hydrates at various dissociation pressure drops (adapted from Goel et al., 2001).

The results obtained from this work will give valuable insight into the current state of existing models for the formation and dissociation of hydrates in porous media. These results will also provide us with information concerning the stability of sea floor hydrates and sediments under dissociation conditions.

References
1. Englezos, P., *Gas Hydrate Equilibria*, M.Sc Thesis, U. Calgary, 1990.

2. Englezos, P., Kalogerakis, N., Dholabhai, P. D., Bishnoi, P. R., *Kinetics of Formation of Methane and Ethane Gas Hydrates*, Chem. Eng. Sci., 42 (11), 2647-2658, 1987.

3. Goel, N., Wiggins, M., Shah, S., *Anayltic modeling of gas recovery from in situ hydrate dissociation,* Journal of Petroleum Sci. & Eng., 29, 115-127, 2001.

4. Kim, H. C., Bishnoi, P. R., Heidemann, R. A., Rizvi, S. S. H. *Kinetics of methane Hydrate decomposition*, Chem. Eng. Sci, 42 (7), 1645-1653, 1987.

5. Parent, J.S. and P.R. Bishnoi, *Investigations into the nucleation behavior of natural gas hydrates,* Chemical Engineering Communications (CEC), 144, 51-64, 1996.
6. Servio, P., Englezos, P., *Measurement of the amount of dissolved methane in water in equilibrium with its Hydrate*, J. Chem. Eng. Data, *47*(1), 87-90, 2002.

7. Yousif, M.H., Abass, H.H., Selim, M.S., Sloan, E.D., *Experimental and theoretical investigation of methane-gas-hydrate dissociation in porous media*, SPE Reservoir Eng., 69-76, February 1991.

STABILIZATION OF COPPER/ZIRCONIA BASED CATALYSTS FOR ALCOHOL SYNTHESIS

*Cheng Yang, Guisheng Wu, Wenhuai Li, Yuhan Sun**

State Key Laboratory of Coal Conversion,
Institute of Coal Chemistry, Chinese Academy of Sciences,
Taiyuan 030001 P.R.China

Introduction

Among other technologies based on syngas, direct alcohols synthesis represents a promising natural gas upgrading objective. It is widely recognized that higher alcohols together with methanol can be produced from syngas by appropriate modification of methanol synthesis catalysts and reaction conditions [1-2]. The conventional methanol synthesis is a highly exothermic process with 6-8 MPa, 260-280°C as operating conditions and a conversion of CO about 60% performed on CuZnAl catalyst. The synthesis of higher alcohols is a combination of parallel and consecutive reactions. The formation of alcohols becomes more exotherm with higher carbon number. In comparison with the other alcohols, methanol formation is limited thermodynamically at substantial lower temperature. Qualitatively, in the reaction of syngas to methanol and higher alcohols only the conversion of the reaction to methanol can be limited by the position of the thermodynamic equilibrium in the range of 10-30MPa and 300-420°C, whereas a similar situation is not expected in the case of ethanol, n-propanol and isobutanol [3]. However, such reaction conditions are hardly consistent with the preservation of a high dispersion of reduced copper.

Palladium is also well known as an active phase for CO hydrogenation. Indeed, an alkalized PdZnMrZrO2 catalyst has been developed for methanol-isobutanol synthesis, as ZrO_2 was claimed to be active for iso-synthesis [4]. The catalyst for the process also requires high temperatures (>400°C) and pressures (>12 MPa) and produce isobutanol with relatively low productivity (<100 g/kg-cat·h). Moreover, the addition of palladium into other metal catalysts can lead to a substantial improvement in catalytic properties due to its excellent candidates of activate hydrogen, which could then spread over the neighboring phases through a hydrogen-spillover mechanism. It has been demonstrated that active catalyst for the synthesis of methanol can be prepared by dispersing Cu on ZrO_2 [5]. Thus, the objective of this work is first to stabilize a Cu/ZrO_2 catalyst by introducing La and Mn. Then, the most efficient catalyst for methanol synthesis is shifted towards higher alcohols under mild conditions using K as a promoter. The modification is further made in the catalyst composition by Pd to increase the production of higher alcohols without simultaneously increasing unwanted methanation and other hydrocarbon by-products.

Experimental

Catalysts preparation. Catalytic formulations were prepared by co-precipitation in constant pH conditions about 10-11 using the corresponding metal nitrates as precursors (Cu:Mn/La:Zr molar ratio = 1:0.5/0.1:2) with aqueous sodium carbonate solution, followed by aging, washing and drying. Pd and K were doped by wetness impregnation K_2CO_3 and $Pd(NO_3)_2$ with the precipitates, and then the samples were calcined at 350°C for 4 hr under air. The Pd and K loading in the prepared catalysts were 0.5wt% and 5.0wt%, respectively.

* Corresponding author. Fax: +86-351-4041153. E-mail address: yhsun@sxicc.ac.cn, yangch68@sxicc.ac.cn

Catalytic activity test. CO hydrogenation tests were carried out using a stainless steel fixed-bed reactor, which contained 1.0ml catalyst. All the catalysts were reduced in H_2 (5% in N_2) flow at 300 °C and atmospheric pressure for 6 hr before syngas exposure. Shimazu-8A GC was used to analyze the products. H_2, CO, CH_4 and CO_2 were determined by thermal conductivity detector(TCD) equipped with a TDX-101 column. The water and methanol in liquids were also detected by TCD with a GDX-401 column. The alcohols and hydrocarbons were analyzed by flame ionization detector(FID) with a Propake-Q column.

Characterization Methods. The surface area of the catalysts was measured at -196°C by nitrogen adsorption using a BET apparatus (ASAP 2000). The dispersion degree of Cu was calculated by N_2O-adsorption performed in a micro-reactor, followed with MS. The transmission EXAFS measurements were conducted in the 4B9A beamline in Beijing Synchrotorm Radiation Facility operating at 30-50mA and 2.2GeV. X-ray power diffraction was carried out with a Rigaku D/Max diffractometer equipped with a Cu target and Ni filter. TG-MS was used to determine the amount of carbon deposited on a TGA-92 from TA Instruments.

Results and Discussion

Table 1. The structural parameters of La and Mn modified Cu/ZrO_2 catalysts

Catalyst	S_{BET} (m^2/g)	D_{Cu} (%)	CuO fitting parameter [a]	
			N	R/(Å)
Cu/ZrO_2	128.86	2.92	3.60	1.948
$Cu/La/ZrO_2$	144.16	4.12	3.57	1.952
$Cu/Mn/ZrO_2$	171.01	5.54	1.83	1.945

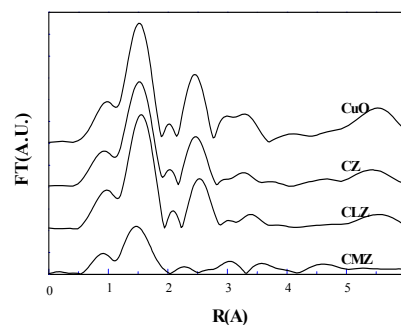a: The coordination number and Cu-O bond length of pure CuO is 4.0 and 1.96, respectively.

Figure1. The RSF profile of La and Mn modified Cu/ZrO_2 catalysts

The catalyst structure greatly changed with the Mn and La addition (see **Table 1**). The surface area increased and highly dispersed copper appeared suggested that both Mn and La could promote the dispersion of the active phase. The radial structure functions (RSF) obtained around Cu atom are shown in **Figure 1**. The coordination number of Cu-O in $Cu/Mn/ZrO_2$ was much lower than that in $Cu/La/ZrO_2$, indicating that a CuMnOx complex formed [6], though only a broad peak could be detected in XRD patterns (not presented). On the contrary, La was facile to enter the lattice of ZrO_2 crystals and enhanced the $Cu-ZrO_2$ interaction [7]. Sun [5] found that the strength and nature of the interaction between the dispersed Cu and ZrO_2 rather than their surface area is decisive for the activity of CO hydrogenation. Clearly, the addition of La and Mn both promoted the

activity of Cu/ZrO_2 for methanol synthesis, and methanol yield on $Cu/La/ZrO_2$ was much higher than that on $Cu/Mn/ZrO_2$ catalyst (see **Figure 2**). It could be interpreted that La and Mn played different roles in influencing the interaction of the components, besides increased the dispersion of active phase Cu. More interestingly, it was found that La and Mn in the co-modified Cu/ZrO_2 catalyst performed a synergistic promotion in improving the catalytic activity for methanol synthesis (see **Figure 3**). The yield of methanol reached 1.8 g/ml-cat.h under 6.0MPa at the GHSV of $7000h^{-1}$.
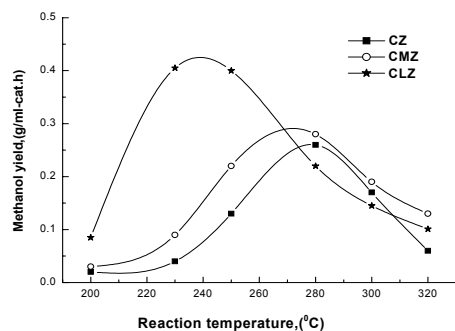
Figure 2. Activity of La and Mn modified Cu/ZrO_2 catalysts for methanol synthesis, Reaction conditions: P=6.0MPa, GHSV=3000 h^{-1}, H_2/CO (molar)=2.0: 1
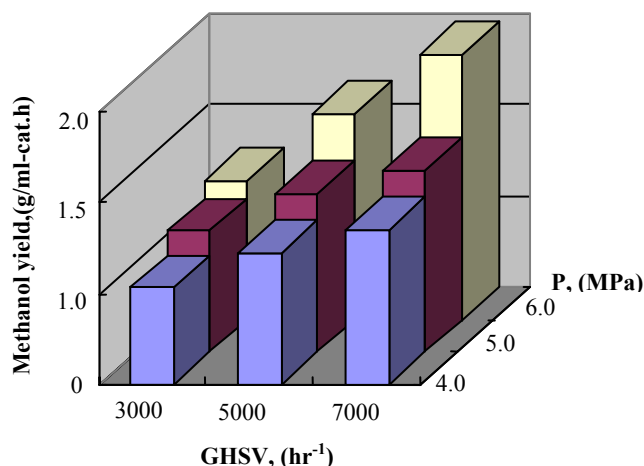
Figure 3. Catalytic performance of La and Mn co-modified Cu/ZrO_2 catalysts for methanol synthesis

K was usually used as a promoter for methanol synthesis shifted towards higher alcohols. As shown in **Table 2** and **Figure 4**, K-CLMZ catalyst showed high performance for higher alcohols synthesis. Naturally, the BET surface area of the alkalized catalyst was drastically decreased as K doped in the pore. The activity of K-CLMZ was also decreased comparing with that of CLMZ catalyst, but it was successfully shifted methanol synthesis towards higher alcohols with amount of CO_2 and hydrocarbons as the by-products. It was noticed that the texture of K-CLMZ catalyst was seriously destroyed during the catalytic test and amount of carbon was deposited on the surface. This suggested that the alkalized catalyst could not serve the relatively severe conditions, i.e. lower H_2/CO radio and high reaction temperature and pressure.

Apparently, the activity was remarkably promoted by Pd addition to K-CLMZ catalyst. Though the selectivity of alcohols and the amount of $C^{2+}OH$ was slightly increased, their yields were both

Table 2. Activity and selectivity of alkalized $CuMnLaZrO_2$ (CLMZ) and $PdCuLaMnZrO_2$ (PCLMZ) catalysts for higher alcohols synthesis

Catalyst	CO Conv (%)	Selectivity, (C-atom%)			Alc.STY (g/ml/h)
		CHx	CO_2	ROH	
K-CLMZ	32.04	28.42	29.32	42.26	0.596
K-PCLMZ	57.38	31.89	24.37	43.74	0.716

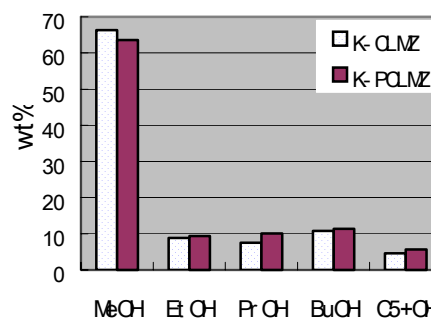Reaction conditions: T=360℃, P=12.0MPa, GHSV=8000 h^{-1}, H_2/CO (molar)=1.0: 1

Figure 4. Alcohol distributions over K-CLMZ and K-PCLMZ

remarkably improved. This might due to Pd as an excellent candidate of activate hydrogen, which could spread over the neighboring phases through a hydrogen-spillover mechanism, then improved the rate of carbon hydrogenation and retarded the carbon deposit. Fujimoto and Yu[8] investigating the spillover effect of hydrogen on Pd or Pt promoted Cu/ZnO-based catalysts, arrived at a conclusion that the introduction of Pd led to an increase in the activity as well as the stability of the catalysts poisoning by water. This might be the reason that the texture of K-PCLMZ only slightly destroyed comparing with that of K-CLMZ catalyst. The catalysts performed the similar behavior as Fujimoto and Yu observed.

Table 3. The texture of alkalized $CuMnLaZrO_2$ (CLMZ) and $PdCuLaMnZrO_2$ (PCLMZ) catalysts and carbon deposit

Catalyst		S_{BET} (m^2/g)	V_P (ml/g)	d_P (nm)	Carbon (wt%)
K-CLMZ	Fresh	94.66	0.100	4.24	-
	Tested	27.85	0.039	6.73	0.51
K-PCLMZ	Fresh	88.91	0.141	4.62	-
	Tested	41.80	0.647	5.73	0.27

References
1. Herman, R. G., *Catal. Today*, **2000**, *55*, 233-245
2. Stiles, A. V., et. Al., *Ind. Eng. Chem. Res*., **1991**, 30, 811-821
3. Verkerk, K. A. N., Jaeger, B., Finkeldei, C. H., Keim, W., *Appl. Catal.,* **1999**, 186, 407-431.
4. Wilhelm, K., Wolfang, F., **1989**, 3, 59-64.
5. Sun,Y. H., Sermon, P. A., *J.Chem.Soc.Chem.Commun*., **1993**, 16, 1242-1244.
6. Porta, P., Moretti, G., Musicanti, M., Nardella, A., Catal. Today, **1991**, 9, 211-218.
7. Andriamasinoro, D., Poix, P., Kiennemann, A., Kieffer, R., Appl. Catal. A: General, **1993**, 106, 201-207.
8. K. Fujimoto, Y. Yu, *Stud. Surf. Sci. Catal*., **1993**, 77, 393-396.

INFLUENCE OF PREPARATION ON STRUCTURAL AND CATALYTIC PROPERTIES OF PALLADIUM PROMOTED COPPER/ZIRCONIA CATALYSTS

*Minggui Lin[1], Cheng Yang[2], Yongkui Shan[1], Wei Wei[2], Yuhan Sun[*1,2], Mingyuan He[1]*

[1] Department of Chemistry, East China Normal University, Shanghai 200062 P. R. China
[2] The State Key Laboratory of Conversion, Institute of Coal Chemistry, Chinese Academy of Sciences, Taiyuan 030001 P.R.China

Introduction

The traditional low-temperature low-pressure methanol synthesis catalysts, based on $CuO/ZnO/Al_2O_3$ by BASF, were still the subject of extensive fundamental studies, which allowed recently to envisage other supports and in particular, zirconia. Indeed, ZrO_2 is of special interest because of its character of abundant oxygen vacancy, redox property, thermal mechanical stability, high specific surface area, and intrinsic catalytic properties. In recent years, a number of zirconia-containing catalysts have been developed. Especially, metal/zirconia based systems showed interesting catalytic behavior for hydrogenation reaction. For example, zirconia supported copper catalyst has been found to exhibit excellent properties for the methanol synthesis from syngas [1]. Palladium is also well known as an active phase for CO hydrogenation. Moreover, the addition of palladium into other metal catalysts could lead to a substantial improvement in catalytic properties due to its excellent candidates of activate hydrogen, which could then spread over the neighboring phases through a hydrogen-spillover mechanism. Fujimoto and Yu [2], investigating the spillover effect of hydrogen on Pd or Pt promoted Cu/ZnO-based catalysts, arrived at a conclusion that the introduction of palladium led to an increase in the activity as well as the stability of the catalysts poisoning by water. Similar observation has been made by Sahibzada *et al.* and Melian-Cabrera *et al.* [3,4].

The present study focuses on the influence of preparation variables on the structural and catalytic properties of palladium promoted copper/zirconia catalysts for methanol synthesis from CO/H_2. The catalysts were characterized by means of nitrogen adsorption, X-ray powder diffraction (XRD), temperature-programmed reduction (TPR) and nitrous oxide titration.

Experimental

Catalyst preparation. The copper/zirconia (Cu:Zr molar radio =1:2) catalyst were prepared by conventional co-precipitation from a solution of $Cu(NO_3)_2$, $ZrOCl_2$, with Na_2CO_3 under electromagnetic stirring at 70℃. The precipitate was aged, washed with distilled water free of Cl^-, then dried overnight at 120℃ and calcined at 350℃ for 3 hr in air. The catalysts containing 0.2 wt% Pd were prepared by the wetness impregnation method using $Pd(NO_3)_2$ as the precursor. One was dried and the other further calcination following procedures as above, denoting with PCZ-d and PCZ-c respectively.

Catalytic activity test. Activity tests were carried out using a stainless fixed-bed flow reactor with I.D. of 8mm. The catalyst evaluated was hold in the middle of the microreactor, then was reduced in a gas of H_2/N_2 mixture (10% in N_2) at 290℃ for 8 hr with temperature-programmed controller before exposure to syngas. The composition of feed gas was $H_2/CO=2$ with trace amount of CO_2. CO

* Corresponding author. Fax: +86-351-4041153. E-mail address: yusun@sxicc.ac.cn yangch68@sxicc.ac.cn

hydrogenation was employed at 8.0MPa overall pressure and with a space velocity of $8000h^{-1}$. H_2, CO, CH_4, and CO_2 were separated by using a carbon size column and were monitored by thermal conductivity detector. The liquid products were separated by using Porapak Q column and detected by a flame ionization detector.

Characterization Methods. The surface area of the samples was determined at -196℃ by nitrogen adsorption using a BET apparatus (ASAP 2000). The powder X-ray diffraction were performed on a D/max- ɤ A diffractmeter. The amount of exposed copper was measured using a nitrous oxide chemisorption method called reactive frontal chromatography (RFC). TPR experiments were carried out at a heating rate of $10℃min^{-1}$ with a programmable temperature controller. An H_2/Ar mixture (5% in Ar) was passed over the catalyst at a total flow-rate of 50 cm^3min^{-1} and hydrogen consumption was monitored by a thermal conductivity detector.

Results and Discussion

Table 1. Morphological properties of catalysts

Samples		S_{BET} m^2/g	V_p cm^3/g	d_P nm	D_{Cu} (%)
CZ	Flesh	148.9	0.127	3.423	2.89
	Used	45.0	0.047	4.236	1.30
PCZ-d	Flesh	131.2	0.134	4.074	1.12
	Used	67.2	0.069	4.130	1.45
PCZ-c	Flesh	117.8	0.117	3.981	1.31
	Used	46.4	0.051	4.433	1.14

The addition of 0.2wt%Pd into copper/zirconia system led to a slight change in BET surface area as shown in **Table 1**. A further loss of special surface area for palladium promoted Cu/ZrO_2 catalyst was followed with calcinations of pre-dried sample at 350℃ under air. After exposure to hydrogenation condition, all samples suffered from a sharply decrease of BET surface area compared to the fresh ones. Considering the loss of the porous volume of all samples (**Table 1**), one should consider that this might be resulted partially from the plugging of microporous fraction of samples by coke deposition on the catalyst surface originated from the Boudouard reaction:

$$2CO (g) = CO_2 (g) +C (s)$$
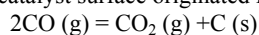
Moreover, it is worth noting that PCZ-d catalyst seems to exhibit more effective capability of coke deposition resistance than that of other catalysts, therefore possesses larger porous volume. Because of its ability of activate hydrogen followed spread over the neighboring phase through spillover mechanism, the existence of palladium causes more abundant hydrogen resource required for CO hydrogenation on Cu/ZrO_2 catalyst surface. Therefore, this will reduce the coke deposition to some extent due to sufficient hydrogen pressure on the catalyst surface [5].

The results of copper dispersion were also presented in **Table 1**. Similar to the trend in BET surface area, a large loss of metal Cu dispersion can be observed after CZ catalyst underwent CO hydrogenation, decreasing from 2.89% to 1.30%. In the case of palladium promoted Cu/ZrO_2 catalysts, there is essentially no difference between the flesh catalysts and the used ones, even PCZ-d with better dispersion.

XRD measurements were operated to investigate the phase composition and the changes induced by the pretreatment of the precursors. In all samples, the zirconia phase gave rise to a very broad peak (not presented), indicating either a state of very low

crystallinity or the presence of very small zirconia crystallites before reaction as well as after exposure to CO hydrogenation condition.
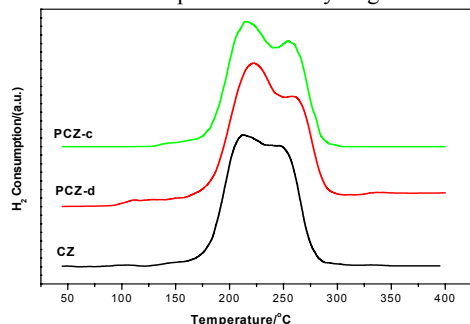

Figure 1. The TPR profiles of the catalysts

Before catalytic activity test, catalysts have been characterized by TPR with hydrogen as the reducing gas, and the resulting TPR profiles are shown in **Figure 1**. For all samples, only two reducing peaks can be seen at 215-220℃ and 250-260℃, which are agreement with the results of Shimokawabe *et al.*[6], who have demonstrated that the lower temperature peak centered at 220℃ is due to the reduction of the highly dispersed cupric oxide with an octahedral environment while the higher temperature one corresponding to 242-290℃ ascribed to these of the bulk-like CuO. Compared with binary copper/zirconia catalyst, the ternary catalysts exhibited a higher intensity of the peak of lower temperature at the expense of the magnitude of higher temperature peak. This must be attributed to the typical effect of hydrogen spillover as a result of Pd addition between the palladium component and zirconia support, although it also occurred in the interphase of copper and zirconia. On this phenomenon, hydrogen atoms activated by palladium and/or copper components spread over zirconia on layer and sublayer surface at lower temperature, and then were released for reduction of CuO through the reverse spillover function at elevated temperature, a mechanism observed by R.Burch *et al.* [7] over Cu/ZnO catalyst. These authors proposed that ZnO can act as a reservoir for spillover hydrogen, and that reverse spillover may account for the higher rate of methanol synthesis on Cu when ZnO is present in the catalyst. Accordingly, it must be the spillover/reserve spillover mechanism partially responsible for high activity (discussed below) of the ternary catalysts. Hydrogen spillover and inverse spillover function were also reported over rhodium-based catalysts [8].
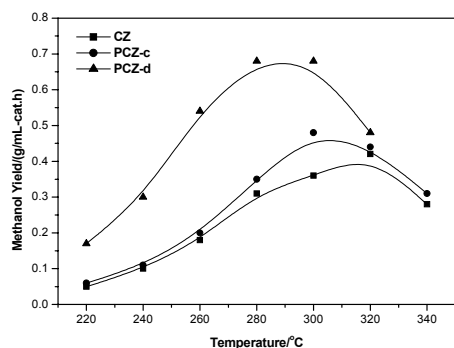

Figure 2. Catalytic activity of samples as a function of reaction temperature. Reaction conditions: P=8.0MPa; GVSH=8000h[-1].

The catalytic performances of samples were investigated after drying as well as after calcination at 350℃. It can be observed from

Figure 2 that zirconia supported copper catalysts, either alone or combined with palladium promoter, exhibit highly active properties for methanol synthesis. Surprisingly, space time yield (STY) increased from 0.42g/mL-cat.h at 320℃ for CZ catalyst to 0.68g/mL-cat.h at 280℃ for PCZ-d catalyst while that of PCZ-c was only influenced slightly, revealing clearly that the various pretreatment of the catalyst precursors causes a disproportionately significant effect in methanol synthesis activity. Palladium promotion in traditional Cu/ZnO-based catalysts for methanol synthesis from CO_2 has been studied by several groups [3,4].

Apparently, it is established that catalytic properties of samples does not correlate with measured BET surface area, and these textural changes therefore cannot explain the unexpected increase in activity observed over PCZ-d catalyst. Moreover, there is no apparent correlation of the activity rise with the changes in the amount of exposed copper of ternary catalysts, especially, PCZ-d catalyst. We suggest that high activity is related to the presence of amorphous zirconia as proposed by R. A. Koeppel *et al.* [9]. In the work, these authors suggested that the presence of anions like acetate, formate or nitrate in the precursors could result in a distortion of the oxide structure of zirconia due to the partial replacement of oxygen ions by these anions, and therefore inhibit the phase transformation of amorphous zirconia. And in their opinions, the crystallization of the amorphous zirconia is likely to result in a drastic decrease of the copper/zirconia interfacial area, which is decisive factor of methanol activity.

In summary, on the basis of the present findings that the Pd promotion in methanol production varied greatly with pretreatment method employed, single phenomenon cannot be responsible for this trend in catalytic activity. On the one hand, the structural modification of zirconia support by dopant anions must be considered according to other publications reported, and the resort of NO_3^- in the zirconia lattice causing distortion of structure appeared to be cause of the activity change of PCZ-d catalyst; on the other hand, hydrogen spillover mechanism should not be ruled out judging by the discussion above. However, further experiment work is required to confirm such hypothesis and provide a definite interpretation.

References
1. Y. H. Sun, P. A. Sermon, *J. Chem. Soc. Chem. Commun.,* **1993**, 16, 1242-1244.
2. K. Fujimoto, Y. Yu, *Stud. Surf. Sci. Catal.*, **1993***, 77, 393-396.
3. M. Sahibzada, K. Chadwick, I. S. Metcalfe, *Catal. Today*, **1996**, 29, 367-372.
4. I. Melian-Cabrera, M. Lopez Granados, J. L. G. Fierro, *Catal. Lett.*, **2002**, 79, 165-170.
5. J. T. Sun, I. S. Metcalfe, M. Sahibzada, *Ind. Eng. Chem. Res.*, **1999**, 38, 3868-3872.
6. M. Shimodawabe, H. Asakawa, N. Takezawa, *Appl. Catal.*, **1990**, 59, 45-58.
7. R. Burch, S. E. Golunski, M. S. Spencer, *J. Chem. Soc. Faraday Trans.*, **1990**, 86 (15), 2683-2691.
8. T. Inui, T. Uamanoto, M. Inoue, H. Hara, T. Takeguchi, J. Kim, *Appl. Catal., A: General*, **1999**, 186, 395-406.
9. R. A. Koeppel, A. Baiker, C. Shild, A. Wokaun, *Stud. Surf. Sci. Catal.*, **1991**, 63, 59-68.

OVERVIEW OF UTILIZATION PROSPECTS FOR COAL MINE METHANE

Ray Zahradnik and Charles D. Estes

Appalachian-Pacific, LLC.
1401 Wilson Boulevard
Suite 1101
Arlington, VA 22209

Introduction

Coal Mine Methane (CMM) refers to methane that is released from coal mines as a consequence of the mining operation. CMM has historically been perceived as a safety hazard in mining operations. It can be released during operations at the mining face, where it is generally removed by circulating air that maintains methane concentrations well below safety standards. It can be released after mining has occurred, as in the case of longwall mining, and is generally vented to the atmosphere by means of drilled openings that are referred to as gob wells. It can also be released after a mine has been decommissioned and shut in. In this instance, it is released to the atmosphere by means of vent wells and/or natural fissures in the surrounding rock formation.

It is estimated that in the United States over 300 million cubic feet of CMM are released to the atmosphere every day. Methane is a potent greenhouse gas and contributes to environmental problems such as global warming, retropospheric ozone formation, and potentially stratospheric ozone depletion. The Intergovernmental Panel on Climate Change estimates the potency of methane to be 22 to 24.5 times that of carbon dioxide. On this basis, the daily discharge of CMM is equivalent to the exhaust of between 5 and 6 1000MW power stations.

Apart from being hazardous and environmentally dangerous, CMM represents a potentially attractive raw material, and its recovery and utilization can be a profitable venture under certain conditions. At a value of $1/MCF, the worth of the vented CMM in the United States represents $100 million annually. Whether the capital expenditure needed to capture and utilize CMM is economically justified has been the subject of a long-term investigation by Appalachian-Pacific, LLC. (AP)

Technologies for Recovering and Utilizing CMM

The composition of CMM varies, depending upon how it is obtained. In a mine ventilation shaft, where much of the CMM is released, the methane concentration is 1 or 2 %, with the remainder being air. In gob wells, the methane concentration ranges from 50 to 80 %. CMM released from shut-in mines varies from 60 to 90 % methane, with nitrogen and carbon dioxide comprising the rest. Both the composition and the flow of CMM from all of these sources vary with time and conditions, presenting a problem for potential utilization.

The simplest recovery system consists in capturing CMM as it is released from gob wells or from shut in mines by means of collection lines attached to the wells. The gas is at atmospheric pressure and generally saturated with water. Such gas can be introduced into natural gas pipeline with a minimum of processing, which would include drying and pressurization. CMM is often below pipeline standards, but because it is such a small quantity in relation to the pipeline flow, pipeline companies often accept it.

A second utilization procedure is to use the CMM as a fuel for electrical generation. Depending upon the system used to generate power, the CMM may need little additional processing. However, the uneven nature of the flow and composition presents operational problems for the power system, and both gas clean up and storage may be required for optimal economic advantage.

A third utilization scheme is to liquefy the methane in CMM to produce LNG for sale as an alternate transportation fuel. This represents the highest value-added use for CMM, but requires the most elaborate and expensive processing facilities. AP has been involved in a cost-shared project with the US DOE to determine an appropriate technology and marketing plan for the production and sale of LNG from CMM for the past several years.

The Production and Sale of LNG from CMM

In order to produce LNG from CMM in a cost competitive manner, technologies that are compatible with the production rates and composition variability of CMM are necessary. AP has developed process designs that satisfy these requirements. A critical element in the design is a small-scale liquefier that is both efficient and inexpensive. AP plans to use a Thermoacoustic liquefier being developed by Praxair, Inc., based upon initial investigations by LASL.

The basis of the Thermoacoustic liquefier is the use of a Thermoacoustic engine to provide the power for a refrigeration cycle. (1) A 100 gpd pilot unit to liquefy methane was constructed and tested with good results in the late 90's, and a 500 gpd unit is currently undergoing testing and verification. (2) A photograph of this experimental unit is provided in Figure 1.

Figure 1. Photograph of Prototype 500 gpd Thermoacoustic Liquefier.

If these tests are successful, AP plans to incorporate a 10,000 gpd Thermoacoustic refrigeration unit into a CMM recovery and processing facility to be located in West Virginia. The LNG produced would be sold into the heavy-duty transportation market.

A process design for this facility has been completed, based upon a feed stream of CMM from a shut-in mine. Alternative gas conditioning systems have been considered. The purpose of the gas conditioning system is to remove CO_2 and water vapor prior to entering the refrigeration unit. In some cases oxygen is present in the CMM, which also must be removed.

Both amine scrubbing and cryogenic removal have been considered for this operation. Depending upon the conditions of the feed stream and the overall system balances, either option may be employed.

A process schematic for the overall system is provided in Figure 2. The details for this design and for the Liquefier will be provided in the complete paper.
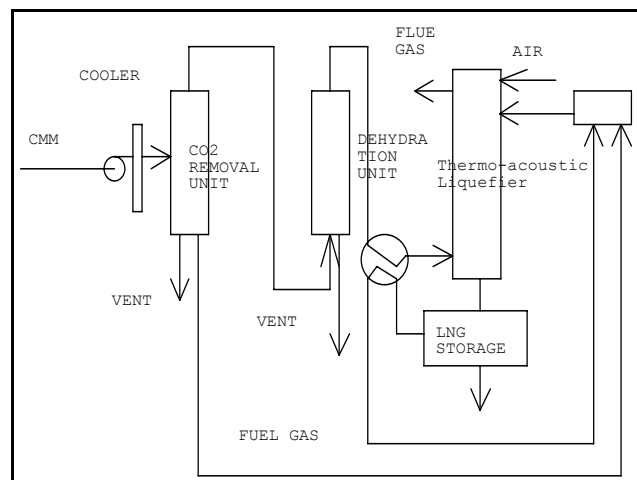

Figure 2. Process schematic for producing LNG from CMM.

In general, a portion of the CMM feed stream can be used to provide the combustion gas for the Thermoacoustic liquefier, as shown in Figure 2.

Fuel gas may also be needed for the onsite generation of electrical power. Depending upon the availability and composition of the CMM and the decision to generate electricity, the overall system material balances must support these options.

CMM itself may be used directly as a fuel gas. In this case, the separation scheme following the liquefier is somewhat more involved, as shown in Figure 3.

Various cost projections for the venture will also be presented, along with a discussion of the economic sensitivities.

Because LNG has not become generally accepted in the West Virginia area as an alternative fuel, AP plans to conduct a market priming program, aimed at providing information to potential users about the features of LNG utilization as well as initial sales. AP is being aided in this effort by West Virginia University
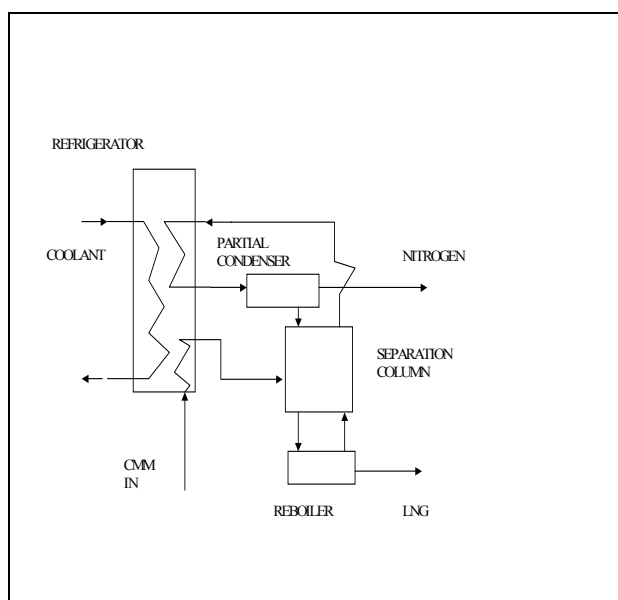

Figure 3. Schematic of Refrigerator, showing how nitrogen can be rejected at tail end of process.

.

Conclusions

CMM represents both an environmental problem and an economic opportunity. There are problems involved with its capture and utilization that are technical, economic, and institutional. The complete paper will include a discussion of these problems.

There are other projects underway under the DOE cooperative program that provide additional perspective on the utilization of CMM. These will also be discussed.

References
1. Swift, G. W., Thermoacoustics: A Unifying Perspective for some Engines and Refrigerators. *Acoustical Society of America Publications, Sewickley, PA* 2002.

2. Wollan, J. Praxair, Inc. Private Communications

OPPORTUNITIES FOR CLEAN FUELS FROM LAND FILL GAS

James Wegrzyn

Energy Sciences and Technology Department
Brookhaven National Laboratory
Upton, New York 11973-5000, USA

Introduction

The US Department of Energy estimates that if bioreactor technology were applied to 50% of the waste that's currently being deposited in landfills, it would provide over 270 billion cubic feet of methane annually. Bioreactors are defined as any landfill cell where liquid and/or air is added in a controlled fashion to accelerate bio-stabilization. However besides providing waste stabilization, bioreactors also increase the production rate of methane. This presents the opportunity for making clean fuels from a sustainable energy source (*i.e.* municipal solid waste). Although 270 billion cubic feet of methane might seem like a large number, it's small when compared with the US annual fuel consumption. The interest therefore in clean fuels from landfill gas is not to address the countries energy security problem, but rather in developing a market driven and environmentally sound approach for converting LFG to liquid fuel. This paper suggests the replacement of the biomass gasification and hot gas cleanup route to GTL with a bioreactor and cold gas cleanup process.

Description

The four major subsystems of converting wastes to clean fuels are; 1) bioreactor, 2) gas cleanup, 3) methane steam reforming or partial oxidation, and 4) gas to liquid technologies. Information on each of these four components can be readily found in the open literature. A brief review is being given here for the purpose of completeness.

Bioreactor. The bioreactor landfill is an emerging technology for solid waste management, although it has been a subject of research since the 1960s. More recent and complete reviews are available [1,2,3]. This paper will attempt to simplify a very complex biological system by starting with Equation (1).

$$C + H_2O \rightarrow 1/2CO_2 + 1/2CH_4 \quad \text{anaerobic} \quad [1]$$
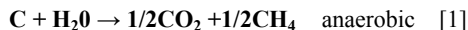
But in fact a consortium of microorganisms (fermentative, acetogenic and methanogenic) is necessary to convert organic material into methane and carbon dioxide. Justification for using Eqn. (1) is that the typical LFG composition follows Equation (1) as being 50% methane; 40% carbon dioxide; and 10% nitrogen, oxygen and VOCs. Also aerobic bioreactors can stabilize waste and compliments the anaerobic activity. The optimum bioreactor appears to be a hybrid bioreactor which combines the positive features of both the anaerobic and aerobic reactions. The major difference between a bioreactor and a "dry tomb" conventional landfill is the controlled addition of moisture. "The recirculation system employed to distribute moisture throughout the waste mass is the most critical operational component in the bioreactor process [4]". US EPA has identified six advantages of bioreactors over dry tomb landfills.

- Waste stabilization in years vs. decades
- Lower waste toxicity and mobility
- Reduced leachate disposal costs
- Significant increased LFG generation
- Reduced post-closure cost

This paper looks at taking advantage of this increased LFG generation rate for the production of 5,000 to 10,000 gallons per day of clean synthetic fuels.

Landfill Gas Cleanup Landfill gas has become a marketable energy resource. Projects include power generation, pipe line grade natural gas and more recently the production of liquefied natural gas. In the case of LNG there are currently three cleanup technologies being considered; adsorbents, chilled methanol[5] and liquid CO_2 wash[6]. The first two gas cleanup technologies are well document in the literature, so discussion will be limited to applying the CO_2 wash technology for LFG cleanup. The Acrion CO_2 wash technology is an absorbent column that utilizes the excellent solvent property of liquid CO_2. The process requires water and hydrogen sulfide removal prior to compression. Nominal operating conditions are -50°C and 25 bar pressure. At these conditions approx. 10% of the CO_2 is condensed at the top of the reactor (Figure 1) and flows down a high surface area packed bed removing all contaminants. Independent analysis was not able to detect any contaminants in the process stream. Gas composition by volume at the outlet was measured to be; 63.4% methane, 27.8% carbon dioxide, 07.4% nitrogen and 01.4% oxygen. Detection sensitivity was at the ppm or better level. This feed stock of high purity gas offers wider selections of catalysts and longer catalysts life for the subsequent GTL process.
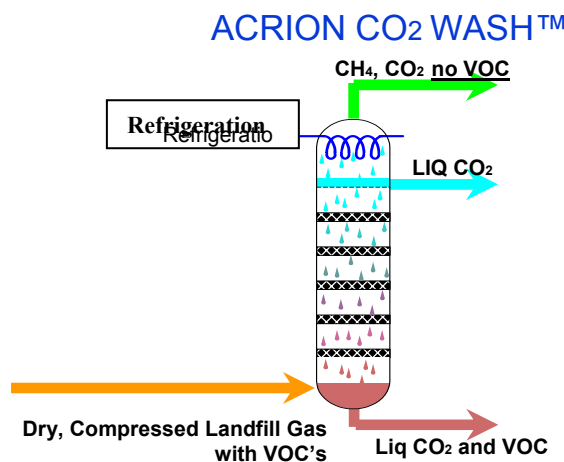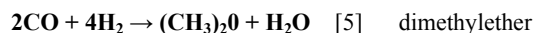

Figure 1. Liquid CO_2 wash technology for the removal of volatile organic contaminants (VOC) from a LFG process stream

Stream/Dry Reforming Natural Gas The two methods of producing syn-gas from natural gas are partial oxidation and reforming. The reforming of natural gas requires higher temperatures than partial oxidation (steam reforming ~ 800°C equation (2) and dry reforming ~ 1200°C Equation (3)). However since landfills have a flaring system to incinerate the VOCs, access to high temperatures is not a major problem. Also it's worth noting that the use of dry reforming reduces the atmospheric venting of CO_2 by incorporating it into the fuel process stream.

$$CH_4 + H_2O \rightarrow CO + 3H_2 \quad [2] \quad \text{steam reforming}$$

$$1/2CO_2 + 1/2CH_4 \rightarrow CO + H_2 \quad [3] \quad \text{dry reforming}$$
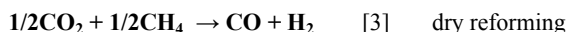
The reformer is the major capital cost item in the production of syn-gas. Using the heat from incineration for reforming will require a separate engineering/cost study.

Gas to Liquid Technologies GTL is both a mature and emerging technology. Equations (4-6) represent GTL technologies in its simplest form without the associated catalyst roles and activities.

$$CO + 2H_2 \rightarrow CH_3OH \qquad [4] \qquad \text{methanol synthesis}$$

$$2CO + 4H_2 \rightarrow (CH_3)_20 + H_2O \quad [5] \qquad \text{dimethylether}$$

$$nCO + 2nH_2 \rightarrow -(CH_2)_n- + nH_2O \quad [6] \qquad \text{Fischer-Tropsch}$$

Equation (6) assumes the cessation of water-gas shift activity[7], but the hydrocarbon product distribution will still follow the observed Anderson, Schutz and Flory (ASF) distribution.

Proposed Process Flow

The problem at hand is to link the various subsystems into an energy efficient and environmentally sensitive system that will also make a business case to attract investment. There are multiple approaches to solving to this problem. The process flow diagram shown in Figure 2 was selected based on simplicity, waste stabilization and product optimization. No attempt was made to determine a return on investment (ROI) for the proposed process.
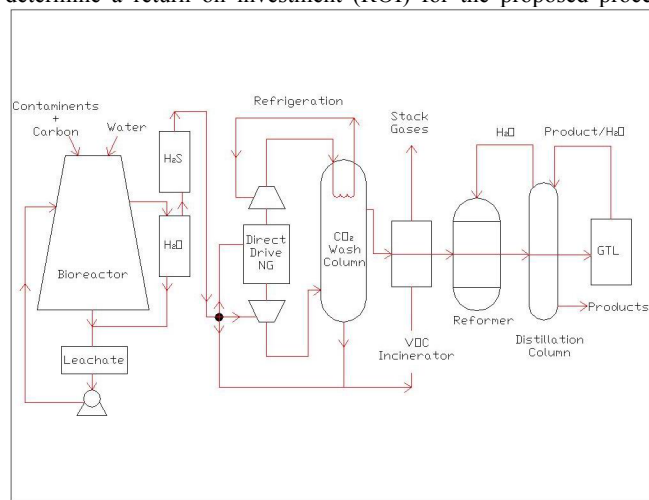

Figure 2. Waste to clean fuel process flow diagram for 5,000-10,000 diesel equivalent gallon per day output.

The clean gas composition from the outlet of the wash column is nominally three parts methane to one part carbon dioxide. The criteria of one part CO with two part H_2 for optimum liquid fuel synthesis, see Equation (6), requires the addition one part water, see Equation (7). This water can be recycled from the distillation column. The remaining water from the distillation column can help meet the water demand of the bioreactor.

$$3/4CH_4 + 1/4CO_2 + 1/2H_2O \rightarrow -CH_2- + H_2O \quad [7]$$
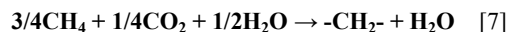
Other features of the proposed design are:

- The use of a direct drive natural gas engine to power the compressors, reducing the electrical load requirements
- The use of the heat from incineration for steam reforming
- The use of the hot syn-gas from the reformer for distillation
- No waste water treatment necessary
- Emissions limited to the effluents of the incinerator

Discussion

Because of the economy of scale GTL projects have been limited to large gas fields. Large projects require large investments. This paper attempted to identify the opportunity of down sizing to the scale of 5,000 to 10,000 gal per day by taking advantage of low cost LFG and associated emission credits. Most the processes discussed in this paper has been greatly simplified. In fact the process calls for inputting only organic waste and water, and then waiting 200 days before producing a reasonable quantity of syn-fuel without any electrical load requirement. The process also minimizes and contains all waste products. The opportunity is here. The challenge is to make a business case with a more thorough engineering/cost study.

References

1. Reinhart, D.R., Townsend, T.G. *Landfill Bioreactor Design and Operation*, Lewis Publishers, Boca Raton, FL. 1998.

2. Komillis, D.P., Ham R.K., Stegmann R., *The Effect of Landfill Design and Operation Practices on Waste Degradation Behavior:A Review,* Waste Management Res., 17, 20-26, 1999.

3. Komillis, D.P., Ham, R.K., Stegmann, R., *The Effect of Municipal Solid Waste Pretreatment on Landfill Behavior: A Literature Review,* Waste Management Res., 17, 10-19, 1999.

4. *The Bioreactor Landfill; Next Generation of Landfill Management*, A White Paper from Waste Management, Inc.

5. Vandor, D., *Liquid Natural Gas (LNG): An Alternative Fuel from Landfill Gas and Wastewater Digester Gas*, Technical Report Brookhaven Nat. Lab., 1999.

6. Acrion Technologies, Inc., Cleveland, Ohio; US Patent 5,681,360 Landfill Gas Recovery, 28 Oct. 1997.

7. Mahajan, D., Koyayaashi, A., Gupta, N., *Fischer-Tropsch Synthesis Catalyzed by Ultrafine Particles of Iron: Cessation of water-Gas Shift Activity*, Chem. Commun., p. 795, 1994.

SELECTIVE CHEMICAL SENSORS FOR COMBUSTION PROCESSES

Arun K Prasad, Hongwen Zhou, Pelagia I Gouma

Dept of Material Science and Engineering
SUNY at Stony Brook
314, Old Engineering Bldg,
Stony Brook, NY 11794-2275

Introduction

Semiconducting metal oxides have been studied as suitable materials for gas sensors for the past few decades because they are easy to fabricate, give fast response to gases and are robust even while operating under harsh environments. There has been various reports on these materials used as thin film gas sensors in automotive exhausts for monitoring the products of combustion processes such as nitrogen dioxide, nitric oxide, carbon monoxide, hydrocarbons etc. Traditionally, gas sensors reported till date, utilize various methods to achieve selectivity such as addition of dopants, varying the processing technique use of mixed metal oxides etc. It is shown that it is possible to achieve the desired sensing properties by altering the polymorphic phase of a single oxide material.

Experimental

Ion Beam Deposition. Thin films of tungsten trioxide were reactively sputter-deposited onto alumina substrates in a dual ion beam deposition system. Ion-beam sputtering from the 6" diameter tungsten target was done using a filamentless radio-frequency inductively coupled plasma (RFICP) primary source, with the film partially oxidized during growth using a RFICP assist source directed at the substrate. The ratio of oxygen to argon in the secondary plasma was maintained at 1:1 and the overall process pressure was 1.6×10^{-4} Torr. A more extensive description of the deposition chamber is given elsewhere [1].

Sol-gel Preparation. Thin films of sol-gel WO_3 was prepared using tungsten isopropoxide obtained from Chemat Technology. The solutions were prepared by mixing it with n-butanol to obtain 0.1M solution. After mixing, the sol was mechanically agitated for 5 min and then ultrasonic agitation was performed for 2 hours. The sol was then allowed to age and settle. A transparent yellow liquid was obtained after 24 hours of aging. The sol was dropped on sensor substrate which consists of alumina substrate with gold interdigitated electrodes (200 μm width and 150 μm separation). The substrate was spun at 2500 rpm for 30 s in a spin coater (Chemat Technology KW-4A). The films were then sintered for 8 hours at 500°C.

Sensor Testing. The sensing tests were carried out inside a tube furnace (Lindberg/Blue), which was heated at a programmed rate. The sensor was placed inside the tube furnace in a quartz tube (1 in. diameter and 24 in. length) and is connected to external leads. The sensing tests were performed at 450°C. The gases used for sensing are nitrogen dioxide and ammonia. The gases were controlled using MKS flow controllers. Synthetic air was used as background gas. Electrical resistance measurements of the sensing films as a function of gas concentration were recorded using Agilent 34401 digital multimeter.

Characterization. TEM investigations were performed using a Philips CM12 transmission electron microscope with LaB_6 cathode and incident energy of electrons of 120keV. XRD was performed on a Philips CM1728 diffractometer, to identify the phases in the sol-gel films during various stages of the study. DSC/TGA studies were carried out using NETSCH Analyzer STA 441C.

Results and Discussion

Figure 1 shows the sensing response of the IBD WO_3 deposited on the sensor substrates. The response shows the shift in resistance of the WO_3 IBD films upon exposure to various concentration pulses from 400 ppm down to 100 ppm of various gases such as ammonia, and nitrogen dioxide. It is seen that the WO_3 films are more sensitive to nitrogen dioxide than ammonia (a 200% increase in case of NO_2 as opposed to less than 5% decrease in case of NH_3). The average grain size found by TEM analysis is around 50 nm. Phase determination by electron and x-ray diffraction studies revealed the presence of orthorhombic phase of β-WO_3 phase.

Figure 2 shows the DSC/DTA data for sol-gel WO_3 films. We observed a peak near 320°C which is probably associated with water removal. XRD investigations showed no peaks associated with WO_3 phases. The next broad peak which was observed at around 500°C is probably associated with the formation of metastable orthorhombic phase of β-WO_3. Heat treatments were done at this temperature for 8 hours with the sol-gel deposited on sensor substrates and sensing tests were carried out. **Figure 3a** shows the response of sol-gel WO_3 film to various concentrations of NO_2 from 100 ppm down to 20 ppm. **Figure 3b** shows the response of sol-gel WO_3 film to various concentrations of NH_3. There is found to be a 25% decrease in resistance with NO_2 as opposed to only less than 0.1% decrease with ammonia. The inverse response with NO_2 as compared with that obtained from IBD films can probably explained due to the change in carrier concentration from n to p type of the semiconducting oxide and is discussed in detail elsewhere[1].

Figure 4 shows the TEM bright field image of sol-gel films after sensing. The grain size as observed is found out to be in the range of 20-30 nm.
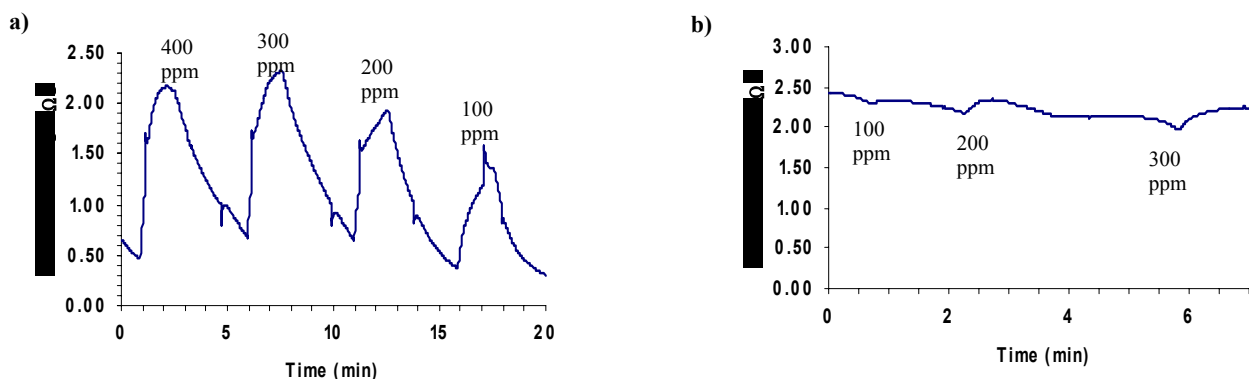

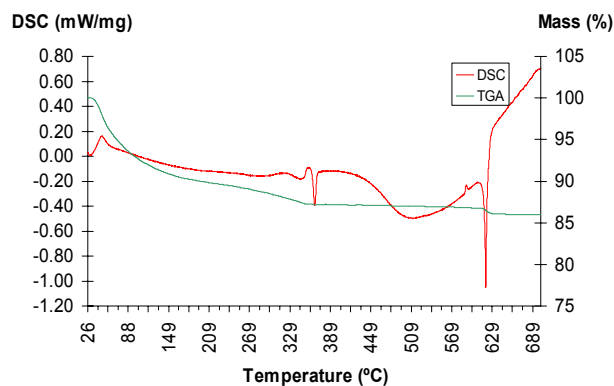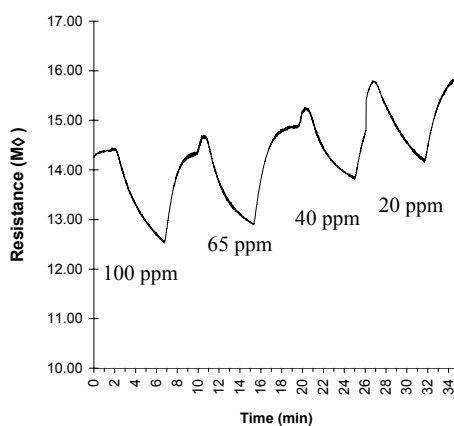**Figure 1.** Sensing response of IBD WO_3 to a) NO_2 and b) NH_3

Figure 2. DSC/TGA curve for sol-gel WO$_3$

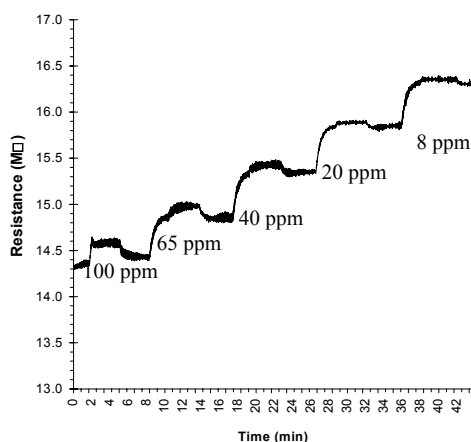**3a)**

3b)

Figure 3
a) Response of sol-gel WO$_3$ to various concentrations of NO$_2$
b) Response of sol-gel WO$_3$ films to various concentrations of NH$_3$

It is shown that the orthorhombic phase of WO$_3$ which possesses a distorted ReO$_3$ structure is selective to NO$_2$ in comparison to NH$_3$. In our other work with MoO$_3$ [2], we have shown that he existence of β-MoO$_3$ phase (monoclinic) which has a similar structure to that of β-WO$_3$ (orthorhombic)[3]. Sol-gel technique is better suited to applications in microhotplates because it allows easier method of depositing film on desired areas in the microhotplates.
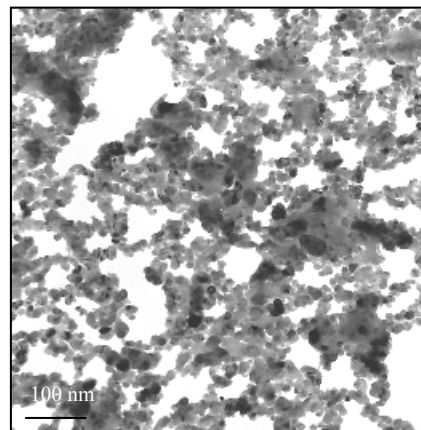

Figure 4. TEM bright field image of sol-gel films after sensing

Current work focuses on processing of thin films made of a single oxide material which show preferential selectivity which depends upon the polymorphs chosen as the sensing element. The hotplates used are fabricated and copyrighted by NIST. Future work will report on these results.

Conclusions

Selective NO$_2$ sensors were fabricated using IBD films of tungsten trioxide. The films were characterized and the microstructure of the films which are sensitive to NO$_2$ are identified. Using sol-gel technique, thin films of the same oxide material are fabricated possessing similar microstructure. Sensing tests performed using the sol-gel WO$_3$ films showed selective response to NO$_2$ in comparison to ammonia. Incorporation of these sol-gel films on microhotplates is currently under study and will be reported in future work.

References

(1) Prasad, A. K.; Kubinski, D.; Gouma, P. I. *Sensor Actuat B-Chem* **In Print**.
(2) Prasad, A. K.; Gouma, P. I. *Journal of Materials Science* **Submitted**.
(3) Mccarron, E. M. *J Chem Soc-Chem Comm* **1986**, *4*, 336-338.

METHANOL SYNTHESIS FROM SYNGAS IN A SLURRY REACTOR

Fei Ren, Hansheng Li, Dezheng Wang and Jinfu Wang
Department of Chemical Engineering, Tsinghua University, Beijing 100084, China
Weixiong Pan and Jinlu Li
Department of Chemistry, Tsinghua University, Beijing 100084, China

Introduction

The synthesis of methanol from CO and H_2 has become more important since methanol is one of the materials that can substitute the forthcoming depletion of petroleum. Industrially, methanol is produced catalytically on copper-containing catalysts such as $Cu/ZnO/Al_2O_3$ and $Cu/ZnO/Cr_2O_3$ from synthesis gas containing carbon monoxide, carbon dioxide and hydrogen in a gas-phase process at high pressures and temperatures. The synthesis gas is usually produced by the steam reforming of natural gas or other hydrocarbons or coals.

In the gas phase process, syngas reacts on the surface of the catalysts in a fixed bed reactor. In this type of reactor, the control of the reaction temperature uses the recycling of excess synthesis gas for the removal of reaction heat. H_2-rich synthesis gas is the preferred media for heat removal because the heat capacity of H_2 is much larger than that of CO. Therefore, the one-pass CO conversion is kept at a relatively low level. The recycling and compression of synthesis gas result in a huge energy consumption [1].

To overcome these disadvantages of the gas phase process, liquid phase processes for methanol production have been developed.[2] A higher one-pass CO conversion is obtained in the liquid phase processes, and these new processes also confer technical advantages when CO-rich synthesis gas is used as the feedstock.

In this work, we report the development of a new catalyst (denoted LP201) which gives a high CO conversion without any decrease in activity in 1000 hour operation in a slurry reactor for the synthesis of methanol. The syntheses of methanol in a slurry reactor and a fixed bed reactor are compared and the deactivation of the catalyst in the gas-phase process is discussed.

Experimental

Catalyst preparation. The catalyst, denoted as LP201, has a molar ratio of copper, zinc, aluminum and zirconium of 5:4:0.8:0.2 and was prepared by a co-precipitation method described elsewhere.

Catalyst characterization. The BET specific area of the catalyst samples were measured in a Micrometrics ASAP 2400 apparatus by nitrogen adsorption. The specific area of the catalyst LP201 is 93 m^2/g. Thermogravimetric analysis was performed on a WCT-2A thermogravimetric apparatus and infrared spectroscopy on a Nicolet FT-IR spectrometer.

Catalyst activity. CO (containing 4.2% CO_2) and H_2 were mixed and fed into a 1000 ml stirred autoclave with a series of controllers which provide precise control and measurement of temperature (± 1 K), agitator speed and pressure (Autoclave Engineers, USA). After reaction, the mixture is processed by a high-pressure gas-liquid separator. The gas phase flows out through a back-pressure regulator and is analyzed on-line by gas chromatography. The flow rate is measured with a wet flow meter. The liquid phase flows through a needle valve and enters a normal-pressure gas-liquid separator. The liquid product (methanol) is weighed and its composition is analyzed by gas chromatography. The solvent is liquid paraffin, whose distillation cut-off temperature is

higher than 573 K. The catalysts are LP201 or C302 (manufactured in China) used with particle sizes of 150-180 mesh. Before use for methanol synthesis, they were reduced in H_2/N_2 (3.4%H_2) at 240℃ and 0.8 MPa.

Results and Discussion

The activities of the LP201 and commercial C302 catalysts in a mechanical agitated slurry reactor are compared. The result is shown in Figure 1. It can be seen that the activity of the LP201 catalyst is much higher than that of the commercial C302 catalyst. When LP201 is used, its syngas conversion at the lower pressure of 4 MPa is higher than that of C302 at 6 MPa. This indicates that the LP201 catalyst is suitable for the large scale synthesis of methanol in a slurry reactor.
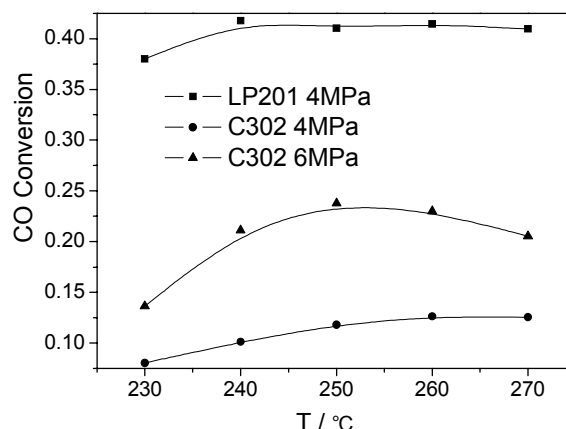

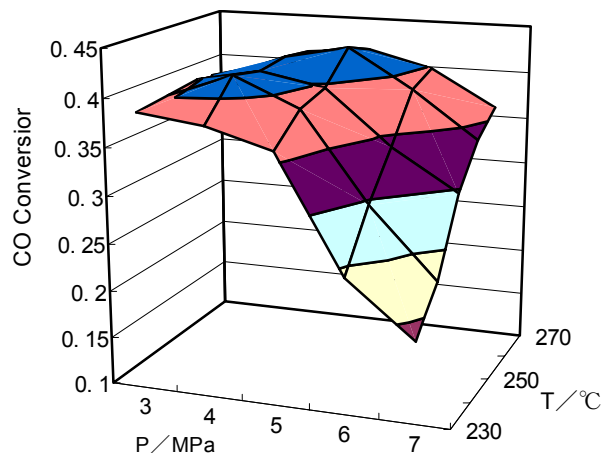**Figure 1**. Comparison of the activities of LP201 and C302 at a space velocity of 3000 ml.gcat^{-1}.hr^{-1} and H_2/ $(CO+CO_2)$ of 2

Figure 2. Influence of temperature and pressure on CO conversion at a space velocity of 3000 ml.gcat^{-1}.hr^{-1} and H_2/ $(CO+CO_2)$ of 2

Figure 2 shows the influence of temperature and pressure on CO conversion in a slurry reactor. There exist different phenomena at high and low pressure conditions. When the pressure is relatively low, with an increase in temperature, the change in CO conversion is not monotonic, and the trend is that of an increase followed by a decrease, with the maximum conversion appearing near 250 ℃ . This

phenomenon is in agreement with many works in the literature[3, 4] and our previous works.[5] As the reaction temperature increases, the reaction rate gets higher and leads to the increase of CO conversion. However, methanol synthesis is an exothermic reaction, and a low temperature is more beneficial for methanol synthesis. With continual increase in the reaction temperature, the conversion does not continue to increase because of thermodynamic limitation, but a decreasing trend will even appear. When the system pressure is relative high, because of the relatively low CO conversion, the system is far from thermodynamic equilibrium and under the control of reaction kinetics. In this case, CO conversion increases monotonically with an increase in temperature.

In the whole temperature range studied, with an increase in pressure, CO conversion first increases and the decreases. Methanol synthesis is a volume-decreasing reaction, and a high pressure benefits methanol generation, but when the pressure increases beyond a certain pressure, methanol accumulates in the liquid phase, which leads to a check on methanol synthesis and the CO conversion decreases.
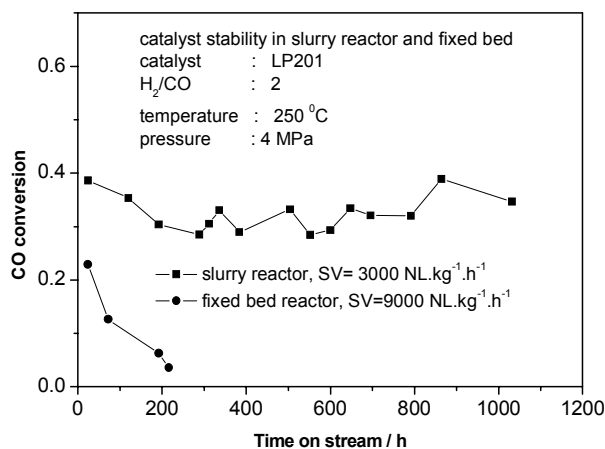

Figure 3. Stability of LP201 catalyst in a slurry reactor and a fixed bed reactor.

LP201 has a higher catalytic activity and good stability in a slurry reactor, as shown in Figure 3. The one-pass CO conversion is still higher than 30% after a 1000-hour lifetime experiment. However, in a fixed bed reactor, the catalyst activity shows an obvious decreasing trend at a space velocity of 9000 L.kg^{-1}.h^{-1}. This phenomenon shows the advantage of a slurry reactor compared with a fixed bed, and the liquid phase methanol synthesis is more suitable for the large-scale industrial application.

To understand the deactivation of catalyst LP201 in the fixed bed, thermogravimetric analysis (TGA) and infrared spectroscopy studies were carried out. Figure 4 shows the results of TGA. The TG curve shows three regions of weight loss: 20~110, 110~300 and 600~800℃, which are attributed to water loss and carbon combustion of the deactivated catalyst, respectively. Meanwhile, an endothermal peak around 80℃, and two exothermal peaks around 300 and 700℃ appear in differential thermal analysis (DTA) that are related to the thermo-gravity losses. These indicate the existence of carbon on the deactivated sample and the two exothermal peaks around 300 and 700℃ in DTA represent different types of carbon[6]. Figure 5 shows the FT-IR spectra of LP201 catalyst before reduction (A), after reduction (B), after deactivation (C) and the sample after TGA of the deactivated catalyst (D). The surface structure of the deactivated catalyst is very different from the LP201 catalyst after reduction and

before methanol synthesis and the change in the structure of the deactivated catalyst is irreversible. This suggests that an irreversible change in the structure of catalyst and carbon deposition during the gas-phase methanol synthesis led to the deactivation of the catalyst.
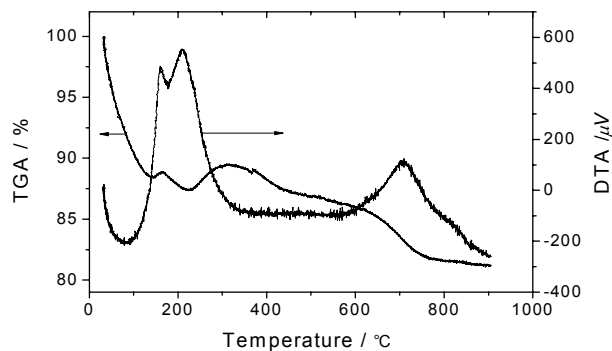

Figure 4. TGA and DTA of deactivated LP201 catalyst
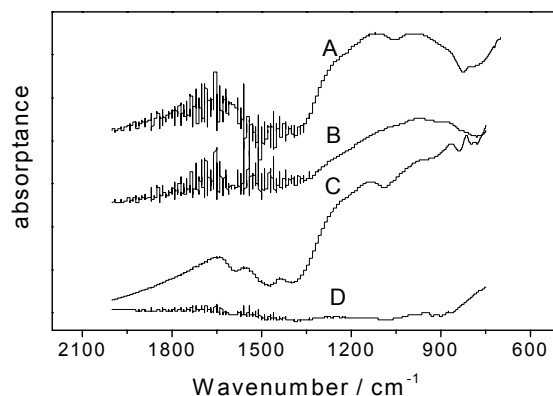

Figure 5. Infrared spectra of LP201 catalyst
A-before reduction, B-after reduction, C-after deactivation, D-the sample after TGA of the deactivated catalyst

References

(1) Zhang Kai, Song Huisen, Sun Dongkai, Li Shunfen, Yang Xiangui, Zhao Yulong, Huang Zhe, Wu Yutang. Fuel, **2003**, 82(2): 233-239.

(2) H. Mabuse, K. Hagihara, T. Watanabe, M. Saito. Energy Conversion and Management **1997**, V38, pp. S437-S442.

(3) Inui T., Li J.-L. Applied Catalysis A. **1996**, 139(1-2): 87-96.

(4) Liaw B.J., Chen Y.Z. Applied Catalysis A. **2001**, 206(2): 245-256.

(5) Yuwei Wang, Zhiliang Wang, Jinfu Wang, Yong Jin, Petrochemical Technology. **2002** 31(8): 597-601.

(6) Liu H M, Li T, Xu Y D. Chem. J. Chin. Univ., 2002, 23(8): 1556-1561.

BIOCHEMICAL ENHANCEMENT OF COALBED METHANE (CBM) RECOVERY AND ITS POTENTIAL FOR TREATMENT OF PRODUCED WATER

Mow S. Lin and Eugene T. Premuzic

Energy Sciences & Technology Department
Brookhaven National Laboratory
Building 815
Upton, NY 11973-5000

Introduction

Exploration and production of coal bed methane (CBM) resources has been increasing rapidly in recent years. In the United States, the CBM resource is estimated to be between 275 to 649 trillion cubic feet (TCF). The current production amounts to 7.5 percent of the total natural gas production in the US.[1] Along with CBM, water is co-produced during the process and compared to conventional natural gas wells, the amount of produced water is significantly higher. With increasing CBM production, the produced water is expected to increase accordingly. Currently, the water produced is either disposed or reused. If this water, after treatment, meets the requirements of several State and Federal regulations such as Clean Water Act, Resource Conservation and Recovery Act and Drinking Water Act, it may be added to the local water supply. Some source dependent produced water may contain salts, dissolved organic compounds and metals including radioactive elements, which require expensive treatment, before it is disposed to surface or compatible subsurface formations. In contrast to the oil industry, the water is not reinjected into the reservoir to enhance recovery as practiced in many oil fields. In this study, the feasibility of biochemically-enhanced recovery of CBM will be discussed.

Experimental

Bioabsorption of dissolved metals. All microorganisms were purchased from ATCC and grown to maximum growth according to published procedures.[2] The cells were harvested by centrifugation and washed with isotonic water, then stored at 4 $^{\circ}$C. The samples were resuspended in synthesized salts solution and allowed to equilibrate at 25 $^{\circ}$C for 30 minutes. The concentrations of metals in the samples were analyzed by atomic absorption spectroscopy (Perkin-Elmer model 560) calibrated according to the manufacture's manual.

Degradation of dissolved organics. Heavy crude oil was added to a mineral medium of 2 g NH_4Cl and 5.57g Na_2HPO_4, 2.44g KH_2PO_4, 0.2g $MgCl_2$, 0.001g $CaCl_2 \cdot H_2O$ and 0.001g $FeCl_3 \cdot H_2O$ per liter up to a saturation of 25 $^{\circ}$C. 5% (v/v) of fully-grown *Acinetobacter sp* ATCC 31012 was added to the sample and incubated at 30 $^{\circ}$C aerobically. The reaction was monitored by UV-VIS spectrophotometer at 260 nm.

Biochemical conversion of coals. Coals were ground by mortar and pestle into a powder under 80 mesh and stored in a desiccator. A dried sample was suspended as 2 % (w/v) of powder in the above described mineral medium in an Erlenmeyer flask. The sample was inoculated with 5% of *Acinetobacter* culture (10^8/ml) and incubated aerobically on a rotary shaker at 30 $^{\circ}$C for 7 days. A control sample without inoculation was prepared and treated under the same conditions. After treatment the samples were filtered and dried in a desiccator for analysis.

Pyrolysis-gas chromatography-mass spectrometry analysis. A CDC 150 pyroprobe was fitted with the inlet of a Perkins Elmer gas chromatograph with a 30m DB1 capillary column (J&W Co).

The sample was heated from 30 $^{\circ}$C at a rate of 20 $^{\circ}$C /m sec to 800 $^{\circ}$C and held for 10 sec. The pyrolysate was analyzed with a temperature program set at 50 $^{\circ}$C initially for 4 minutes, then ramped at a rate of 8 $^{\circ}$C/min to 320 $^{\circ}$C and held for 20 min. The effluent was split and analyzed by a Pulse flame photometric detector (PFPD) for sulfur and by an ion trap detector (ITD) for simultaneous mass spectrometric analysis. PFPD measures the sulfur emissions, was used to selectively analyze the fragments containing sulfur.

Results and Discussion

Dissolved metals are known to accumulate in either cellular organelles or on cell surfaces and membranes.[2,3] The former process is associated with cellular functions and cell growth. The latter process is due to interaction with functional groups i.e. carboxylate hydroxyl, and amino groups which are integral parts of the cell surface. These groups form strong and specific chelating complexes that can be released by changing pH. In principle the cells can be used to adsorb and release the metals in cycles. The cells can be immobilized and engineered in a column or bed to facilitate filtration processes.

Data shown in **Table 1** indicates that different microorganisms can adsorb substantial amounts of metals both metal selectively and species specifically.[2]

Table 1. Selective adsorption of metals by different microorganisms as measured by grams of metal adsorbed/dry weight (g) of microorganisms.

Microorganism	Pb	U	Th	Cr	Mn	Sn
E. coli	0.32	0.05	0.03	0.36	0.001	0.11
S. cerevisiae	0.16	0.02	0.04	0.04	0.001	0.09
P. aeruginosa sp	0.08	0.14	0.90	0.008	0	0.1
P. fluorescens	0.08	0.02	0.56	0.1	0.05	0.02

Data shown in **Figure 1** indicate that there is a maximum adsorption of lead, U/Th decay product by *E. coli* near pH 6 and little adsorption outside the pH 3.5 to 9.5 ranges. Therefore, the bioadsorbent can be used to adsorb metals at pH 6 and release it outside the pH range for example.
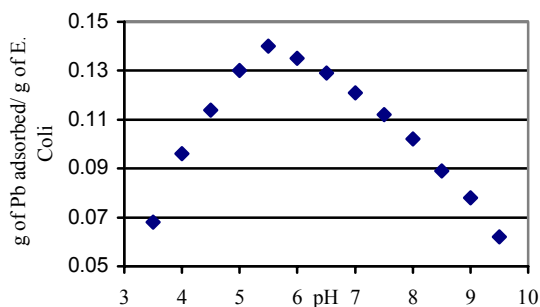

Figure 1. Effect of pH on the adsorption of lead

The chemical structure representing heavy crude oils rich in asphaltenes, resemble to a certain extent, the chemical structures of coal. Many studies of the biodegradation of petroleum oils have been reported.[4] For example as shown in **Figure 2** a fast biodegradation of a heavy crude oil occurs over a period of 16 days. The oil concentration was reduced by 70%. Under aerobic condition, the products were identified to be small acids and alcohols i.e. acetic and ethanol.[5]

Coal is a complex mixture of macromolecular hydrocarbons cross-linked by nitrogen, sulfur and oxygen (NSO) bridges as well as metals within organometallic complexes. To analyze such complex
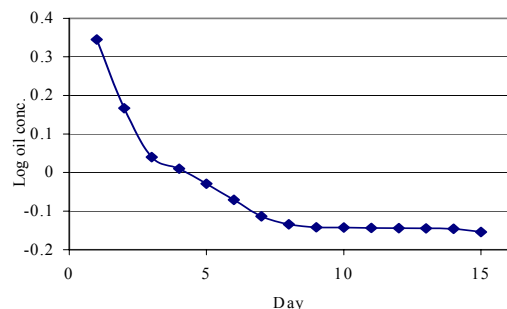

Figure 2. Biodegradation of heavy crude oil in water at 30 ^{o}C,Y axis is log oil concentration in 30 mg/liter

metrics several multipurpose analytical technique must be used.[6] In this work GC-MS, Py-GC-MS interfaced with PFPD has been used throughout (see Experimental Section) under identical conditions for untreated and biotreated samples. For example, in **Figure 3**, the result of a Py-GC analysis using the sulfur specific detector (PFPD) shows significant changes in the organosulfur components of the untreated and treated coal samples. In the treated sample, smaller molecular weight sulfur compounds appear in the retention time region of 3-7 min., accompanied with reduction of substituted thiophenes in the 6-11 min. region, dibenzothiophenes in the 10-25 min. and larger organosulfur compounds in the 30-60 min. region. The results suggest that the coal matrix structures was broken at the cross-linking bridges yielding smaller molecular weight fractions.
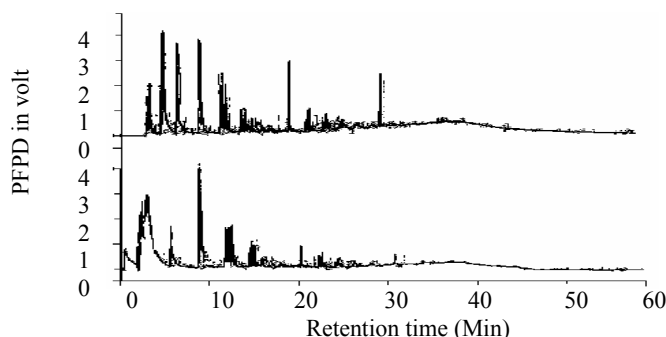

Figure 3. Py-GC-PFPD selective analysis of sulfur compounds of untreated Wyodak coal (top) and aerobically biotreated coal (bottom) samples.

Shown in **Figure 4,** the Py-GC-MS analysis of untreated coal pyrolysate with standards identify hydrocarbon compounds from retention time 5-10 min. as C_6-C_{12} fraction, 10-25 min. as C_{12}-C_{18} diesel fraction, 25-40 min. as C_{18}-C_{32} fractions and 40-60 min. as C_{32}-C_{50} fractions correspondingly. Under identical analytical conditions, the treated sample shows 40% more of C_{10}-C_{16} fractions and 20% more of C_{28}-C_{82} fractions, which further supports the observation shown in **Figure 3**.

Anaerobic transformation of coal has been reported as a potential source of methane from coal [7]. Biochemical reactions enrich the lighter carbon isotope in the product. It is recognized that the isotope effects measured as $\delta^{13}C$ of thermogenic CH_4 and biogenic CH_4 are in the range from −50 to -20 ‰ and −110 to -50 ‰ respectively.[8] Isotopic studies of $\delta^{13}C$ from gases produced from two

wells in Alberta, Canada measured ranging from −56.4 to −48.4. The results of these gases, rich in lighter carbon (^{12}C) indicate that they are biogenic in origin. Attempts to incubate the microbes from cores isolated from these wells were not successful. However, laboratory studies were able to produce significant amounts of biogenic methane using coal as the only substrate. [9]
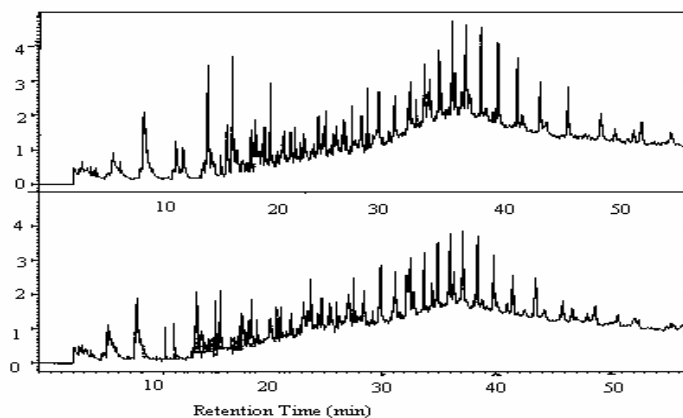

Figure 4. The Py-GC-MS analysis of hydrocarbons of treated Wyodak coal (top) and untreated sample (bottom). Y axis is detector response of unit in Mega counts.

Conclusion

The data presented in this paper indicate that coal under certain conditions can be biodegraded and the initial and produced material can be analyzed for. This implies that the biodegradation of coals under aerobic and anaerobic condition can be monitored, which is essential to the development of a processing technology. Currently, the assumption that the produced waters may also be biotreated in a manner similar to processing of coal by either biosorption and/or further biotreatment in an attractive possibility and is being further explored.

References
1. USGS Fact Sheet FS-156-00, November **2000**.
2. Premuzic, E. T., Lin, M., Zhu, H. L., and Gremme, A. M., *ArchEnviron. Contam. Toxicon.*,**1991**, 20, 234-240.
3. Beveridge, T. J.; Koval, S. F., *Appl. Environ Microbiol* **1981**, 42(2): 325-335.
4. Altas, R. M. Bartha, R.,*biotechnol Bioeng,* **1972,** 14, pp. 309-317.
5. Premuzic, E. T., Lin, M. S., *Resources, Conservation and Recycling*, **1991**, 5, pp. 277-284
6. Lin, M. S., Premuzic, E. T., Manowitz, B., Jeon, Y., and Racaniello, L., *Fuel,* **1993,** 72, No. 12, pp. 1667-1672
7. Deobald, L. A.,**1993** in: *Microbial transformation of low rank coals,* pp/ 111-138, Crawford, D. L. (Ed). CRC press, Inc. Boca Raton, FL.
8. Whiticar, M.J. **1999**, *Chem. Geology*, 161, 291.
9. Budwill, K., 4th Annual unconventional Gas and Coalbed Methane Conference, **2002**, Oct. 24, Alberta Research Council

REDUCTIVE DECHLORINATION OF CHLORINATED SOLVENTS IN GROUNDWATER : A CASE STUDY

Eric Rodriguez[1], Kevin A. McGuinness[1], and Duke U. Ophori[2]

[1]ARCADIS G&M
1200 MacArthur Blvd
Mahwah, NJ

[2]Department of Earth and Environ. Studies
Montclair State University
Upper Montclair, NJ 07043

Introduction

In groundwater contaminated by chlorinated aliphatics, remediation by reductive dechlorination is a well-documented process that occurs given the appropriate groundwater environment[1,2]. The first microbiologically mediated reductive dechlorination of perchloroethene (PCE) and trichloroethene (TCE) was observed in the early 1980s, and the first evidence of complete dechlorination of PCE to ethane under methanogenic conditions was reported in 1989[3]. According to Sutherson[3], even where a strongly reducing natural groundwater environment is not present, complete and effective reductive dechlorination of chlorinated volatile organic compounds (CVOCs) can still be accomplished by artificially driving an aquifer to a strongly reduced state that is maintained throughout the remedial process. The injection of a reagent solution (electron donor) to serve as a carbohydrate substrate can enhance microbial activity (biostimulation) by providing a carbon source[3].

In this study, an experiment was conducted, in which a carbohydrate solution (molasses) was injected into groundwater wells at a site impacted with CVOCs, in an attempt to create strongly anaerobic and reducing conditions that might cause Enhanced Reductive Dechlorination (ERD). A post-experiment evaluation of the site was performed to ascertain: 1) if a strongly anaerobic and reducing zone was created successfully, and 2) if reductive dechlorination was enhanced.

Site Description

The site occupies approximately 1.8 acres of land in the metropolitan New York. Locally, the site is underlain by fill material consisting of sand, silt, gravel, bricks, marble fragments, and boulders. Regionally, the bedrock is composed of the Manhattan Formation Schist, Inwood Marble, and Fordham Gneiss.

Manufacturing operations at the site were initiated in 1951 and ceased in 1998. Operations consisted of electroplating and the use of degreasers, which are believed to be the source of a CVOC plume, mainly TCE, at the site. An initial review of available site-specific data showed that high concentrations of TCE were present in the upper 10 feet of the aquifer, and that reductive dechlorination was already occurring at the site but because of only aerobic to slightly anaerobic conditions, complete dechlorination was not occurring.

Pre-Experiment Evaluation

The focus of this study was to create conditions that would enhance or drive reductive dechlorination to completion at the site. Prior to creating such anaerobic conditions, it was necessary to assess the existing natural background conditions of groundwater at the site. The conditions would assist in the creation and implementation of an In-situ Reactive Zone (IRZ), defined as an area in a groundwater system where strongly reducing and anaerobic conditions have been created for the purpose of reducing chlorinated compounds in groundwater. These data would also serve as the background with which post-experiment results could be compared. The background evaluation was performed to identify key electron acceptors and donors available, and to establish existing oxidation-reduction potential (REDOX) conditions. These data were obtained by collecting and analyzing groundwater samples from wells, and by collecting wellhead field parameters during low-flow well purging[4].

Groundwater levels in wells were measured to characterize the groundwater flow field. Results of these measurements indicate that groundwater flows to the south and southwest at the site.

Groundwater sampling was performed using the low-flow methodology[4]. Wells were purged using a Grundfos Rediflow 2 submersible pump at a purge rate between 0.2 and 0.5 liters/min. Trichloroethene (TCE) was found to be the diagnostic constituent of concern at the site. The highest concentrations of total CVOCs in groundwater were detected in the upper unconsolidated unit between the depth range of 10 to 20 feet. Concentrations of TCE ranged from not detected to 28,000 ppb.

Field parameters were collected during low flow purging using a flow-through-cell. A YSI 600XL water meter was used to measure water-quality and field parameters such as DO, REDOX, temperature, specific conductance, pH, total organic carbon (TOC) and dissolved organic carbon (DOC). Samples were submitted to a certified laboratory for analysis, except for ferrous iron and sulfide that were analyzed directly in the field using a HACH spectrophotometer.

The field parameters and biogeochemical analysis were used to determine the DO and REDOX conditions of the site, and to evaluate the presence of electron acceptors and donors. Dissolved oxygen is the most thermodynamically favored acceptor used by microbes for the biodegradation of organic carbon. After depletion of DO, microbes will preferentially use nitrate as an electron acceptor, followed by iron (III), sulfate (sulfanogenesis), and carbon dioxide (methanogenesis) in that order[1].

During the pre-experiment assessment, one up-gradient well (MW-HP-8S), three side-gradient wells (GP-106, MW-2, MW-4S), seven mid-plume wells (GP-107, PTW-1, GP-105, MW-HP-1S, MW-HP-1D, GP-104), and three distal-plume wells (GP-103, MW-7S, GP-102S), were sampled as in literature[1].

A summary of relevant field and analytical data from this assessment showed DO and REDOX values which indicated aerobic and oxidizing groundwater conditions in the up-gradient well, transitional to aerobic conditions in the side-gradient and mid-plume wells, and anaerobic to aerobic conditions in the distal-plume wells. Sufficient concentrations of electron acceptors such as nitrate, manganese, Fe(III), sulfate and carbon dioxide were available for microbial respiration, once oxygen was depleted, to support reductive pathways.

Experiment

A 20-month in-situ bioremediation experiment was conducted by injecting a carbohydrate substrate (molasses) into the groundwater to increase microbial activity and thus to deplete the electron acceptors. The goal was to create an IRZ that would possibly enhance reductive dechlorination of CVOCs in groundwater at the site. Monitoring well GP-107 was selected as the substrate injection point because it is located in the center of the TCE plume area, that has historically shown elevated concentrations of TCE. The substrate injections were performed on a biweekly schedule to create and maintain the IRZ. Fifty substrate injection events were performed between September 2000 and August 2002.

The concentration of substrate used for the first three injections into well GP-107 had a water to molasses ratio of 20:1, with a volume of approximately 100 gallons. Substrate

injections were performed using a centrifugal pump. The water and molasses were mixed using the pump and stirring rod in 55-gallon drums. Following a thorough mixing of the solution, it was injected under low pressure (approximately 2 to 12 psi) into the injection point.

Results from the pre-experiment analyses were continuously reviewed throughout the experiment to adjust the reagent strength and volume to ensure that the injections would not initiate excessive fermentation processes that can lower the pH.

To track the establishment, growth and progress of the IRZ, performance monitoring of select wells (PTW-1, PTW-2, GP-104, MW-HP-1S) immediately down-gradient and side-gradient of well GP-107 was conducted on a biweekly schedule. This allowed parameters such as DO, REDOX potential, specific conductivity, TOC and DOC to be monitored. These wells which are within and immediately surrounding the IRZ were sampled and analyzed for a targeted list of specific electron acceptors and byproducts to document that anaerobic microorganisms were depleting the acceptors, and that reduced byproducts (i.e., sulfide, ferrous iron, dissolved iron, methane) were present and accumulating. Daughter products of TCE such as cis-1,2 DCE, vinyl chloride, and ethane were also analyzed to track the anticipated increase of these compounds. This synergy of data collected is sufficient to document the occurrence of reductive dechlorination and its level of occurrence.

Results and Discussion

In-Situ Reactive Zone (IRZ). Reducing conditions were established at the injection point GP-107 two weeks after the first substrate injection was performed. The minimum target TOC concentration of 1,000 mg/L was reached approximately 1.5 months after the first injection. It was observed that the created IRZ encompassed an area down-gradient of GP-107 that included wells PTW-1, PTW-2, and MW-HP-1S, after 1.5, 5, and 10 months of the first injection respectively. Encompassment of the IRZ is characterized by increases in TOC and conductivity, and by decreases in DO and REDOX potential (Fig. 1).
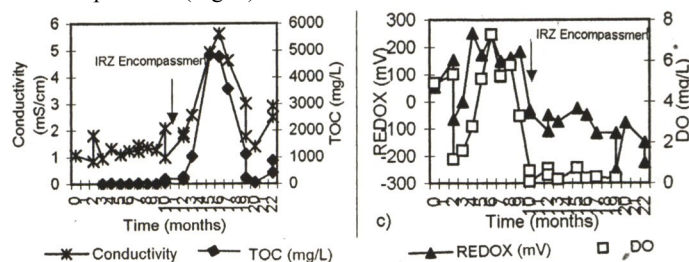

Figure 1. Example patterns of TOC, conductivity, DO and REDOX from well MW-HP-1S.

Enhanced Reductive Dechlorination (ERD). Results of the experiment provided evidence that ERD was occurring at the site due to the alteration of the groundwater environment. Factors for evaluating the occurrence of ERD include depletion of electron acceptors and increase in their byproducts as illustrated by biogeoch-
emical monitoring results, a decrease in parent (source) TCE concentrations, and the accompanying increase in daughter products. Analytical results indicated that concentrations of TCE decreased in wells PTW-1, PTW-2, MW-HP-1S, and GP-104 while daughter products, primarily cis-1,2 DCE, vinyl chloride, and ethene increased in concentration. Based on the field data and TOC results summarized in the preceding section, the IRZ has encompassed monitoring points PTW-1, PTW-2, and MW-HP-1S, and is believed to be the catalyst for the ERD of TCE. The monitoring results from the three wells encompassed by the IRZ were similar, thus only those from PTW-2 are summarized here. Monitoring well PTW-2 is located approximately 30 feet down gradient of injection well GP-107. Concentrations of TCE detected in well PTW-2 showed a significant decrease from 8,400 ug/L (pre-experiment) to 400 ug/L (post-experiment) (Fig. 2). In May and June 2001, concentrations of TCE
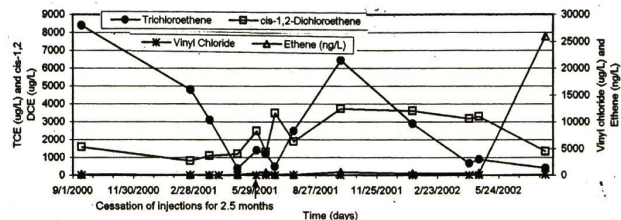

Figure 2. Distribution of TCE, DCE, Ethene and Vinyl Chloride from well PTW-2

had decreased to 380 and 480 ug/L respectively and subsequently increased to 2,500 ug/L (July 2001) and then to 6440 ug/L (October 2001). Note that the experiment was conducted in the mid-plume area, therefore a mass of TCE continues to flow into the study area, which may be responsible for the TCE concentration rebound. Additionally, a temporary cessation of injections was done to quantify how long the organic carbon in the up gradient injection well (GP-107) would remain during injection #20, which may be partially responsible for the rebound. However, following re-initiation of injections, concentrations of TCE again decreased significantly.

With the decrease of TCE, concentrations of cis-1,2-DCE increased from 1,600 (pre-experiment) to 3730 ug/L (October 2001) providing evidence of ERD of TCE and not TCE dilution processes. Following October 2001, cis-1,2 DCE decreased to 1340 ug/L at the conclusion of the pilot test demonstrating that continued and complete reductive dechlorination is occurring. This process is further supported by the detection of vinyl chloride (118 ug/L) during the last groundwater sampling event. Concentrations of ethene have also illustrated a significant increasing trend from 209 ng/L (pre-experiment) to 26,000 ng/L (post-experiment) demonstrating that the mass of TCE in groundwater has been reduced and that the final degradation product (ethene) has been achieved. The complete degradation sequence (TCE to ethene) for dechlorination of TCE has been observed.

There was more evidence from the analysis of field data and biogeochemical indicators that supported the occurrence of anaerobic and reducing conditions, as well as ERD at the site. These include: low dissolved oxygen (< 1 mg/L) and REDOX (< 0 mV) concentrations, reduced nitrate and sulfate, and increased nitrite and sulfide concentrations. Methane concentrations increased continually, suggesting that the environment could have approached and achieved methanogenic conditions.

References
1. Wiedemeier, T.H., Swanson, M.A., Moutoux, D.E., Gordon, E.K., Wilson, J.T., Wilson, B.H., Kampbell, D.H., Hansen, J.E., Haas, P., Chapelle, F.H., *Technical protocol for evaluating natural attenuation of chlorinated solvents in groundwater;* Air Force Center for Env. Excel. Tech. Transfer Div., **1996**.
2. Carr, C.S., Hughes, J.B., *Env. Sci. Tech.*, **1998**, 32, 1817-1824.
3. Sutherson, S.S., *Natural and enhanced remediation systems*, CRC Press, Inc., Boca Raton, Florida, **2002**.
4. U.S. EPA., *Groundwater sampling standard operating Procedures*, U.S. EPA., Region II, New York, **1998**.

EFFECT OF THE ADDITION OF Fe AND Mn ON STRUCTURAL AND CATALYTIC PROPERTIES OF Cu/ZrO$_2$ CATALYSTS FOR CO HYDROGENATION

Run Xu, Zhongyi Ma, Cheng Yang, Wei Wei, Yuhan Sun*

The State Key Laboratory of Conversion
Institute of Coal Chemistry
Chinese Academy of Science
Taiyuan 030001 P.R.China
*Corresponding author. Fax: +86-351-4041153. E-mail address:
yhsun@sxicc.ac.cn, yangch68@sxicc.ac.cn

Introduction

Since the last century's oils crises, higher alcohol synthesis from natural gas via syngas has received increasing attention because it can be used as gasoline blend or alternative motor fuel [1]. The preparation of more effective catalysts is still a subject for practical purposes. The catalysts most frequently used contain copper as active component, zinc oxide and alumiana or chromium oxide as a structural promoter. Several metal oxides have been tested as alternative support materials for CO/CO$_2$ hydrogenation catalysts. Among them, ZrO$_2$ is of special interest because of its mechanical and thermal stability, its high specific surface area and its intrinsic catalytic properties. In the previous work, Fischer-Tropsch elements (Fe, Co, Ni, Ru) were introduced to Cu/ZrO$_2$ based system, which successfully shifted methanol synthesis towards higher alcohols [2]. More recently, a FeCu/MnZrO$_2$ bimetallic system was designed and the interaction of molecule in the catalyst for higher alcohols synthesis was studied [3]. The interactions that occur between the active phases or metal-support generally affected the surface and structure of the catalyst and hence its catalytic performance. However, regarding the interplay of FeCu/MnZrO$_2$ catalysts, very few data was available contrasted with Cu/ZrO$_2$. The aim of the present work was to study the effect of group I and group Γ metal oxides, i.e. through iron or manganese derivates, addition to a CuZrO$_2$ catalyst.

Experimental

Catalysts preparation. Catalyst were prepared by co-precipitation from a solution of Cu(NO$_3$)$_2$·3H$_2$O, ZrOCl$_2$·8H$_2$O and/or Mn(NO$_3$)$_2$, Fe(NO$_3$)$_3$·9H$_2$O with a solution of Na$_2$CO$_3$ under electromagnetic stirring at 343K and pH=10. Then the precipitates were aged at 343K for 2h. After washed thoroughly with distilled water, the precipitates were dried and calcined. The prepared catalyst composition was as follows: Cu:Mn:Zr:Fe = 1:0.5:2:0.1(mole ratio).

Characterization Methods. The BET surface areas of catalysts were determined by N$_2$ adsorption at 77K using the Tristar 3000 Chemical Adsorption Instrument (Micromeritics). The temperature programmed reduction (TPR) of catalysts was carried out in the flowing of 5% H$_2$ in Ar. The catalysts were heated at the rate of 10K min^{-1} and the amounts of H$_2$ consumption were determined by a gas chromatograph with a TCD detector. The diffuse reflectance FTIR (DRIFT) spectra were recorded with a resolution of 8cm^{-1} and accumulation of 400 on a Nicolet Magna-II 550 FTIR spectrometer supplied with a TGS detector and a diffuse reflectance attachment. The CO temperature programmed desorption (TPD) of catalysts was carried out in the flowing of Ar. The catalysts were heated at the rate of 10K min^{-1} and the analysis of the gas was determined by mass spectrometer. The copper surface area (S_{Cu}) was determined by applying a nitrous oxide pulse method as described by Evans et al. [4]. The exit gas was analyzed by mass spectrometer. The amount of surface copper was calculated from the amount of nitrogen evolved, assuming the dissociation of nitrous oxide takes place on surface copper (average atom density : 1.49 • 10^{19}atoms/m^2) :

Catalytic test. The activity tests were conducted with a fixed-bed, stainless flow micro reactor with I.D. of 6 mm. All catalysts were reduced before syngas exposure. The analysis of the gaseous and liquid products was made by shimazu-8A gas chromatographs. CO, CO$_2$, CH$_4$ and H$_2$ were analyzed by a thermal conductivity detector (TCD) on a carbon seize column. C1-C5 hydrocarbons and the alcohols were analyzed by a flame ionization detector (FID) on a Chromosorb 101 column.

Results and Discussion

Cu/ZrO$_2$ has been reported to show high activity and high selectivity for methanol synthesis under mild reaction conditions [5]. As Stiles [6] proposed, the modifications would be made in the catalyst composition and operating conditions to increase the production of higher alcohols. Indeed, the catalytic activity and selectivity over Cu/ZrO$_2$ was not high at relatively high temperature (see **Table 1**). This might due to the sinter of Cu on the surface [7]. The addition of iron greatly influenced on the performance of the Cu/ZrO$_2$ catalyst. The catalytic activity decreased. But the content of higher alcohols in the liquid products increased as well as the selectivity to CO conversion to alcohols. This indicated that the effect of Fe could be ascribed to giving the activity sites for carbon chain growth and stabilization the catalyst against sintering. It was interesting to find the Cu/MnZrO$_2$ catalyst showed a higher activity and selectivity for alcohols synthesis [2]. The space-time yield reached 0.849 g • mL^{-1} • h^{-1} and methanol was the primary alcohol component. It was considered that Mn could mainly enhance the activity of methanol synthesis through increase the degree of Cu dispersion. As a result, contrary to the result of the bimetallic catalyst FeCu/ZrO$_2$, the performance of the Mn modified FeCu/ZrO$_2$ catalyst had a drastic change. The space-time yield increased to 0.42 g • mL^{-1} • h^{-1}. At the same time, the higher alcohols fraction represented 15.3% of the total alcohol production.

Table 1 The CO hydrogenation performances of various catalysts

Catalysts	CO Con. (%)	Selectivity [a] (%)		ROH Yield (g • mL^{-1} • h^{-1})	Alcohols Distribution (wt.-%)				
		CH$_x$	ROH		C$_1$	C$_2$	C$_3$	C$_4$ (i-C$_4$)	C$_5^+$
Cu/ZrO$_2$	13.05	42.79	57.21	0.209	98.01	1.33	0.66	---	---
FeCu/ZrO$_2$	7.80	24.99	75.01	0.19	95.11	2.65	0.91	1.09(0.94)	0.24
Cu/MnZrO$_2$	37.28	21.79	78.21	0.849	94.01	2.41	1.61	1.4(0.96)	0.58
FeCu/MnZrO$_2$	26.3	40.17	59.83	0.42	84.7	7.65	3.12	3.49(1.48)	1.04

Reaction conditions: 573K, 8.0MPa, 8000h^{-1} a: selectivity based on number of atoms per gram carbon = [number of CO converted to given product / total number of CO converted] × 100%

The surface areas and copper dispersion of catalysts are given in **Table 2**. The Cu/ZrO_2 showed a lower BET surface area of all catalysts. But this was obviously increased on the bimetallic catalyst $FeCu/ZrO_2$. It can be seen that a high surface areas was achieved in Mn modified catalysts. And the area of $FeCu/MnZrO_2$ catalyst was enhanced ulteriorly than Mn modified alone. The Cu dispersion and surface areas of Cu/ZrO_2 slightly improved via the addition Fe promoter. The Cu-dispersion degrees in the $Cu/MnZrO_2$ catalyst system increased greatly. This might account for the catalytic results that the activity for methanol synthesis on $Cu/MnZrO_2$ catalyst was much higher than Cu/ZrO_2 catalyst and the $FeCu/MnZrO_2$ catalyst showed a good performance on higher alcohols synthesis.

Table 2 BET surface areas and Cu dispersion of various catalysts

Catalysts	S_{BET} ($m^2 \cdot g^{-1}$)	D_{Cu} (%)	S_{Cu} ($m^2 \cdot g^{-1}$)
Cu/ZrO_2	61.16	1.07	1.35
$FeCu/ZrO_2$	112.14	1.13	1.41
$Cu/MnZrO_2$	193.32	5.67	6.32
$FeCu/MnZrO_2$	196.6	6.55	7.15

Figure 1 illustrates TPR curves for the copper catalysts with different promoters, such as Cu/ZrO_2, $FeCu/ZrO_2$, $Cu/MnZrO_2$ and $FeCu/MnZrO_2$. Only one peak was seen at 543 K on bulk CuO (not shown in figure). This peak was considered to the reduction of CuO to Cu. Over Cu/ZrO_2 catalyst, the peaks shifted to lower temperature and two peaks were discerned at 473K and 528K, according to the reduction of highly dispersed CuO and bulky CuO, respectively [8]. The peak shifted to higher temperature when Fe was added. The reduction of CuO in $FeCu/ZrO_2$ occurred at the temperature range 420-600K with only one peak at 508 K. It indicated that single state of Cu^{2+} existed in $FeCu/ZrO_2$ catalyst, and the interaction between copper and other components was enhanced, which hindered the reduction of CuO. For Mn-promoted Cu/ZrO_2, the intensity of former peak increased and shifted to higher temperatures, while the latter peak decreased. On $FeCu/MnZrO_2$ catalyst, the former reduction peak shifted to higher temperatures with the maximum at 513K, and the latter one disappeared. It was in line with the results that the addition of iron improved the dispersion of Cu.
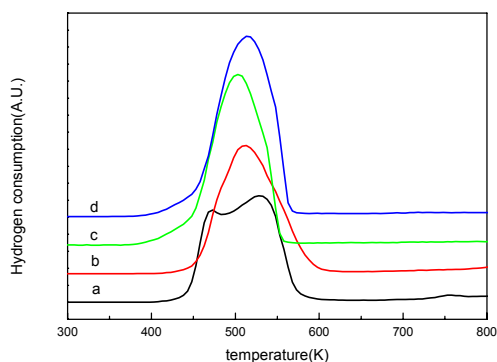

Figure 1. The H_2-TPR curves of iron and manganese modified Cu/ZrO_2 catalysts.
a: $CuZrO_2$ b: $FeCu/ZrO_2$ c: $CuMnZrO_2$ d: $FeCuMnZrO_2$

The IR bands of CO adsorbed on various catalysts are shown in **Table 3**. CO has been extensively used to identify the nature of adsorption sites in copper catalysts [9]. According to the research of

Fisher and Bell [10], the bands of CO adsorption with the frequencies of 2095-2120 cm^{-1} could be attributed to linearly adsorbed CO on Cu sites. Noteworthy was that the band of CO adsorbed on monometallic catalysts shifted to high frequency when addition Fe promoter. And the intensity of the bands above mentioned also enhanced in consistent with Cu dispersion and surface areas improved. Furthermore, the interaction between Cu and Fe resulted in the antibonding of the metal d-electrons to the $2\pi^*$-orbital of the CO molecule decrease, thus weakening of the carbon-metal bond in the chemisorbed CO molecule on Cu, which leaded to the band of CO adsorbed shift to high frequency.

The results of CO-TPD are also listed in **Table 3**. It could be seen that the amounts of CO desorption on monometallic catalysts were few. Only a small amount of CO_2 was desorbed from Cu/ZrO_2. Contrary to the monometallic catalysts, the addition of Fe improved the CO adsorption. The amount of CO_2 desorption was almost three times than Cu/ZrO_2. Moreover, these phenomena became obviously on Mn modified catalysts. This result indicated that the number of CO adsorption sites and the interplay between CO and metal were all increased.

Table 3 The CO adsorbed on various catalysts

Catalysts	Wavenumber[a](cm^{-1})	CO ($\mu mol \cdot g^{-1}$)	CO_2($\mu mol \cdot g^{-1}$)
Cu/ZrO_2	2101_w	115[b]	45
$FeCu/ZrO_2$	2108_w	197	130
$Cu/MnZrO_2$	2109_m	317	175
$FeCu/MnZrO_2$	2113_s	475	255

[a] the wavenumber are the bands of CO adsorption on Cu
[b] the values are those of desorbed gases during the TPD

Conclusion

C_1-C_5 alcohols could efficiently be produced by modification a typical methanol catalyst (e.g. Cu/ZrO_2) from syngas by addition of iron and manganese compounds. It was found that the addition of iron could improve the selectivity of higher alcohols because of its strong chain growth ability and strong interaction with copper. The synergistic effect of manganese with bimetallic catalyst might play an important role in increase the activity for alcohols synthesis.

References

1. X. D. Xu, E. B. M. Doesberg, J. J. F. Scholten, *Catalyst. Today*, 2 (1987) 125
2. N. Zhao, R. Xu, W. Wei, Y.H. Sun, *React. Kinet. Catal. Lett.*, 75 (2002) 297
3. R. Xu, Z.Y. Ma, C. Yang, W. Wei, Y.H. Sun, *Molecule.* (In press)
4. J. W. Evans, M. S.Wainwright, A. J.Bridgewater, D. J.Youny, *Appl. Catal.*, 1983, 7:75
5. Y. H. Sun, P.A. Sermon, *J. Chem. Soc. Chem. Commun.*, (1993) 1242
6 . A. B. Stiles, F. Chen, J. B. Harrison, X.D. Hu, D. A. Storm, H. X. Yang, Ind. Eng. Chem. Res. 30 (1991) 811
7. Y. H. Sun, P.A. Sermon, *Catal. Lett.*, 29 (1994) 361
8. M. Shimokawabe, H. Asakawa, N. Takezawa, *Appl. Catal.*, 59 (1990) 45.
9. J. Ryczkowski, *Catalysis Today*, 68 (2001) 263
10. I. A. Fisher, A. T. Bell, *J. Catal.*, 178 (1998) 153